FEDERAL UNIVERSITY OF CEARÁ
CENTER OF SCIENCES
POST GRADUATE PROGRAM IN CHEMISTRY

JESSICA MIRANDA ABREU FREIRE

CARBON-BASED MATERIALS FOR WATER TREATMENT: ADSORPTION AND CAPACITIVE DEIONIZATION STUDIES

FORTALEZA
2023

JESSICA MIRANDA ABREU FREIRE

CARBON-BASED MATERIALS FOR WATER TREATMENT: ADSORPTION AND CAPACITIVE DEIONIZATION STUDIES

Thesis presented to the Post Graduate Program in Chemistry at the Federal University of Ceará as a requirement to obtain the title of Doctor in Chemistry. Concentration area: Analytical Chemistry.

Supervisor: Prof Dr Elisane Longhinotti
Co-supervisor: Prof Dr Adonay Rodrigues Loiola

FORTALEZA
2023

Dados Internacionais de Catalogação na Publicação
Universidade Federal do Ceará
Sistema de Bibliotecas
Gerada automaticamente pelo módulo Catalog, mediante os dados fornecidos pelo(a) autor(a)

F933c Freire, Jessica Miranda Abreu.
Carbon-based materials for water treatment : adsorption and capacitive deionization studies / Jessica Miranda Abreu Freire. – 2023.
134 f. : il. color.

Tese (doutorado) – Universidade Federal do Ceará, Centro de Ciências, Programa de Pós-Graduação em Química, Fortaleza, 2023.
Orientação: Profa. Dra. Elisane Longhinotti.
Coorientação: Prof. Dr. Adonay Rodrigues Loiola.

1. Water treatment. 2. Toxic metal. 3. Magnetic graphene oxide. 4. Capacitive deionization. 5. Brackish Water Desalination. I. Título.

CDD 540

JESSICA MIRANDA ABREU FREIRE

CARBON-BASED MATERIALS FOR WATER TREATMENT: ADSORPTION AND CAPACITIVE DEIONIZATION STUDIES

Thesis presented to the Post Graduate Program in Chemistry at the Federal University of Ceará as a requirement to obtain the title of Doctor in Chemistry. Concentration area: Analytical Chemistry.

Approved on 24/03/2023.

EXAMINATION BOARD

_____

Prof. Dr. Elisane Longhinotti
Federal University of Ceará (UFC)

_____

Prof. Dr. Paulo Naftali da Silva Casciano
Federal University of Ceará (UFC)

_____

Prof. Dr. Pierre Basílio Almeida Fechine
Federal University of Ceará (UFC)

_____

Prof. Dr. Luís Augusto Martins Ruotolo
Federal University of São Carlos (UFSCar)

_____

Prof. Dr. Odair Pastor Ferreira
State University of Londrina (UEL)

To my husband, Tiago, and my family.

ACKNOWLEDGEMENTS

I would like to express my gratitude to God for all the blessings in my life. The journey of challenges and accomplishments has molded me into the person I am today. To my family, my gratitude for providing me with a life of dignity, with precious teachings about principles and values. My dear mother, Angela Maria, and father, Francisco Nilson, have always recognized the important role of education for personal and professional formation. I am also thankful to my lovely husband, Tiago Melo, who has been with me since the beginning of our studies in chemistry and who has believed in me and encouraged me to surpass challenges in my life journey. To my friends, old and new, I am deeply grateful for their participation in my life. Without their love and support, my achievements would hardly have been possible.

I am also thankful to profª Elisane Longhinotti, who I have worked with since my graduation and who has become a dear friend, always giving me the support I needed and believing in my potential. I would like to extend my gratitude to my co-advisor, prof. Dr Adonay Rodrigues Loiola, for his cooperation and assistance during my doctorate studies.

I am obliged to Universidade Federal do Ceará (UFC) for providing me with countless experiences and opportunities. At UFC, I was introduced to the research world, had the opportunity to learn from amazing professionals, had an experience abroad in my doctoral studies, have been a public servant at Seara da Ciência since 2014, and met my husband and some of my dearest friends.

Finally, I would like to thank to the professors members of my qualification and defense committees for the contributions to this thesis. I am also grateful to all the partner laboratories for their invaluable support during these past years. A special thanks to my colleagues at Seara da Ciência and my lab partners at LABMA for supporting me during my master's and doctoral studies. The financial assistance provided by the Coordination for the Improvement of Higher Education Personnel (CAPES) and the National Council for Scientific and Technological Development (CNPq) were essential for the realization of the projects I have been involved in my academic journey.

RESUMO

Nesta tese foram estudadas as tecnologias de adsorção e de deionização capacitiva para o tratamento de água em diferentes abordagens usando materiais à base de carbono. Para tanto, óxido de grafeno magnético silanizado foi utilizado para a adsorção de metais tóxicos e carvão ativado (CA) suportado em feltro de grafite (FG) foi utilizado para a dessalinização de água via deionização capacitiva (DIC). No primeiro estudo, compósitos de magnetita e óxido de grafeno (MAG-GO_x) foram modificados com grupos amino (MAG-GO_1-NH_2) para melhorar a seletividade a cromo em uma solução multielementar contendo íons cádmio e cobre. Técnicas de caracterização como infravermelho com transformada de Fourier, espectroscopia Mössbauer e espectroscopia de fotoelétrons de raios-X confirmaram o sucesso da síntese e evidenciaram diferentes grupos à base de oxigênio e nitrogênio capazes de promover a adsorção dos metais. Comparando os compósitos não modificados com os silanizados, observou-se um aumento na capacidade de adsorção de Cr(VI) em relação aos outros metais: MAG-GO_1-NH_2 adsorveu Cr(VI) 39.0 e 6.5 vezes mais que Cd(II) e Cu(II), respectivamente, enquanto MAG-GO_1 adsorveu Cr(VI) 5 vezes mais que Cd(II) e Cu(II). Esse efeito foi atribuído às interações eletrostáticas e do tipo duro-duro entre as espécies de carga negativa de Cr(VI) e os grupos de carga positiva $–NH_3^+$. Além disso, experimentos de reuso mostraram uma adsorção de aproximadamente 100% de íons Cr(VI), em uma solução multielementar contendo 0,1 mmol L^{-1} de cada metal, durante 5 ciclos, demonstrando uma boa estabilidade e capacidade de adsorção do material modificado com grupos amino. No segundo estudo, estratégias simples para melhorar o desempenho dos eletrodos FG-CA na DIC foram estudadas através da modificação da espessura do eletrodo (2,0, 3,0 e 5,0 mm), da carga mássica de CA (32, 37 e 55 mg de CA por cm^2) e da sua distribuição sobre o FG. As caracterizações eletroquímicas mostraram que, ao reduzir a espessura do eletrodo e aumentar a carga mássica, melhoram-se a capacitância total (F) e a capacitância específica (F g_{CA}^{-1}), respectivamente, resultando em maiores capacidade de adsorção de sais (*SAC*) (de 2,7 mg g^{-1} para 7,9 mg g^{-1}) e redução da concentração de sal (Δc) (de 60,8 mg L^{-1} para 95,3 mg L^{-1}) nos experimentos de dessalinização. Além disso, eletrodos com uma dispersão mais homogênea de CA produziram superiores taxa média de adsorção de sais (*ASAR*, 45%) e produtividade de água (*P*, 59%). Assim, os progressos obtidos na otimização da preparação de eletrodos utilizando FG através de simples estratégias impulsionam os estudos de DIC a uma abordagem mais prática e promissora.

Palavras-chave: tratamento de água; metais tóxicos; óxido de grafeno magnético; deionização capacitiva; dessalinização de água salobra.

ABSTRACT

In this thesis, the effectiveness of carbon-based materials for water treatment was studied through the examination of adsorption and capacitive deionization technologies. For this purpose, silanized magnetic graphene oxide (MAG-GO_1-NH_2) was used for toxic metal adsorption and activated carbon (AC) supported on graphite felt (GF) was utilized for water desalination via capacitive deionization (CDI). The first study focused on modifying composites of magnetite and graphene oxide (MAG-GO_x) with amino groups (MAG-GO_1-NH_2) to improve chromium selectivity in a multielement solution containing cadmium and copper ions. Characterization techniques such as Fourier transform infrared, Mössbauer spectroscopy, and X-ray photoelectron spectroscopy confirmed the success of the synthesis and evidenced the presence of nitrogen and oxygen-based moieties able to promote metal adsorption. Adsorption studies showed improved Cr(VI) uptake in the silanized composites compared to the unmodified ones: MAG-GO_1-NH_2 adsorbed Cr(VI) at 39.0 and 6.5 times more than Cd(II) and Cu(II), respectively, while MAG-GO_1 adsorbed Cr(VI) 5 times more than Cd(II) and Cu(II). This enhancement is likely due to hard-hard and electrostatic interactions between Cr(VI) and $–NH_3^+$ groups that improve adsorption of chromium negative species. The stability of the amino-grafted material was confirmed through reuse experiments, which demonstrated that it could adsorb approximately 100% of Cr(VI) in a multielement solution containing 0.1 mmol L^{-1} of each ion over 5 cycles. In the second study, simple strategies were studied to enhance the performance of GF-AC electrodes in capacitive deionization (CDI) by modifying electrode thickness (2.0, 3.0, and 5.0 mm), AC mass loading (32, 37 e 55 mg of AC per cm^2), and its distribution over GF. Electrochemical characterizations revealed that reducing electrode thickness and increasing mass loading resulted in improved total capacitance (F) and specific capacitance (F g_{AC}^{-1}), resulting in higher salt adsorption capacity (*SAC*) (from 2,7 mg g^{-1} to 7,9 mg g^{-1}) and salt concentration reduction (Δc) (from 60,8 mg L^{-1} to 95,3 mg L^{-1}) in desalination experiments. Electrodes with a more homogeneous dispersion of AC produced significant enhancements in terms of average salt adsorption rate (*ASAR*, 45%) and water productivity (*P*, 59%). These progresses on optimizing the preparation of GF composite materials have paved the way for improving the electrochemical separation of ions and a more practical approach to CDI studies using GF-based electrodes.

Keywords: water treatment; toxic metal; magnetic graphene oxide; capacitive deionization; brackish water desalination.

LIST OF FIGURES

LIST OF TABLES

TABLE OF CONTENTS

1 CHAPTER I – INTRODUCTION

Water demand has increased around the world mainly due to urban and industrial growth, directly impacting freshwater supply. It is estimated that about 80% of industrial waste is disposed of in the environment without any treatment, making access to drinkable water even more difficult (UNITED NATIONS WORLD WATER ASSESSMENT PROGRAMME, 2017). Although approximately 71% of Earth's surface is covered by water, only 2.5% of this total corresponds to freshwater (rivers, lakes, groundwater, glaciers), while the other 97.5% is saline water (seas and oceans). Besides, most of the freshwater is inaccessible for being in the form of glaciers and permanent snow covers, which restrict its collection to limited sources as groundwater. This one stands for 30% of all freshwater in the world (ELSAID et al., 2020). Although Brazil is known as the country with the highest percentual of freshwater in the world (12%), its distribution is poor and highly concentrated in the North, Midwest, and Southeast regions. In fact, 80% of water flowing through Brazilian territory is located in the Amazonian watershed.

In Brazil, the main uses for water withdrawals are for irrigation, animal use, industry, and urban supply (Fig. 1), accounting for 92% of total consumptive water demand. In consumptive uses, water is removed from the available sources and may not be returned to them totally or partially. Over the past two decades, water usage for irrigation has increased from 640 to 965 $m^3 s^{-1}$ (50% of total consumptive water usage in 2020), and it is expected an increment in approximately 42% by 2040 (AGÊNCIA NACIONAL DE ÁGUAS E SANEAMENTO BÁSICO, 2022). Population expansion and industrial activities with intensive use of water are the main responsible for the increase in water stress in Brazil, which affects most the Southern region (where water is needed for human supply, irrigation, and industry) and South region (where large rice fields are irrigated). The Northeastern semi-arid is also very impacted by low hydric availability, due to low precipitation levels, high temperatures throughout the year, and soils with low water storage capacity (AGÊNCIA NACIONAL DE ÁGUAS, 2019). Therefore, considering the global shortage of quality freshwater, it is crucial to invest in public policies to preserve water sources and optimize their use and reuse, such as by treating industry and domestic waste, and brackish or saline water.

Figure 1 – Total water consumption in Brazil in 2020.

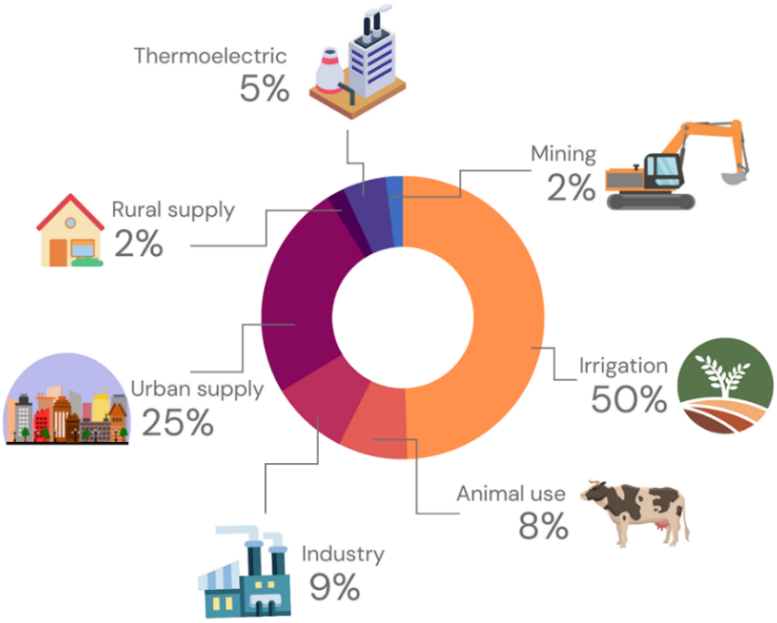

Source: adapted from reference (AGÊNCIA NACIONAL DE ÁGUAS E SANEAMENTO BÁSICO, 2022).

1.1 Water treatment

The complexity of wastewater matrixes necessitates the use of multiple technologies in wastewater treatment plants (WWTPs). For example, to achieve a drinkable standard, the effluent requires treatments in terms of harmful microorganisms, persistent organic pollutants, toxic metals, organic matter, and salinity. Consequently, a multi-stage treatment process (categorized as primary, secondary, and tertiary treatments) is necessary to fully treat the polluted water source (Fig. 2). The choice of the treatment method will be based on a combination of technical, economic and socio-environmental factors, as well as the sustainability of the process. This decision must also considers regulatory and governmental aspects, as well as social and environmental concerns (ULLAH et al., 2020). Although some methods are already well consolidated in WWTPs, there is still room for improvements and advancement in the field.

It is important to highlight that the number of stages and technologies utilized for treating a determined effluent depends on its source (municipal wastewater, river water, tannery/textile industry) and its final destination (discharge into water streams, human

consume, or industrial use). The preliminary treatment step, which removes coarse solids (plastics, papers, plant remains) and grits (sand, cinder, gravel) helps prevent damages to the downstream equipment. However, the wastewater from this stage may contains settleable and non-settleable solids, organic matter and microorganisms, thus demanding further treatment (ULLAH et al., 2020).

Figure 2 – Typical water purification combining primary, secondary and tertiary treatments with major technologies used respective to the application and class of contaminants.

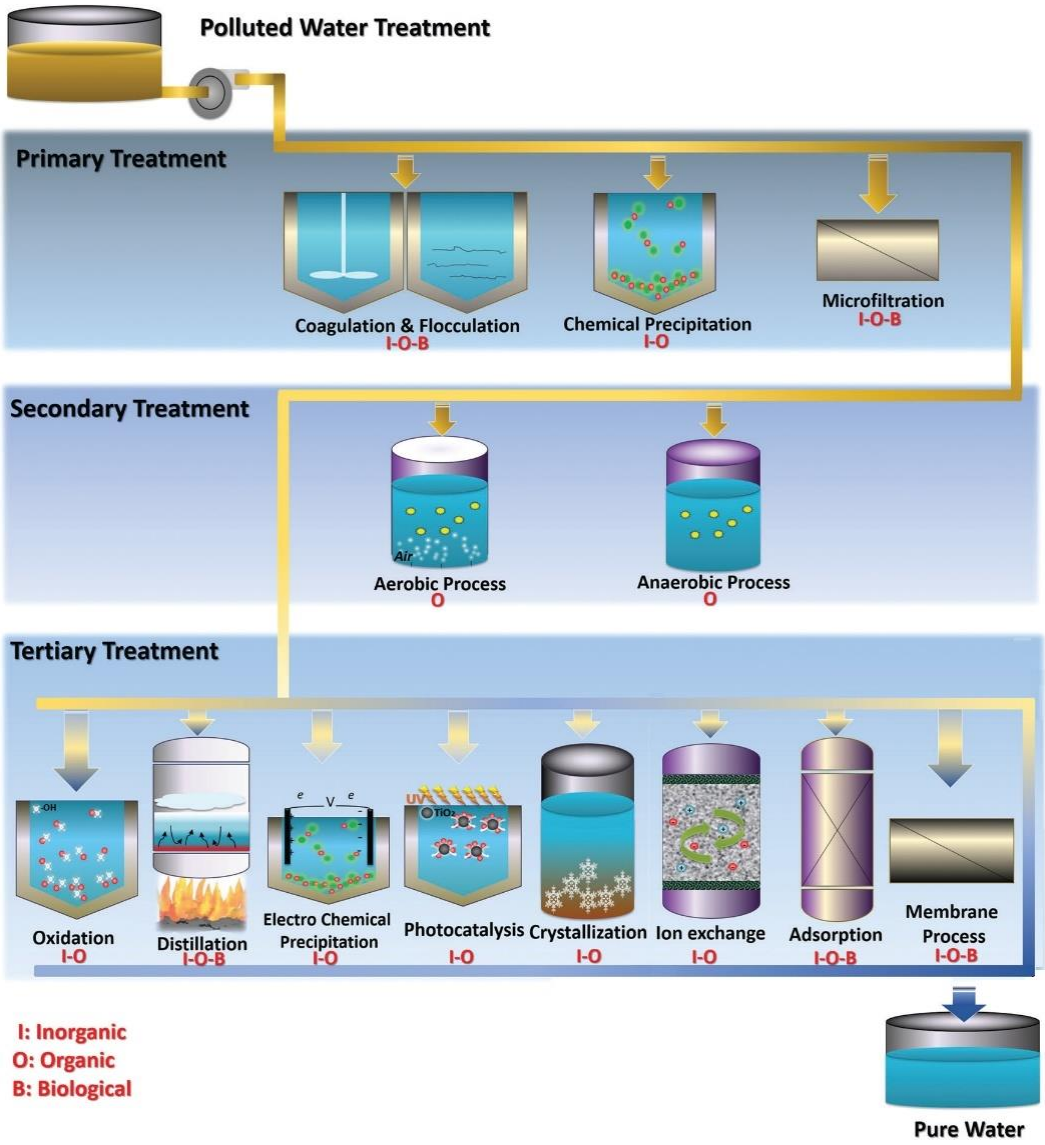

Source: adapted from reference (BOLISETTY; PEYDAYESH; MEZZENGA, 2019).

Primary treatment typically includes cost-effective and simple methods, such as microfiltration, centrifugation, sedimentation, chemical precipitation, coagulation, and flocculation used to improve the overall water quality by removing a significant portion of the organic and inorganic matter content. A secondary treatment is commonly used for organic matter degradation and is based on the use of microorganisms through aerobic and/or anaerobic processes, which convert contaminants into simpler components (such as CO_2, new biomass, biogas) (BOLISETTY; PEYDAYESH; MEZZENGA, 2019; ULLAH et al., 2020). Some attempts have been made to extend the use of microorganisms for the production of safe drinking water using biological processes to treat different water sources in terms of toxic metals, organic matter, inorganic non-metallic matter, disinfection products, etc, using methods such as sand biofiltration, biological activated carbon, trickling filter (fixed-film biofilm), and membrane bioreactor (HASAN; MUHAMMAD; ISMAIL, 2020). However, there are challenges in this approach, such as contamination by pathogenic microorganisms, selectivity toward pollutants, maintaining and monitoring of the microbial community, consumers acceptance, and implantation in developing countries. Further studies are necessary to address these challenges.

Tertiary treatment is the final stage in wastewater treatment and involves the removal of nutrients, such as phosphate and nitrate, as well as the removal of micropollutants such as disinfection by-products, pharmaceuticals, pesticides, endocrinal disrupting compounds. This stage comprises consolidated methods such as chemical oxidation, adsorption, ion exchange, and membrane processes, and emerging methods such as advanced oxidation processes, including photocatalysis, electrochemical oxidation, and Fenton/photo-Fenton (BOLISETTY; PEYDAYESH; MEZZENGA, 2019; RIZZO et al., 2019). Although widespread used in WWTPs, chlorination, ozonation and ultraviolet treatments showed to be not ideal for persistent pollutants as they can form toxic organic reaction products (RIZZO et al., 2019) and increase the risk of antibiotic resistance (AL-JASSIM et al., 2015). In this sense, advanced oxidation processes are a promising alternative, as they can remove or convert to less harmful products the organic matter through reactive hydroxyl radicals produced via a catalytic process (WANG et al., 2016c; ZHANG et al., 2016). Additionally, nanofiltration and reverse osmosis (RO) are commonly used technologies in WWTPs to remove emerging contaminants, disinfect water, reject particles, and reduce salinity (RO). Although RO is usually cost-intense, it has been successfully implemented in countries such as United States of America, Singapore

and Australia (RIZZO et al., 2019). Nevertheless, alternatives to diminish energy consume with high pressure pumps and to overcome the problem of disposal of concentrated waste streams should be further explored (SUBRAMANI; JACANGELO, 2015).

Hereupon, studies involving emerging technologies, particularly at pilot- and full scale, must be encouraged to find solutions and new approaches to provide safe freshwater supply. According to Soares (SOARES, 2020), the main drawback for implementing new technologies is, surprisingly, the satisfactory service delivered by existing assets, which makes replacements and major upgrades complex. The author also emphasizes that future works will be focused on process intensification, resource recovery and engineering systems to provide even higher quality water with net zero target at WWTPs. For example, the shortage of nutrient supplies in some countries, especially phosphorus, can strongly affect agriculture productivity, which has driven important advances in processes aimed at this problem, e.g., phosphorus recovery from sewage sludge ash.

Therefore, this thesis aims to purify water focusing in two different approaches: removal of toxic metals via adsorption and desalination of brackish water via capacitive deionization, both using carbon-based materials for their purposes.

1.2 Toxic metals removal

Toxic metal contamination of the environment, caused by human activities such as painting, mining, and tanning, is a major concern worldwide due to the potential health risks posed by these highly toxic and cumulative species. Toxic metals are highly soluble, stable and non-biodegradable, making them persistent in the environment and in organisms. They can lead to problems such as organ damage, anemia, and hormonal disorder in humans, and inhibit photosynthesis, decrease enzymatic activity, and reduce seed germination in plants (SHERLALA et al., 2018; SIONG et al., 2021). Diverse techniques are nowadays available to remove toxic metals from aqueous media, including chemical precipitation, ion exchange, electrocoagulation, nanofiltration, and adsorption (SIONG et al., 2021). Fig. 3 displays the costs of some of these technologies.

In chemical precipitation the pollutants are uptake in the form of solids that could be recovered for other applications (LI et al., 2022b). This treatment demands simple equipment and is easy to operate, however, it may generate large volumes of sludge and is not as efficient

in removing low concentration ions. Ion exchange, on the other hand, uses resins or membranes in a nondestructive and efficient process that allows for selective ion removal (ZHU et al., 2017), even so suffers from fouling by organic matter and particulates and is sensitive to pH changes. Electrocoagulation uses sacrificial anodes (Al, Fe) to generate agents that cause destabilization (Al(III), Fe(II)), which then agglomerate the contaminants. The main challenging of this technology is to reduce electricity consumption and the cost with anode replacement (SUN et al., 2018). Nanofiltration is used for its ability to retain high levels of organic pollutants and remove moderate levels of inorganic species. However, the fouling of membranes, which increases significantly the costs, and the limited flowrates are challenges for membrane filtration processes (SOYEKWO et al., 2019). Adsorption is a worldwide recognized treatment for wastewater, groundwater, industrial and domestic effluents, due to its flexible operation, cost-effectiveness, and low energy demands (CAROLIN et al., 2017; MENDOZA-CASTILLO; REYNEL-A, 2017). Therefore, since the selection of water treatment technology must be based mainly on cost, removal efficiency, feasibility, operability, and environmental impact (BOLISETTY; PEYDAYESH; MEZZENGA, 2019; MENDOZA-CASTILLO; REYNEL-A, 2017), adsorption has become the preferred choice for removing toxic metals and other contaminants (SIONG et al., 2021).

Figure 3 – Cost (upper and lower) of technologies for water treatment.

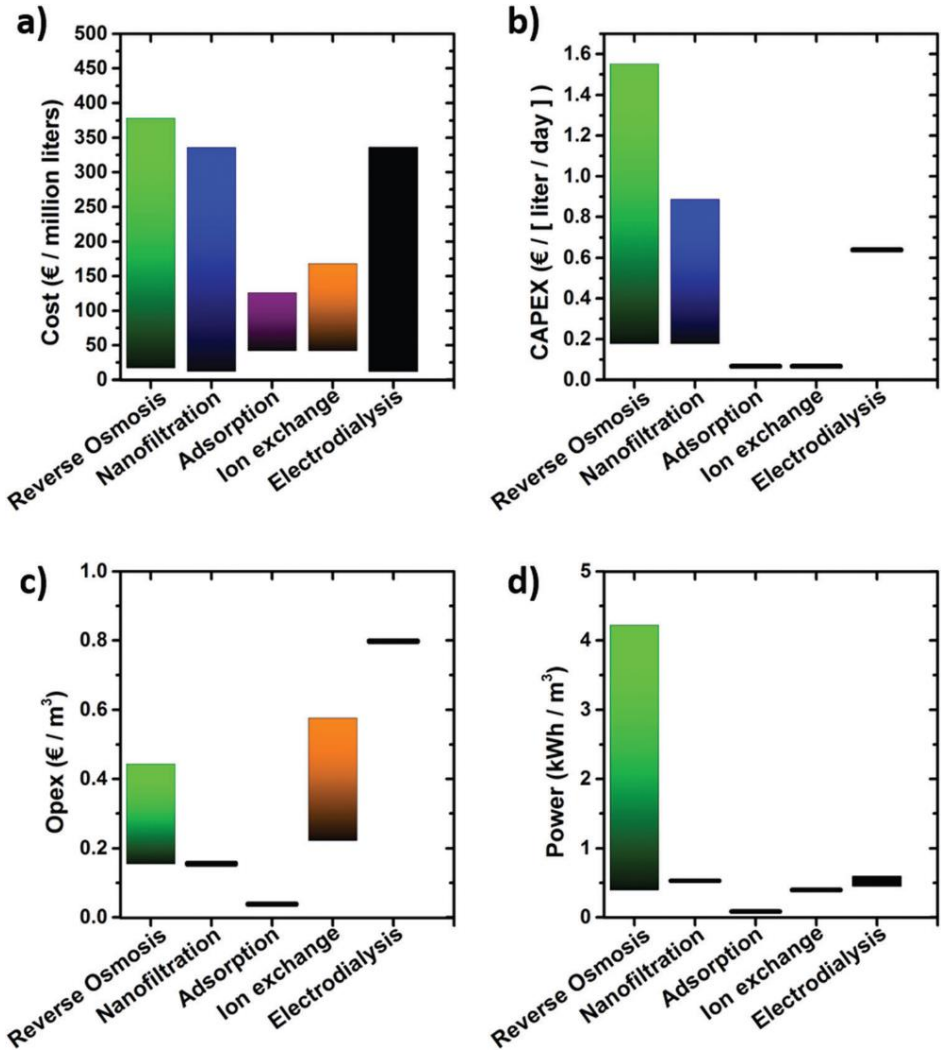

Source: reference (BOLISETTY; PEYDAYESH; MEZZENGA, 2019).

CAPEX: capital cost / OPEX: operational cost

1.2.1 Adsorption

The concept of adsorption relies on the increase of concentration of a specie (adsorbate) on the surface of a solid (adsorbent) through a mass transfer process. For water and wastewater treatment purposes, this concept is used in the removal of pollutants on the surface of several adsorbents that have been studied and developed over the years. Biosorbents (JAIN; MALIK, 2016), industrial solid wastes (SOLIMAN; MOUSTAFA, 2020), inorganic materials such as zeolites (HONG et al., 2019; RAD; ANBIA, 2021) and layered double hydroxides (FENG et al., 2022), silica- (DA'NA, 2017), and carbon-based materials (BABY;

SAIFULLAH, 2019) are examples of materials largely used for toxic metal removal in aqueous media. Among them, carbon-based adsorbents, e.g., activated carbon, biochar, carbon nanotubes, and graphene-like materials, stand out for their abundant sources and tunable properties (surface area, porosity, morphology, surface groups) (MAHESH et al., 2022). No doubt, activated carbon (AC) has been the most widely used adsorbent of toxic metals due to its high surface area, significant stability, low cost, adjustable surface and structure, and high surface reaction affinity (MAHESH et al., 2022). However, other adsorbents, particularly graphene oxide, have also gained prominence in recent years.

1.2.1.1 Graphene oxide

Graphene oxide (GO) is a single-layer of interconnected carbon atoms in an aromatic lattice, similar to graphene, containing oxygenated groups such as carbonyl, carboxyl, epoxide, and hydroxyl. These moieties make GO much more hydrophilic than graphene and allow for easy functionalization and processing, as well as for efficient adsorption of toxic metals. Due to its properties such as high surface area, low cost, and large-scale production, GO has found applications in areas such as drug delivery (OLIVEIRA et al., 2022), energy storage (LUO; ZHENG; HE, 2017), and desalination (WANG et al., 2021).

The first report of GO synthesis was by Brodie (BRODIE, 1859) in 1859, who added potassium chlorate in a slurry of graphite and fuming nitric acid. In 1898, Staudenmaier (STAUDENMAIER, 1898) improved the method by adding potassium chlorate in smaller portions over the course of the reaction and using sulfuric acid, which resulted in a highly oxidized GO. The most common method of producing GO today, known as the Hummers method, was reported in 1958 (HUMMERS; OFFEMAN, 1958) and involves the use of sulfuric acid, potassium permanganate, and sodium nitrate. Since then, several modifications have been made to the Hummers method to improve its productivity and avoid the formation of toxic gases such as NO_2 and N_2O_4 (Fig. 4). Some of these modifications include the complete removal of $NaNO_3$, pre-oxidation of graphite before adding $KMnO_4$, and the use of other oxidants, e.g., K_2FeO_4 and H_3PO_4 (YU et al., 2016). It is important to mention that after the oxidation of graphite, water and hydrogen peroxide are usually added to stop the reaction, exfoliates the product, and reduces the residual manganese ions in the form of permanganate and manganese

dioxide. However, recent studies have shown that water can further oxidize the obtained slurry (KANG et al., 2016a) and H_2O_2 can strongly affect the properties of GO (YOO; PARK, 2019).

Figure 4 – (a) Schematic synthesis of graphene oxide via modified Hummer's method and (b) images of graphene oxide synthesis.

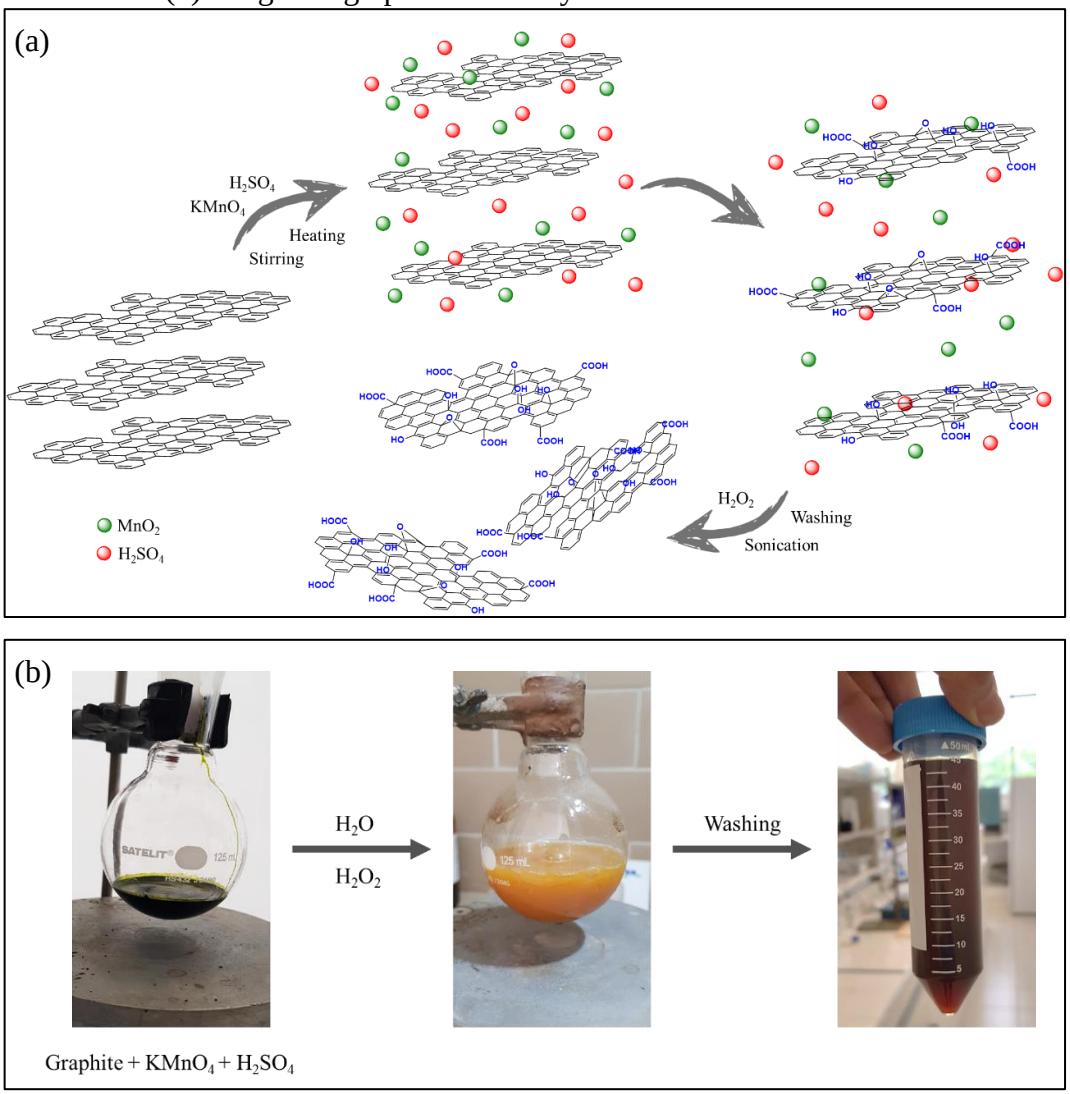

Source: the author.

GO has demonstrated outstanding adsorption capacity towards toxic metals in both single and multielement solutions. For instance, Sitko et al. (SITKO et al., 2013) investigated the adsorptive properties of GO towards Cu(II), Zn(II), Cd(II), and Pb(II) and found the maximum adsorption capacities of 294, 345, 530, and 1119 mg g^{-1}, respectively. The order of affinity, Pb(II) >> Cu(II) > Zn (II) > Cd(II), was associated to the electronegativity of the metal and the first stability constant of its associated hydroxide/acetate. However, separating GO from

solution can be difficult due to its high stability and dispersion. To overcome this issue, the preparation of magnetic composites has become the most promising strategy, offering the benefits of easy and rapid separation with application of an external magnetic field and the synthesis of materials with high adsorption capacities (DUBEY et al., 2022; KAUR; KAUR; SINGH, 2019). Magnetic GO can be synthesized by a co-precipitation method, wherein a mixture of GO and Fe(II)/Fe(III) precursors in water is heated (generally bellow 100 °C) followed by addition of an alkaline solution to promote the precipitation and the formation of the composite (DAHAGHIN; MOUSAVI; SAJJADI, 2017; DUBEY et al., 2022; SUN et al., 2015). The hydrothermal approach can also be used to produce magnetic GO (VERMA et al., 2020; WEI et al., 2015), which enables the production of uniform magnetic nanoparticles by controlling size and shape (KEERTHANA et al., 2015). However, this method may reduce part of the GO, leading to the formation of the reduced graphene oxide (rGO) (PENG et al., 2017; WEI et al., 2015), thereby reducing the number of sites available for metal adsorption.

Modifications on GO surface are used to improve its selectivity, adsorption capacity, and to decrease stacking of the sheets by attaching organic molecules containing oxygenated, nitrogenated and sulfurized functional groups (KONG et al., 2021). Sitko el at (SITKO et al., 2014) aminosilanized GO (GO-NH_2) for preconcentration of Pb(II) and stated a superior selectivity compared to bare GO, although the maximum adsorption capacity has decreased from 364 mg g^{-1} (GO) to 96 mg g^{-1} (GO-NH_2). Lee et al. (LEE et al., 2020) studied the impact of primary and secondary amines on the removal of Cr(VI) by GO grafted with silylation agents containing an increasing number of amine groups. The authors observed a maximum adsorption capacity following the order pN-GO (189.47 mg g^{-1}) < psN-GO (208.22 mg g^{-1}) < pssN-GO (260.74 mg g^{-1}), where p = primary, s = secondary, and N = amine. They attributed the best performance of pssN-GO to the increased number of nitrogen atoms on the structure and the easier protonation of secondary amines. Pirveysian and Ghiaci (PIRVEYSIAN; GHIACI, 2018) synthesized a sulfur-functionalized GO that adsorbed Pb(II) (285 mg g^{-1}), Cd(II) (217 mg g^{-1}), Ni(II) (175 mg g^{-1}), and Zn(II) (196 mg g^{-1}), outperforming previous materials. Although there are several studies for toxic metal adsorption using modified GO, the use of magnetic functionalized GO composites is still in progress and demands further investigation, especially when ion selectivity is desired, since GO exhibits high affinity for diverse metallic species.

1.3 Desalination

Desalination-based technologies are a potential solution for obtaining freshwater from saline and brackish water, and are generally divided into two groups: one based on membrane use, such as reverse osmosis (RO) and electrodialysis (ED), and the other one on thermal energy for evaporation, such as multi-stage flash (MSF) distillation, multi-effect distillation (MED), and vapor compression (VC) (AL-KARAGHOULI; KAZMERSKI, 2013). These conventional desalination processes are known to require intense energy input, which is related to several factors as the type of desalination process (RO, MSF, MED, etc.), feed water quality, water salinity (saline or brackish water), plant dimension, and energy recovery capacity. So, a significant impact on operating cost is expected in terms of energy demand (SEMIAT, 2008). It is also important to notice that the energy depends on the desalination process employed, wherein membrane-based processes are electrical energy driven, while thermal-based processes are electrical and thermal energies driven. By comparing these two technologies, membrane desalination requires less energy than thermal desalination (ELSAID et al., 2020). For example, MSF and MED plants demand more energy than RO plants, wherein RO costs rely mainly on the replacement of onerous membranes; regarding these three technologies, and considering the major types of desalination plants worldwide, RO produces water at a lower cost (0.45 \$ m^{-3} for RO and 0.52 \$ m^{-3} for MSF and MED) (ANDERSON; CUDERO; PALMA, 2010).

In terms of water salinity, for membrane-based processes (RO, ED), desalination of seawater demands more energy than desalination of brackish water, whereas distillation processes (MSF, MED, VC) do not suffer from the influence of water salinity. In general, RO has been demonstrated to be the most economical desalination technology due to the development of membranes with longer life and lower pressure requirement. However, when the process driven by thermal energy uses heat supplied by another source, e.g. by-product of the electricity power plant, or when the feed water has a salt concentration over 60,000 ppm, distillation processes are the best cost-saving technologies. Moreover, for desalination of brackish water, with total dissolved solids (TDS) ranging from 3,000 – 10,000 ppm, both RO and ED are economically viable: for a TDS from 5,000 to 10,000 ppm, RO is more cost-effective; for lower TDS, or when high water recovery is demanded, ED is the best option (AL-KARAGHOULI; KAZMERSKI, 2013).

In this context, technologies that dispense the use of membranes and thermal energy are essential to decrease the costs of freshwater production. Especially when it comes to people more exposed to water scarcity, these efforts are highly necessary to facilitate the access to quality water. Therefore, capacitive deionization (CDI) has emerged as a promising water treatment technology attracting the attention of the scientific community (ANDERSON; CUDERO; PALMA, 2010; CHOI et al., 2019; LIU et al., 2021; PORADA et al., 2013; SUSS et al., 2015).

1.3.1 Capacitive deionization

The "electrochemical demineralization of water" was first introduced in 1960 with the work of Blair and Murphy (BLAIR; MURPHY, 1960), wherein ions would be removed from solution when specific groups on the surface of carbon electrodes undergo either reduction or oxidation reactions with consequent formation of ionized groups. Later, Murphy and co-workers developed a desalination system that used activated carbon electrodes (MURPHY et al., 1965) and described the desalination process based on a capacitive mechanism, through a combination of mass balance and transport equations (MURPHY; CAUDLE, 1967). In the early 1970s, Johnson et al. (JOHNSON; NEWMAN, 1971; JOHNSON et al., 1970) brought important contributions to the fundamentals of CDI and proposed the theory of "potential-modulated ion sorption", currently known as Electric Double Layer Theory (EDL), as the mechanism of ion removal. In the 1990s, the studies focused on the development of effective carbon electrodes. A carbon aerogel prepared by Farmer et al. (FARMER et al., 1995), and used for the first time in CDI, gained prominence due to its monolithic structure, large surface area, good conductivity, and immobilization of the carbon matrix, dispensing the need for membrane separators, which had previously been used to prevent carbon detachment. Despite starting decades ago, CDI has only recently received more attention from the scientific community (Fig. 5), making its development relatively recent compared to other desalination techniques.

Figure 5 – Number of publications per year by searching “capacitive deionization” in Web of Science database (29/03/2023).

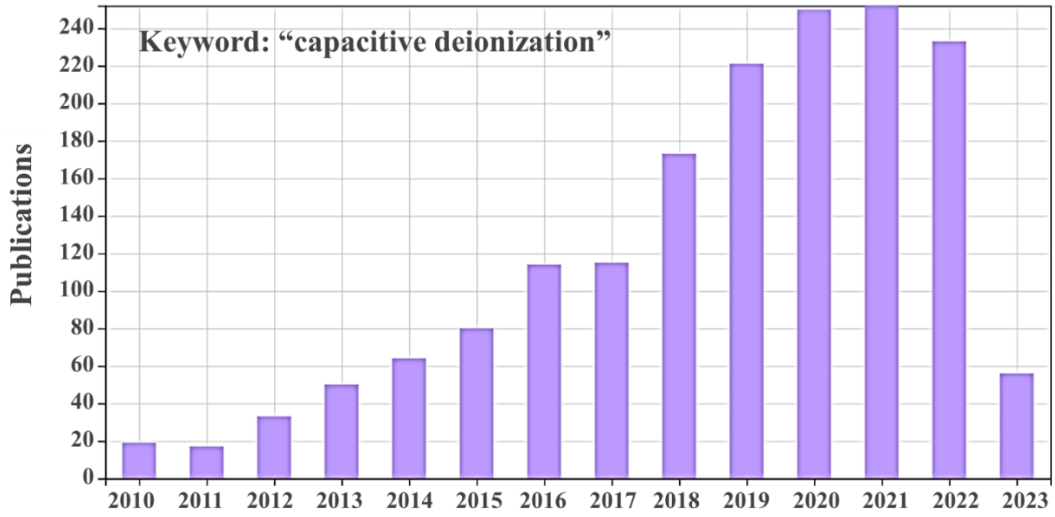

Source: adapted from Web of Science (2023).

In CDI, ions are removed from water via electrosorption by applying a low potential difference or current to a pair of electrodes (or stacks of multiple pairs) placed opposite each other (Fig. 6). The electrodes polarized force the ions to be removed and stored in the EDL formed at the electrode/electrolyte interface, similar to what occurs in electrodialysis and using the same concept of electrical capacitors. In summary, the EDL-model states that there can be charge separation at the electrode/electrolyte interface, wherein the pores of the electrodes have an excess of electronic charges locally compensated by counterions from the electrolyte. Once the pores in the electrodes are saturated with electrosorbed ions and the storage capacity is achieved, the ions are released by lowering or removing the applied potential. This restores the removal capacity of the electrodes and, considering no side reaction, allows for long-term operation (PORADA et al., 2013). Besides, since the technology is primarily based on a capacitive mechanism, part of the energy dispended during electrosorption could be recovered in electrode regeneration (ANDRES; YOSHIHARA, 2016).

Figure 6 – Schematic representation of a capacitive deionization process.

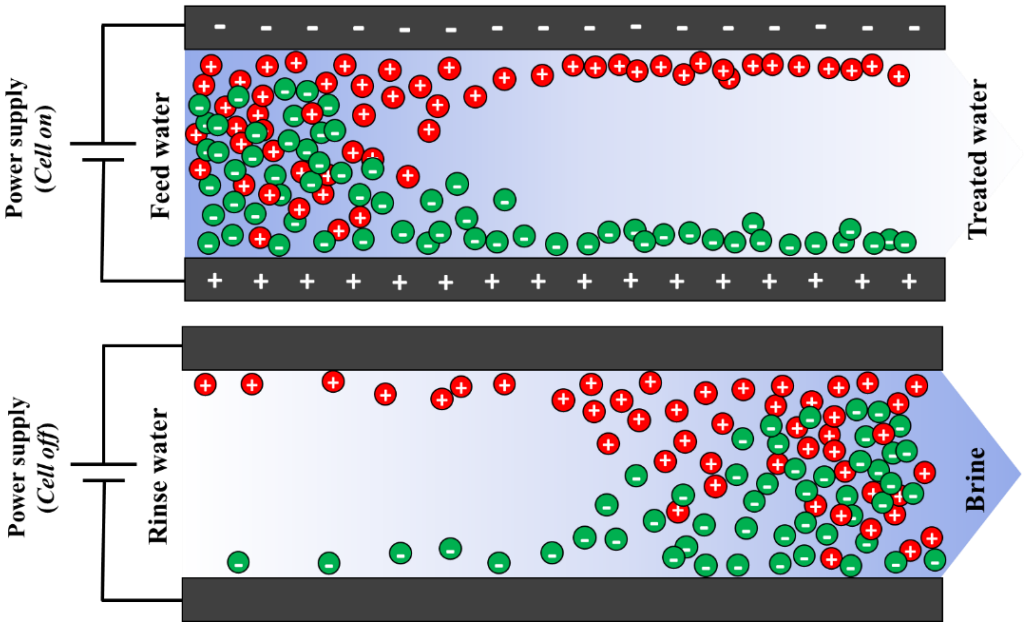

Source: the author.

Considering energy aspects for process cost, CDI could directly compete with the conventional desalination methods, since the energy could be partially recovered at each adsorption/desorption cycle (capacitive behavior) and due to the possibility of a membrane-free operation that results in a low-pressure process. Additionally, under determined conditions and working in moderate to high round trip efficiencies (percentage of energy that can be recovered from the charging process), CDI can be considered a candidate for RO replacement, especially when it comes to brackish water desalination (ANDERSON; CUDERO; PALMA, 2010; LIU et al., 2021; SHARAN et al., 2021). Other advantages is the water quality easily adjusted by tuning potential, current and flow conditions, for example, (ZHAO; BIESHEUVEL; VAN DER WAL, 2012) and the system less susceptible to fouling by biological growth and/or salt incrustation (WANG; LIN, 2018).

1.3.1.1 Performance metrics

The evaluation of CDI desalination performance has been studied using different parameters related to energy demand, throughput, and materials metrics. In a review article, Hawks et al (HAWKS et al., 2019) discussed some important metrics to describe and compare desalination processes, distinguishing them in performance metrics, related to generic

desalination performance, and performance indicators, which provide insight into specific performance metrics. Together, they are relevant when comparing different materials, cell setups, and operational conditions to evaluate whether the device is suitable for CDI application. These metrics should be calculated at the dynamic-steady state (DSS) charge/discharge cycle, where the effluent conductivity begins and ends at the same value, which can be achieved after few cycles under a given experimental condition. In the following text, a brief overview of some of these parameters will be provided.

The most common variables used in CDI studies are salt adsorption capacity (*SAC*, in mg g^{-1}), average salt adsorption rate (*ASAR*, in mg g^{-1} min^{-1}), salt concentration reduction (Δc, mmol L^{-1}), energy consumption per mol of salt removed (E_m, J mol^{-1}), energy normalized adsorbed salt (*ENAS*, in μmol J^{-1}), and specific energy consumption (SEC^{-1}, in mg J^{-1}) (HAN; KARTHIKEYAN; GREGORY, 2015; HEMMATIFAR et al., 2016; OUYANG et al., 2018a; WANG; LIN, 2018). However, Hawks et al stated that the energy consumed per m^3 of treated water (E_V, in Wh m^{-3}) and the productivity (P, in L h^{-1} m^{-2}) should also be considered since they are in function of the volume of treated water, which would be more important for practical applications. Hereupon, energy consumption would impact on operating cost (expenses incurred on the day-to-day operation of a device, of a business, etc.) and productivity would impact on capital cost (fixed, one-time expenses incurred on the construction, enhancement, or acquisition of assets). Therefore, these parameters would facilitate comparisons between CDI and other desalting technologies. Except for *SAC*, the aforementioned variables were considered as performance metrics (HAWKS et al., 2019).

Regarding performance indicators, *SAC*, capacitance (C, in F), specific capacitance (C_{sp}, in F g^{-1} or F cm^{-3}), charge efficiency (Λ_{cycle}, in %), among others are used to better understand the performance results obtained by different CDI configurations and materials (HAWKS et al., 2019). Capacitance is the capability of an electrode to store charges when a difference of potential is developed in parallel electrodes. In turn, the capacitance normalized by the electrode mass or volume is the definition of specific capacitance. These parameters can be calculated from cyclic voltammetry, galvanostatic charge/discharge curves and electrochemical impedance spectroscopy measurements and can predict, or at least suggest, whether the electrodes will exhibit a good performance in desalination (LADO et al., 2019a; SHI et al., 2016; XU et al., 2015). Additionally, charge efficiency measures the percentage of moles of salt removed in the CDI process related to the theoretical number of moles that should

have been removed with the charge input during the charging step. In general terms, it evaluates how the input charges are driven in the CDI process (HAWKS et al., 2018; HEMMATIFAR et al., 2016; PORADA et al., 2013).

Although CDI would ideally work through a capacitive process, wherein ions are accumulated in the EDL, in real-world conditions, the electrochemical cell is frequently exposed to Faradaic reactions at the anode (Equations 1 and 2) (HE et al., 2016) and cathode (Equations 3 and 4) (VANÝSEK, [s.d.]). These Faradaic processes negatively impact the charge efficiency and the life cycle of the electrodes (TANG et al., 2017). They consume part of the energy input for desalination, that is, the electrons delivered to the system are consumed by parallel reactions and more energy is necessary to perform the desalination (HEMMATIFAR et al., 2016; QU et al., 2016). Depending on working conditions, such as applied voltage and current (HEMMATIFAR et al., 2016), mode of operation (constant voltage or constant current mode) (QU et al., 2016), flow mode (flow through or flow by) (REMILLARD et al., 2018a), and level of dissolved oxygen in water (HE et al., 2016), the electrodes would be more or less affected by these reactions.

$O_2 + 4H^+ + 4e^- \leftrightarrow 2H_2O$	$E^0 = -1.23$ V/SHE	(1)
$CO_2 + 4H^+ + 4e^- \leftrightarrow C + 2H_2O$	$E^0 = -0.9$ V/SHE	(2)
$2H_2O + 2e^- \leftrightarrow H_2 + 2OH^-$	$E^0 = -0.828$ V/SHE	(3)
$O_2 + 2H_2O + 2e^- \leftrightarrow H_2O_2 + 2OH^-$	$E^0 = -0.146$ V/SHE	(4)

Another factor influencing Λ_{cycle} is co-ion expulsion. Co-ions are ions with the same charge of a given electrode and counterions are ions with opposite charge of a given electrode. Therefore, an anion is the counterion of the anode and the co-ion of the cathode. After electrode polarization, there are two ways to balance the accumulated charges: by adsorbing a counterion or expelling a co-ion. Thus, co-ion expulsion “consumes” input charges, decreasing Λ_{cycle} and affecting the overall performance of desalination. The use of ion exchange membranes (membrane capacitive deionization, MCDI) can overcome this issue by using an anion exchange membrane in front of the anode and a cation exchange membrane in front of the cathode (Fig. 7). This prevents co-ions from leaving the electrode structure resulting in accumulation in the macropores instead of being released into the spacer channel (as in CDI). Thus, in order to maintain electronegativity, more counterions pass through the membranes and

are stored in the macropores, which increases charge efficiency and enhances salt removal. Reversing the cell potential in MCDI is also made possible as the ion exchange membranes prevent re-adsorption of ions. This results in a faster desorption and greater release of adsorbed counterions compared to CDI, where the cell must be discharged at zero volt (ZHAO; BIESHEUVEL; VAN DER WAL, 2012).

Figure 7 – Schematic representation of charge/discharge processes in MCDI.

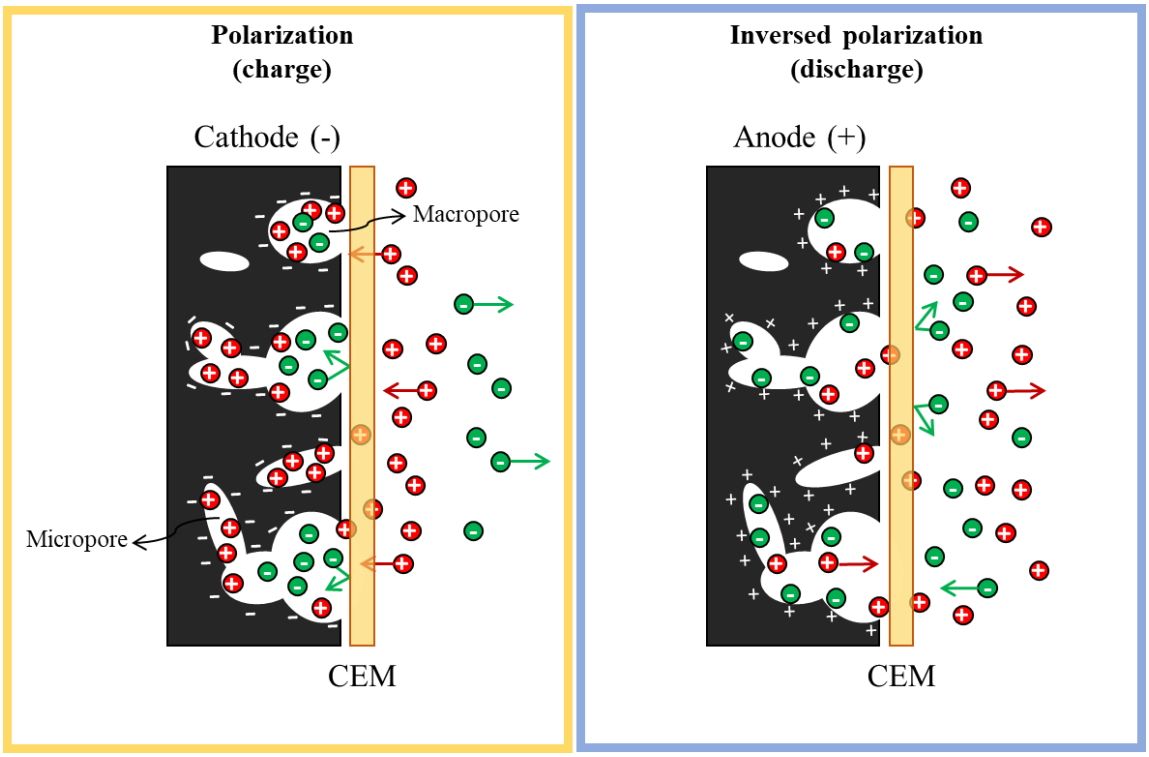

Source: the author.

CEM = cation exchange membrane.

Along with Faradaic reactions and co-ion expulsion, energy loss in CDI devices can also occur through power dissipation in resistive components (ohmic losses), such as low conductive electrolytes and resistive connections/current collectors (GARCÍA-QUISMONDO et al., 2013a). A detailed study of Hemmatifar et al. (HEMMATIFAR et al., 2016) suggests that parasitic (Faradaic reactions) and resistive losses are the main contributors to energy loss in CDI devices. The resistive losses were further categorized into series resistive loss (associated with wires resistance, interfacial contact between electrodes and current collectors, ionic resistance in spacers) and non-series resistive loss (associated with ionic resistance within the

electrode pore). The study also observed that parasitic losses are more significant at high potentials while resistive losses are more pronounced at high currents.

1.3.1.2 Electrode materials

Fundamental for the success of a CDI process, the materials used for electrode preparation are certainly one of the most important factors affecting desalination. For an electrode with high performance, one must take into account some characteristics the material should exhibit, such as (i) large specific surface area (SSA), (ii) high stability over a large pH and voltage range, (iii) interconnected pore structure allowing ion mobility, (iv) high electric conductivity and wettability, (v) low cost, and (vi) good processability and scalability (OREN, 2008). In this sense, carbon-based materials such as activated carbon (JUCHEN et al., 2022; LADO et al., 2019a; ZORNITTA et al., 2017), mesoporous carbon (DUAN et al., 2015a; LI et al., 2009), carbon nanotubes (LIU et al., 2014), graphene (LI et al., 2018a; WANG et al., 2016a), and their composites (CHEN et al., 2012; LEE et al., 2018) have been extensively used as electrodes for CDI purposes (JIA; ZHANG, 2016; LIU et al., 2015b) and energy storage devices (CHEN; PAUL; DAI, 2017). More specifically, AC has been widely studied in CDI field because it meets many of these requirements (LADO et al., 2019b; SANTOS et al., 2018; ZORNITTA; RUOTOLO, 2018), being the most commercially material used in water treatment systems due to its relatively easy production (and in large scale) and to the several sources it can be obtained (wood, coal, rice, starch, coconut shell, resins).

Although AC has advantages over other carbon-based materials, the dominant presence of micropores on its structure hinders the effective access of the electrolytes to inner pores. This issue makes ion diffusion difficult throughout the pore network (VAQUERO et al., 2012), limiting the electrode capability of salt removal. Despite micropores are the mainly responsible for providing high SSA and adsorption sites for deionization, the presence of larger pores (meso and macropores) is desired to decrease the resistance to mass transfer, to allow ion access to inner micropores, and to improve the kinetics of desalination (JUCHEN et al., 2022). Under this perspective, materials with different pore size distributions are beneficial for CDI applications (CUONG et al., 2021; OUYANG et al., 2018b; ZORNITTA et al., 2016).

Porosity in carbonaceous materials can be created through physical (using O_2, CO_2 or steam) or chemical (using KOH, H_3PO_4, $ZnCl_2$) activation, which generally results in

materials with a narrow distribution of micropores (CUONG et al., 2021). Pore structure can be adjusted by modifying some synthesis parameters, such as activation temperature, time of activation, and the reactant-to-carbon ratio (during impregnation step in chemical activation) (LI et al., 2022a), and it varies according to the carbon source (LI et al., 2018b; ZHAO et al., 2016). An interconnected structure can be designed through a templating method that uses porous inorganic solid-state hard-templates, e.g. mesoporous silica, or soft organic materials, e.g. block copolymers, to form self-assembled structures. Nevertheless, hard templating can be challenging to scale-up and demands a post-synthesis extraction using corrosive chemicals (HF, NaOH). Soft templating can be challenging to control the morphology and costly due to expensive and non-renewable surfactants and copolymers used (CUONG et al., 2021). An alternative is to combine commercially available materials with different pore structures, which would enable the preparation of hierarchical electrodes. In this sense, the goal is to create an electrode containing macro, meso and micropores instead of an hierarchical carbon material itself (REALE; SMITH, 2018).

Recently, Wang et al. (WANG et al., 2019) successfully coated graphite felt (GF) with AC for CDI applications, resulting in a stable and promising platform for large-scale CDI, combining the macroporosity of GF and the high surface area of AC. GF is a macroporous material, with a 3D pore network, high mechanical stability, outstanding electric conductivity, and widely used for energy storage and environmental applications (HUONG LE; BECHELANY; CRETIN, 2017). However, its use in CDI devices is scarce (LADO et al., 2021a).

The study by Wang et al. did not investigated the effect electrode thickness or mass loading of active material on CDI performance, which have been shown to be important factors (KIM et al., 2014; LEE et al., 2018; WANG et al., 2011; ZORNITTA et al., 2016). For example, Santos et al. (SANTOS et al., 2018) found that the capacitance in terms of volume (17 vs. 20 F cm^{-3}) did not depend significantly on electrode thickness (50 vs. 180 µm). One could expect a considerably increase in volumetric capacitance with electrode thickness, however the thicker electrode had a much higher density of AC (451 vs. 212 mg cm^{-3}), which limited ion access to the inner pores, as the AC particles would be more compacted, and reduced the number of sites for ion adsorption. Additionally, Liu et al. (LIU et al., 2017b) remark that increasing the thickness of electrodes with high mass loading can increase internal resistance, reducing specific capacitance and energy density due to a more packed structure that restricts

electrochemically active surface area. However, they found a nonlinear dependence between internal resistance and electrode thickness. By using a theoretical model and from experimental data analysis, the optimized electrode thickness was determined to be 53.1 µm, wherein the internal resistance would be minimal and capacitance maximum. In this sense, further studies are needed to understand the effect of electrode thickness on CDI performance as the relationship is not yet well understood (BASIRICÒ; LANZARA, 2012).

1.3.1.3 Operational modes

Over the decades, advances in CDI studies allowed the development of different operational modes to optimize the desalination process. For example, CDI experiments can be performed using either single-pass or batch-mode approaches to measure salt concentration over time. In single-pass mode (Fig. 8a), a solution from a storage vessel is continuously introduced into the cell and salt concentration is evaluated immediately at the outlet of the device (LADO et al., 2021a; WANG et al., 2019). Initially, it is observed a decrease in effluent concentration; then, after electrode saturation, the concentration of the exit solution starts to increase until the level of the inlet solution. On the other hand, in batch-mode configuration water is recirculated in a small vessel wherein ion concentration is evaluated (HAN et al., 2013; WANG et al., 2016b). Once the electrodes reach full adsorption capacity, water salinity reaches a minimum that remains virtually steady over time (Fig. 8b). In general terms, experiments performed using the single-pass method would be more interesting, since they would be closer to real conditions. Although batch-mode allows simpler analysis, recirculation makes the process less efficient (PORADA et al., 2013).

Figure 8 - Different operational modes used in capacitive deionization studies. (a) Single-pass and (b) batch-mode methods, and (c) constant current and (d) constant voltage modes.

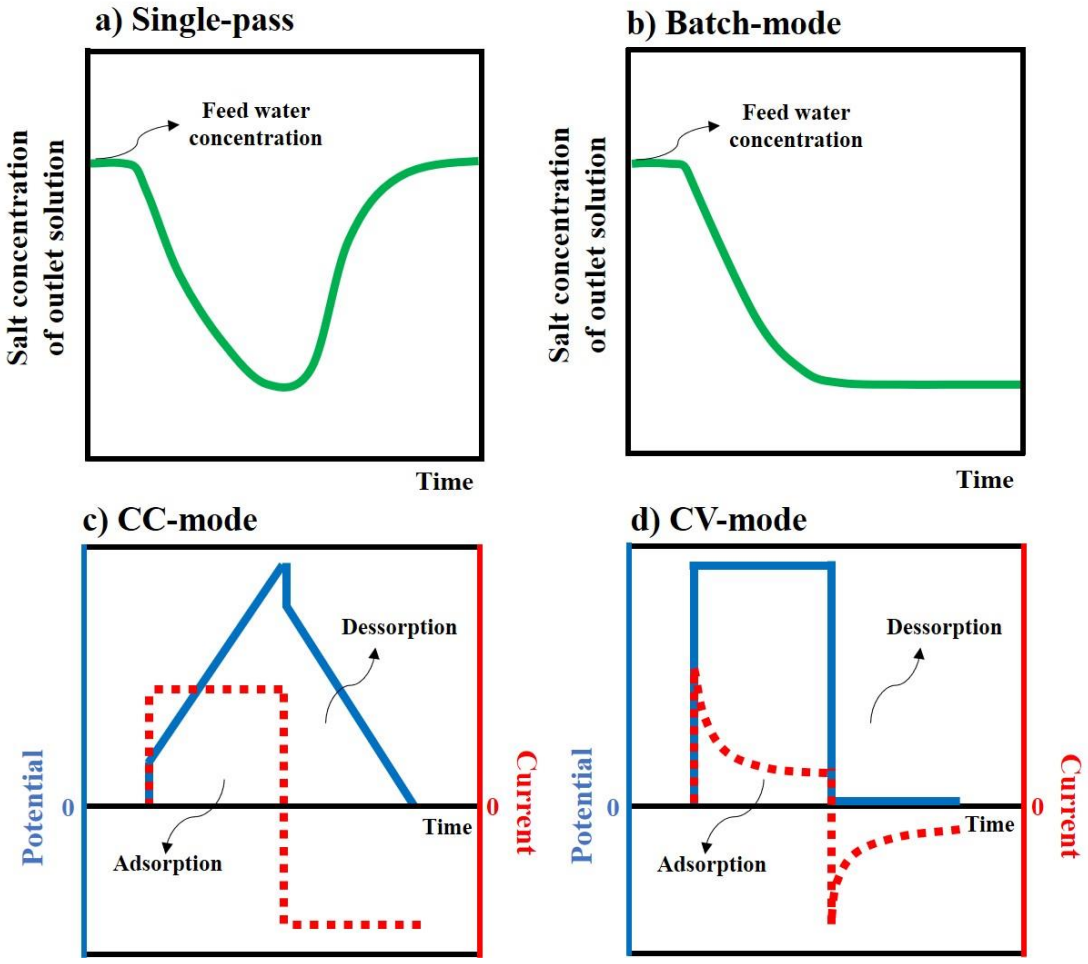

Source: the author.

Another factor influencing CDI performance is how the electrodes are charged and discharged, which directly affect adsorption and desorption processes, therefore parameters such as adsorption capacity and energy consumption, for example. In summary, two modes are employed in CDI studies, one involving constant voltage operation and the other constant current operation (CC). In CC-mode, illustrated in Fig. 8c, the electrodes are charged using a constant current, and a difference of potential is gradually developed until a pre-established value. Otherwise, in constant voltage mode (Fig. 8d), a voltage is applied to the electrodes and the current reaches a maximum with subsequent decrease until a nearly constant value. Accordingly, for adsorption in CC operation, the effluent salinity diminishes and remains fairly constant at a low level until electrodes saturation. For adsorption in constant voltage operation,

the effluent concentration first decreases abruptly and then starts to increase again until the water feed concentration level. After promoting the desalination, the CDI cell is short-circuited (zero voltage) or discharged at constant current, leading to the release of ions as a discharged brine (DYKSTRA et al., 2018; PORADA et al., 2013; QU et al., 2016; ZHAO; BIESHEUVEL; VAN DER WAL, 2012).

Although CDI studies under constant voltage operation are more common in both the academic and commercial areas, CC mode has increasingly gained space for its advantages over constant voltage-CDI (DYKSTRA et al., 2018; KANG et al., 2014; KIM et al., 2015; PORADA et al., 2013). Firstly, constant current operation leads to a nearly constant effluent salinity that can be easily adjusted by changing the current value or the water flow rate (ZHAO; BIESHEUVEL; VAN DER WAL, 2012). Secondly, energy consumption using CC mode is lower (KANG et al., 2014; ZHAO; BIESHEUVEL; VAN DER WAL, 2012), since the cell reaches the desired voltage at the end of the charging process, leading to a lower average cell voltage (KIM et al., 2015). This can be also related to less power dissipation through resistive components (ohmic losses) since the applied current is controlled. Moreover, the electrodes are less exposed to the occurrence of parasitic (Faradaic) reactions (redox reactions on the surface and within the electrodes). The losses associated with these two processes (ohmic and Faradaic) are responsible for consuming part of the energy input for desalination (QU et al., 2016). Furthermore, the energy stored during ion removal (charging step) can be recovered in ion desorption (discharging step) (DŁUGOŁECKI; VAN DER WAL, 2013; GARCÍA-QUISMONDO et al., 2013b; KANG et al., 2016b; OYARZUN et al., 2020). It is reported that energy recovery in CC-CDI is easier attainable and occurs in a higher extent than in constant voltage-CDI (HAN; KARTHIKEYAN; GREGORY, 2015).

1.3.1.4 Capacitive deionization: a versatile technique

Although an extensive number of CDI publications are centered on removal of salt (NaCl) from brackish water, a recent review explores the possibilities of CDI application in the treatment of wastewater and outlook some challenges for its use as an emerging technology in WWTPs (KALFA et al., 2020). For example, CDI has the potential to remove and recover toxic metals, which is desirable from both environmental and economic perspectives. However, since the technique is based on the adsorption driven by electrostatic forces, the design of selective electrodes is challenging. In this way, researchers have explored various strategies to promote ion selectivity in CDI, including (i) the use of selective ion exchange membranes to promote a preferential transport of ions (SHI et al., 2019), (ii) the use of intercalation materials such as manganese oxides (LEONG et al., 2021) and MXene (CHEN et al., 2020), (iii) tuning the micropore size of the electrode material (SUSS, 2017), and (iv) modifying the micropore surface chemistry (GUYES; MALKA; SUSS, 2019). According to the authors of the review (KALFA et al., 2020), investing in the design of selective ion exchange membranes for CDI would be a more practical approach than designing selective electrodes, as the latter requires a more complex production process to create the desired pore network.

The presence of micropollutants in wastewater is a major concern in WWTPs, and there are several strategies for removing them, including nanofiltration, reverse osmosis, advanced oxidation processes (as previously seen in section 1.1), and CDI. For example, the concomitant removal of salts and trace of uncharged organic contaminants (TOrCs) was performed by Lester et al. (LESTER et al., 2020) . In this work, the adsorption of bisphenol A, carbamazepine, estrone, and pentoxifylline was based on the partition coefficient between the solution and the electrode, and the removal increased with hydrophobicity (pentoxifylline < carbamazepine < estrone < bisphenol A). Moreover, the electrosorption of the TOrCs was not affected by the salt concentration.

It is known that, depending on the applied potential, Faradaic reactions can take place in CDI systems, which could be used as strategy to direct or indirect electro-oxidize contaminants, as well as to remove them through electrosorption (KALFA et al., 2020). Duan et al. (DUAN et al., 2015b) used CDI to simultaneously remove organic pollutants (phenol) and inorganic salts (NaCl) by combining electrochemical oxidation and electrosorption using AC electrodes. Phenol removal occurred via different mechanisms, including indirect oxidation via

chlorine species (ClO^-), direct oxidation on electrode surface, and electrosorption, while NaCl was removed via electrosorption. The occurrence of direct and indirect oxidation reactions was possible due to the high potentials applied (2.0 V), which, on the other hand, caused the performance of the cell to deteriorate. To overcome this, the authors applied a reverse potential, which allowed for full recovery of the cell.

The main drawback to CDI setups used to treat water containing dissolved organic matter is the fouling of membranes in MCDI fashion and the clogging of carbon pores in the electrodes. As showed by Mossad and Zou (MOSSAD; ZOU, 2013a), the presence of humic acid (measured by the total organic carbon (TOC) concentration) reduces the efficiency of carbon electrodes due to fouling. For instance, the removal capacity toward inorganic salts decreased after 17 h of operation with a feed stream containing 0.9 mg L^{-1} of humic acid. On the other hand, the efficiency of electrosorption remained at 87.7% during 30 h of operation with a feed solution containing only NaCl. Moreover, increasing TOC concentration from 0.9 to 3.1 mg L^{-1} gradually decreased the adsorption performance from 85% to 70.2% and reduced the produced flow rate from 2 to about 1.25 L min^{-1}. In this work, applying an opposite polarity in the regeneration step was insufficient to promote organic matter removal from the electrodes, while using an alkaline solution resulted to be effective, as confirmed by other authors (HASSANVAND et al., 2019).

Over the years, CDI has shown to be a versatile technique with promising application in different water treatment purposes beyond water desalting (Fig. 9). In view of this, studies related to (i) energy recovery, (ii) long-term operational stability, (iii) the impact of foulants agents and regeneration treatments on electrode performance, and (iv) scaling up from laboratory to pilot- and full scale should further be explored aiming the competitive use of this technology.

Figure 9 – Possible uses of CDI technology for water treatment purposes.

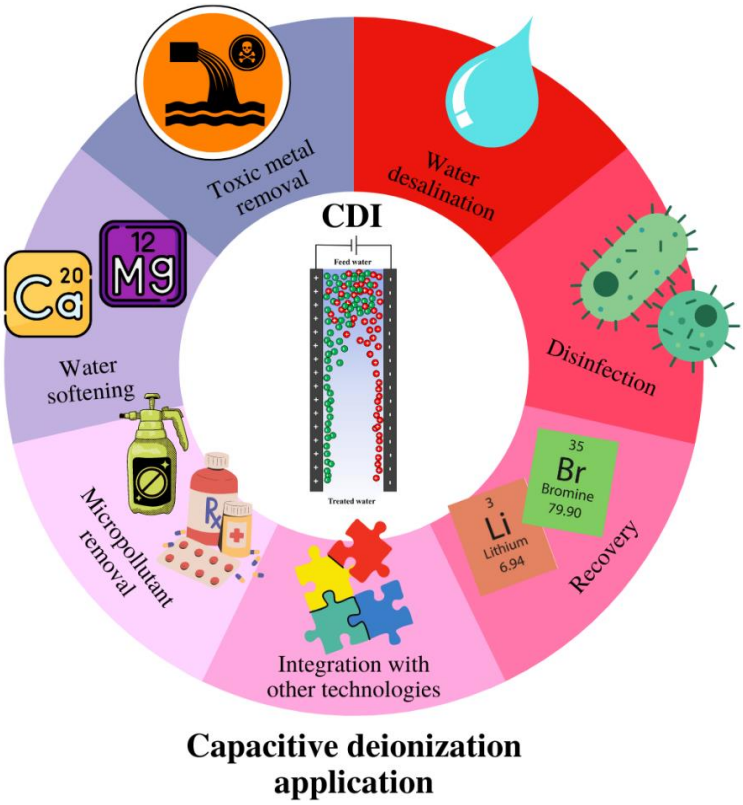

Fonte: the author.

1.4 Objectives and thesis outline

In this thesis, carbon-based materials were used for water treatment purposes from two perspectives: adsorption of toxic metals and capacitive deionization. The document was organized into chapters for better presentation of results.

Chapter II focused on synthesizing magnetic graphene oxide composites with different contents of GO and evaluating their ability to adsorb Cd(II), Cu(II) and Cr(VI) in a multielement solution. Then, one of the composites was functionalized with amino groups to enhance Cr(VI) selectivity. Characterization techniques and adsorption studies were performed to understand the mechanism of adsorption and the selectivity of the final composite.

Chapter III investigates strategies to improve capacitive deionization performance using 3D electrodes of activated carbon supported on graphite felt. For this purpose, the effect of electrode thickness, mass loading, and AC distribution over GF was evaluated in terms of

salt adsorption capacity, kinetics, water production, and energy consumption. The results highlight the crucial role that electrode preparation plays in desalination.

Chapter IV summarizes the main findings of the developed works. The scientific production of the author during the doctorate period (Chapter V), appendixes and bibliography are also included.

2 CHAPTER II – FUNCTIONALIZED MAGNETIC GRAPHENE OXIDE COMPOSITES FOR SELECTIVE TOXIC METAL ADSORPTION

In this work, composites of magnetite and graphene oxide were modified with amino groups to improve chromium selectivity in a multielement solution containing Cd(II) and Cu(II) ions. The results achieved from characterization techniques such as Fourier transform infrared, Mossbauer spectroscopy, and X-ray photoelectron spectroscopy, confirmed the effectiveness of the synthesis and evidenced different moieties able to promote metal adsorption. Comparing the unmodified composites with the silanized one, it was observed an enhancement in Cr(VI) uptake of 86% relative to Cd(II) and 23% relative to Cu(II). This effect was attributed to the hard-hard interactions between the Cr(VI) species $HCrO_4^-$ and the NH_3^+ groups, along with electrostatic interactions, which improve the adsorption of negative chromium species. The metal adsorption by the composites followed the Langmuir model and a pseudo-second order kinetic, and the surface charge played an important role in the adsorption. Finally, reuse experiments showed an adsorption of approximately 100% of Cr(VI) over 5 cycles, underlining the remarkable stability of the produced amino grafted material.

2.1 Introduction

The rapid growth of industrialization around the world has been accompanied by several negative impacts, particularly in the area of wastewater management. One major challenge is the disposal of toxic metals from industries such as fuel, paper, pesticides, and metal plating, which poses a significant threat to human health and ecosystems due to their high toxicity, persistence, non-biodegradability, and cumulative effect. The presence of toxic metals in the human body can result in the disruption of cellular metabolism, loss of cognitive function, weakness, and oxidative stress (SHERLALA et al., 2018).

To address the problem of toxic metal removal from aqueous media, various methods have been developed, including electrochemical processes, chemical precipitation, ion-exchange, filtration, and adsorption (CAROLIN et al., 2017). However, each of these methods has its own limitations, such as high cost in the case of electrochemical processes, the generation of sludge in chemical precipitation, limited ion removal in ion-exchange, and fouling of

membranes in filtration. Despite its requirement for a desorption process, adsorption is cost-effective, simple to operate, and offers a wide range of adsorbent options.

Activated carbon (HOANG et al., 2022), chitosan (HARIPRIYAN; GOPINATH; ARUN, 2022), iron oxide (BHATERIA; SINGH, 2019), silica (DA'NA, 2017), and graphene-based materials (KONG et al., 2021) are some of the materials that have been used as adsorbents for toxic metals. Among graphene-based materials, graphene oxide (GO) has received significant attention from the scientific community for its high potential in toxic metal adsorption (PENG et al., 2017). GO is a non-toxic, environmentally friendly, low-cost material with a large surface area containing oxygenated groups that makes it an ideal material for the removal of toxic metals from aqueous solutions (KAUR; KAUR; SINGH, 2019; KUMAR et al., 2019; PENG et al., 2017). However, due to its strong adsorption affinity for toxic metals, it exhibits low selectivity, making it difficult to adsorb a specific target ion (GU; FEIN, 2015; SITKO et al., 2013).

Efforts have been made to improve the selectivity of GO, such as by incorporating nitrogen-containing functional groups (SITKO et al., 2014) or mercapto groups (ZIAEI; MEHDINIA; JABBARI, 2014). More recently, the use of an ion-imprinted polymer has been explored as a means of improving selectivity (CHI et al., 2021). However, these strategies have focused more on improving the adsorption capacity rather than selectivity. Another limitation of GO is its difficulty in being removed from aqueous solutions, which restricts its reuse. To overcome this, researchers have synthesized GO composites containing magnetic nanoparticles, which can be removed from solution using an external magnetic field (DAHAGHIN; MOUSAVI; SAJJADI, 2017; DUBEY et al., 2022; KAUR; KAUR; SINGH, 2019; LIU et al., 2015a; SUMAN et al., 2022). An alternative approach is the covalent bonding of GO to different supports, such as polystyrene (ISLAM et al., 2014), amberlite resin (KUMAR et al., 2019), or cellulose (CHEN et al., 2022; SITKO et al., 2016). These efforts aim to enhance the functionality of GO and broaden its range of applications in adsorptive processes.

This work aims to investigate the use of a composite of GO and magnetite functionalized with 3-aminopropyltriethoxysilane to improve the selectivity towards hexavalent chromium in a multielement solution containing Cd(II), Cu(II), and Cr(VI). The modified and unmodified composites were characterized using various physico-chemical techniques, and batch adsorption experiments were carried out to investigate the effect of GO content and amino group grafting on Cr(VI) selectivity. The mechanism of adsorption was studied using thermodynamic, isotherm, and kinetic models, and the reusability of the material was also

evaluated. Our results demonstrate that the MAG-GO-NH_2 composite has potential as a selective adsorbent for Cr(VI).

2.2 Experimental procedure

2.2.1 Chemicals and solutions

All the chemicals utilized were of analytical grade and were used as recieved without further purification. Potassium permanganate ($KMnO_4$, 90%, Dinamica), sulfuric acid (H_2SO_4, 95-99%, Vetec), graphite (98%, Synth), hydrogen peroxide (H_2O_2 30% v/v, Synth), hydrochloric acid (HCl, Synth), nictric acid (HNO_3, Synth), and (3-aminopropyl)triethoxysilane (APTES, 95%, Sigma Aldrich). Stock solutions of single and multielement ions (Cu(II), Cd(II), and Cr(VI), 10 mmol L^{-1}) were prepared in a buffer solution of acetic acid (HAc)/sodium acetate (Ac^-) at pH 4.9. Copper nitrate, ($Cu(NO_3)_2 \cdot 3H_2O$, 99%, Vetec), cadmium nitrate ($Cd(NO_3)_2.4H_2O$, 99%, Vetec), and potassium dicromate ($K_2Cr_2O_7$, 99.9%, Merck) were used as metal precursors.

2.2.2 Materials synthesis

2.2.2.1 Graphene oxide

The synthesis of graphene oxide (GO) was performed through a modified version of the Hummers method (HUMMERS; OFFEMAN, 1958). The process involved mixing 0.500 g of graphite and 12 mL of concentrated H_2SO_4 in a round bottom flask, which was cooled to below 20 °C using an ice bath. Next, 1.500 g of $KMnO_4$ was slowly added to the mixture and stirred overnight at room temperature. To stop the reaction, the mixture was diluted with milli-Q water in two portions of 25 mL, separated by a one-hour interval. Afterwards, 2 mL of H_2O_2 (30% v/v) was used to neutralize the remaining manganese ions. The resulting bright yellow suspension was purified by washing with a 1:10 solution of HCl and milli-Q water. Finally, the graphitic oxide was sonicated to obtain a dispersion of GO in water.

2.2.2.2 Composites of magnetite and graphene oxide

The synthesis of composites of magnetite and graphene oxide was carried out using the co-precipitation method (FREIRE et al., 2016). For this purpose, 1.080 g of $FeCl_3 \cdot 6H_2O$ and 0.732 g of $FeSO_4 \cdot 7H_2O$ (in a molar ratio of 2 Fe(III) :1 Fe(II)) were solubilized in 10 mL of milli-Q water (with HCl 1 mol L^{-1}) and added to a round bottom flask containing 100 mL of dispersion of GO (1.0, 2.0 or 3.0 mg mL^{-1}) in the temperature range of 65 – 70 °C. Then, 4 mL of NH_4OH were added dropwise and the mixture was kept under vigorous mechanical stirring for 60 min. After cooling the material to room temperature, it was washed with milli-Q water until pH 5.0, dried in a vacuum desiccator, and ground with a mortar to obtain MAG-GO_x (x = 1, 2, or 3) samples, where x represents the concentration of the GO solution used in the synthesis of the composite. The same procedure was used to synthesize pure magnetite, however, 100 mL of milli-Q water was used instead of a GO dispersion.

2.2.2.3 Functionalized composites of magnetite and graphene oxide

The synthesis procedure of functionalized MAG-GO_1 with amino groups was carried out using APTES. First, 400 mg of the composite was dispersed in 60 mL of ethanol in a round bottom flask and stirred vigorously at a temperature range of 60 – 65 °C. Then, 1 mL of APTES dissolved in 20 mL of ethanol was added dropwise to the suspension. The reaction was allowed to proceed for 24 h before the sample was cooled to room temperature. To remove any excess of the silylating agent, the material was successively washed with water and ethanol. The supernatant solutions were analyzed by UV-Vis spectrometry (Varian, Cary 1E model). The resulting material was named MAG-GO_1-NH_2. The synthesis procedure is illustrated in Fig. 10.

Figure 10 – Scheme of GO, MAG-GO_x and MAG-GO_1-NH_2 syntheses.

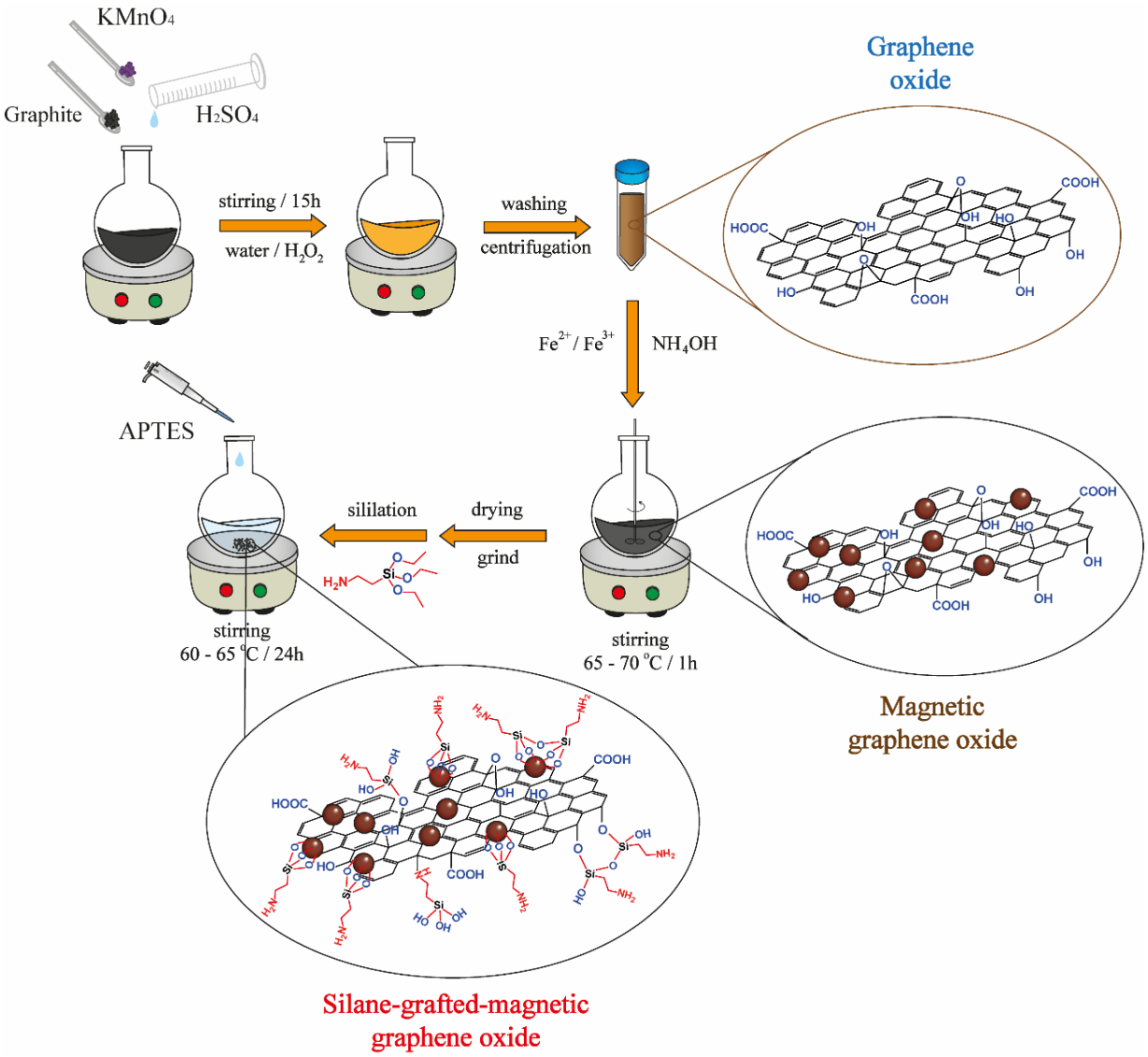

Source: the author.

2.2.3 Materials characterization

X-ray diffraction (XRD) analyses were performed on a Rigaku-DMAXB diffractometer, at room temperature, using a CuKα irradiation source of λ = 1.5405 Å, with step increments of 0.5° min^{-1}, and a 2θ angular range from 10 to 90°. Fourier transform-infrared (FTIR) spectroscopy was carried out using an IRTrace-100 (Shimadzu) instrument in a wavelength range of 4000 to 400 cm^{-1}, with resolution of 4 cm^{-1}, using samples dispersed in KBr. Thermogravimetric analyses were conducted using a Thermogravimeter Analyzer (TA

Instruments Q50) under a synthetic air flow of 60 mL min^{-1}, with a heating rate of 10 °C min^{-1} from room temperature to 850 °C. The morphology and surface aspects of the samples were evaluated using scanning electron microscopy (SEM) with energy-dispersive X-ray spectroscopy (EDS) on a Quanta 450 FEG – FEI. Zeta potential analyses were carried out using a Zetasizer Nano ZS, with 5 mg of the material dispersed in 30 mL of HAc/Ac^- buffer solution (pH 4.9 ± 0.1). Mössbauer spectra were collected using a $^{57}Co(Rh)$ radioactive source in standard transmission geometry at room temperature, and the data was evaluated using least square fitting with the software package Normos. The isomer shifts (δ) were reported relative to α-Fe. Raman scattering spectra were obtained using a T64000 Jobin–Yvon spectrometer and an Argon ion laser (514 nm) as the excitation source. All measurements were performed using a long working distance plan-achromatic objective with a 50.000.3520.50 mm lens. X-ray photoelectron spectroscopy (XPS) analyses were performed using a ThermoFisher Scientific K-alpha+ spectrometer, with a monochromatic Al Kα excitation and a spot size of 400 µm, at a pressure of 10^{-7} Pa in the analysis chamber, and pass energy of 50 eV for high resolution spectra.

2.2.4 Adsorption experiments

Typical batch experiments were conducted using 25 mg of the adsorbent suspended in 10 mL metal ion solutions prepared in HAc/Ac^- buffer (pH 4.9 ± 0.1) in Falcon tubes. Multielement solutions and single element solutions contained 0.1 mmol L^{-1} of each specie (Cd(II), Cu(II), and/or Cr(VI)). The experiments were performed at 25 ℃ using a Dubinoff water shaker. Initially, the effect of GO content on metal ion adsorption was evaluated for both single and multielement solutions in experiments of 60 min. After this period, the materials were magnetically separated, and the solutions were filtered through microfilters (0.45µ PTFE membrane) to determine the ion metal concentration using flame atomic absorption spectroscopy (FAAS) on a Varian SpectrAA 220FS model. Further studies were performed using MAG-GO_1 and MAG-GO_1-NH_2. The adsorption kinetics were studied over a time interval of 0 to 120 min, and the experimental data were fit to the pseudo-first order (S., 1907) (Equation 5) and pseudo-second order (HO; MCKAY, 1999) (Equation 6) models.

$$\ln(q_e - q_t) = \ln q_e - k_1 t \qquad (5)$$

$$\frac{t}{q_t} = \frac{1}{k_2 q_e^2} + \frac{t}{q_e} \quad (6)$$

where q_e (mmol g^{-1}) and q_t (mmol g^{-1}) are the adsorption capacity at equilibrium and time t (min), respectively; k_1 (min^{-1}) and k_2 (g $mmol^{-1}$ min^{-1}) are the pseudo-first-order and pseudo-second-order rate constants, respectively.

Adsorption isotherms were obtained using metal ion concentrations ranging from 0.02 to 2.0 mmol L^{-1}. The experimental data were fit to the Langmuir (LANGMUIR, 1918) (Equation 7) and Freundlich (FREUNDLICH, 1907) (Equation 8) models.

$$q_e = \frac{q_{max} K_L C_e}{1 + K_L C_e} \quad (7)$$

where q_e (mmol g^{-1}) is the adsorption capacity at equilibrium, q_{max} is the maximum adsorption capacity considering the complete monolayer coverage, C_e (mmol L^{-1}) is the ion concentration at equilibrium, and K_L is the constant related to the free energy of adsorption.

$$q_e = K_F + C_e^{1/n} \quad (8)$$

where q_e (mmol g^{-1}) is the adsorption capacity at equilibrium, K_F is the constant related to the adsorption capacity and n is the constant related to the adsorption intensity.

The separation factor (R_L) was calculated as an indicator whether the adsorption process is favorable ($0 < R_L < 1$), linear ($R_L = 1$), unfavorable ($R_L > 1$) or irreversible ($R_L = 0$) according to Equation 9:

$$R_L = \frac{1}{1 + K_L C_0} \quad (9)$$

where K_L is obtained from the Langmuir model (Equation 7) and C_0 is the initial concentration of the adsorbate.

Thermodynamic parameters ΔH (kJ mol^{-1}), ΔS (J mol^{-1} K^{-1}), and ΔG (kJ mol^{-1}) were calculated as described in Equations 10 and 11:

$$lnK = \frac{\Delta S}{R} - \frac{\Delta H}{RT} \quad (10)$$

$$\Delta G = \Delta H - T\Delta S \quad (11)$$

The ion desorption capacity of 0.10 mol L^{-1} HCl and NaOH solutions was evaluated using 25 mg of the sample loaded with ions and 10 mL of the desorption solution. After shaking in a Dubinoff bath for 10 min, the sample was magnetically separated, the

supernatant was filtered, and the leached ions were quantified. The desorption capacity was evaluated for each solution using a freshly loaded sample. Reuse assays were performed using multielement solutions containing 0.1 mmol L^{-1} of each analyte (Cd(II), Cu(II), and Cr(VI)). After each cycle, the material was washed in the following order: 0.1 mmol L^{-1} HCl, water, 0.1 mmol L^{-1} NaOH, and finally with water (three times). The sample was then dried in a vacuum desiccator. For each 25 mg of loaded sample used, 10 mL of desorption solution or water was used.

2.3 Results and discussion

2.3.1 Structural characterization

The XRD patterns of magnetite, GO, and MAG-GO_x composites are presented in Fig. 11a. GO exhibited broad peaks centered at 17.7 an 27.4°, which can be related to the presence of oxygenated groups such as hydroxyl, carboxyl, carbonyl, and epoxy, on the graphite surface after the oxidation process. This leads to a weakening of π–π interlayer interaction, which increases the interlayer spacing of graphite sheets and results in what is known as graphitic oxide (DIMIEV et al., 2012). The synthesized magnetite exhibited diffraction peaks at 18.2, 30.1, 35.5, 43.2, 53.5, 57.2, 62.7, 71.1, and 74.3°, indexed to (111), (220), (311), (400), (422), (511), (440), (620), and (533) planes, which are typical of a Fe_3O_4 inverse spinel cubic structure (ICSD, reference code 01-086-1340). MAG-GO_x composites showed an increase in background noise, with a consequent broadening and disappearance of some peaks related to magnetite (mainly the peak indexed to (311)) with an increase in GO content. This effect may be attributed to the reduction in magnetite particle size of (nucleation of nanoparticles in distinct regions of GO) or an increase in the amorphous portion.

Figure 11 – (a) XRD patterns and (b) TG curves of GO, Fe_3O_4, and MAG-GO_x materials; (c) magnetic separation of MAG-GO_1, MAG-GO_2 and MAG-GO_3 from aqueous solution.

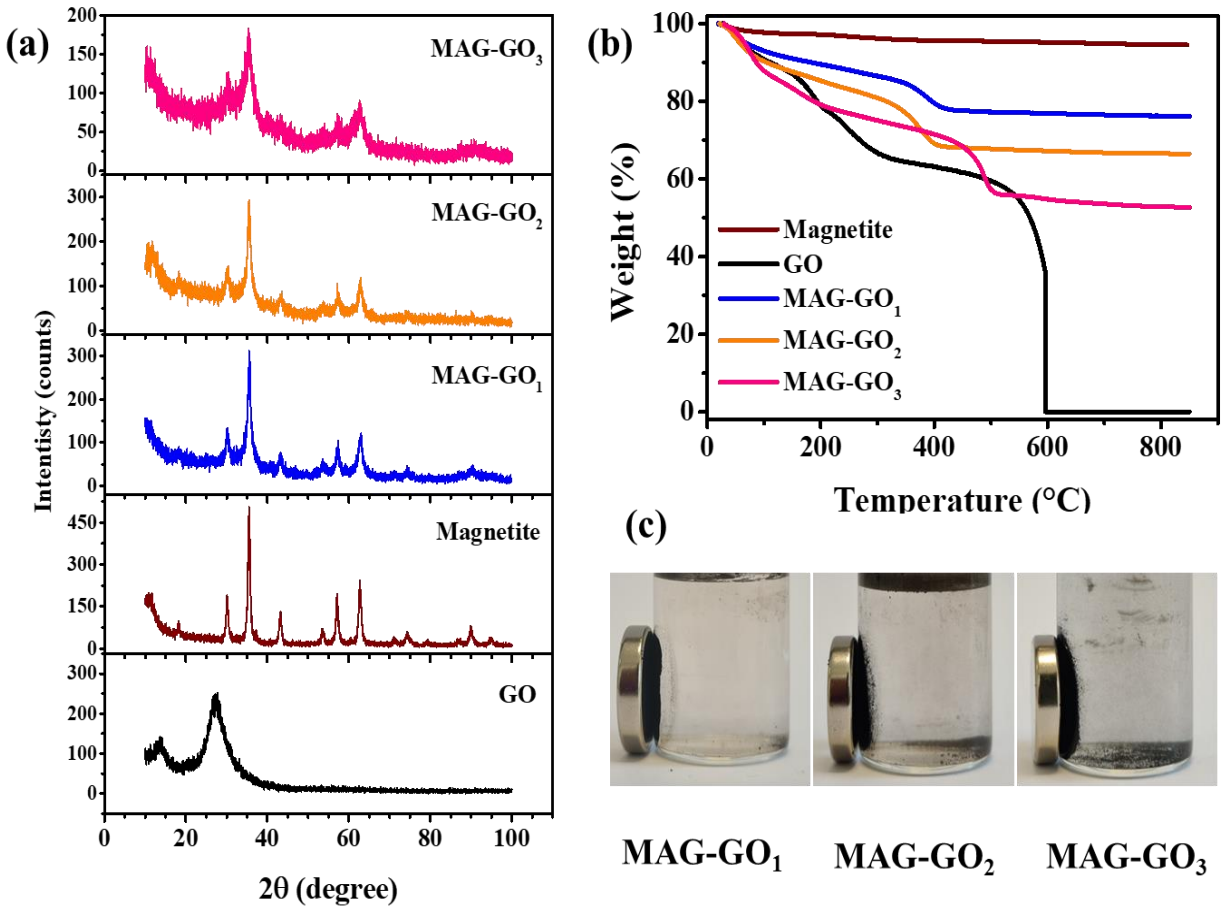

Source: the author.

Thermogravimetric analyses (TGA) were used to confirm the formation of the composites and to quantify the relative amount of magnetite and graphene oxide as depicted in Fig. 11b. The TGA of pure GO exhibited three significant mass loss events in the temperature range of 25 – 850 °C: (i) loss of physisorbed water from 25 to 200 °C (21.2%), (ii) partial decomposition of oxygen functionalities and carbon oxidation into CO and CO_2 from 200 to 500 °C (19.2%) (ISLAM et al., 2014), and (iii) complete disruption of the carbon basal planes of the GO structure from 530 to 630 °C (59.6%). Similar events were observed for MAG-GO samples; however, the GO present in the composites was eliminated at lower temperatures (385, 372, and 484 °C for MAG-GO_1, MAG-GO_2, and MAG-GO_3, respectively) due to the presence of magnetite, which may have a catalytic effect on carbon oxidation (JIA; LI, 2014; JIANG; LIU; MA, 2019). Moreover, the magnetite sample showed a total loss of 5.5 wt.% due to the removal of free and physically adsorbed water. Consequently, the residual mass in the

composites represents the percentage of Fe_3O_4 and the total weight loss, discounting physisorbed water, represents the percentage of GO. The content of GO in the samples was 13.4, 18.9, and 26.3 wt.% for MAG-GO_1, MAG-GO_2, and MAG-GO_3, respectively.

Figure 12 – Scanning electron microscopy images for (a) GO, (b) Fe_3O_4, (c) MAG-GO_1, (d) MAG-GO_2, and (e) MAG-GO_3.

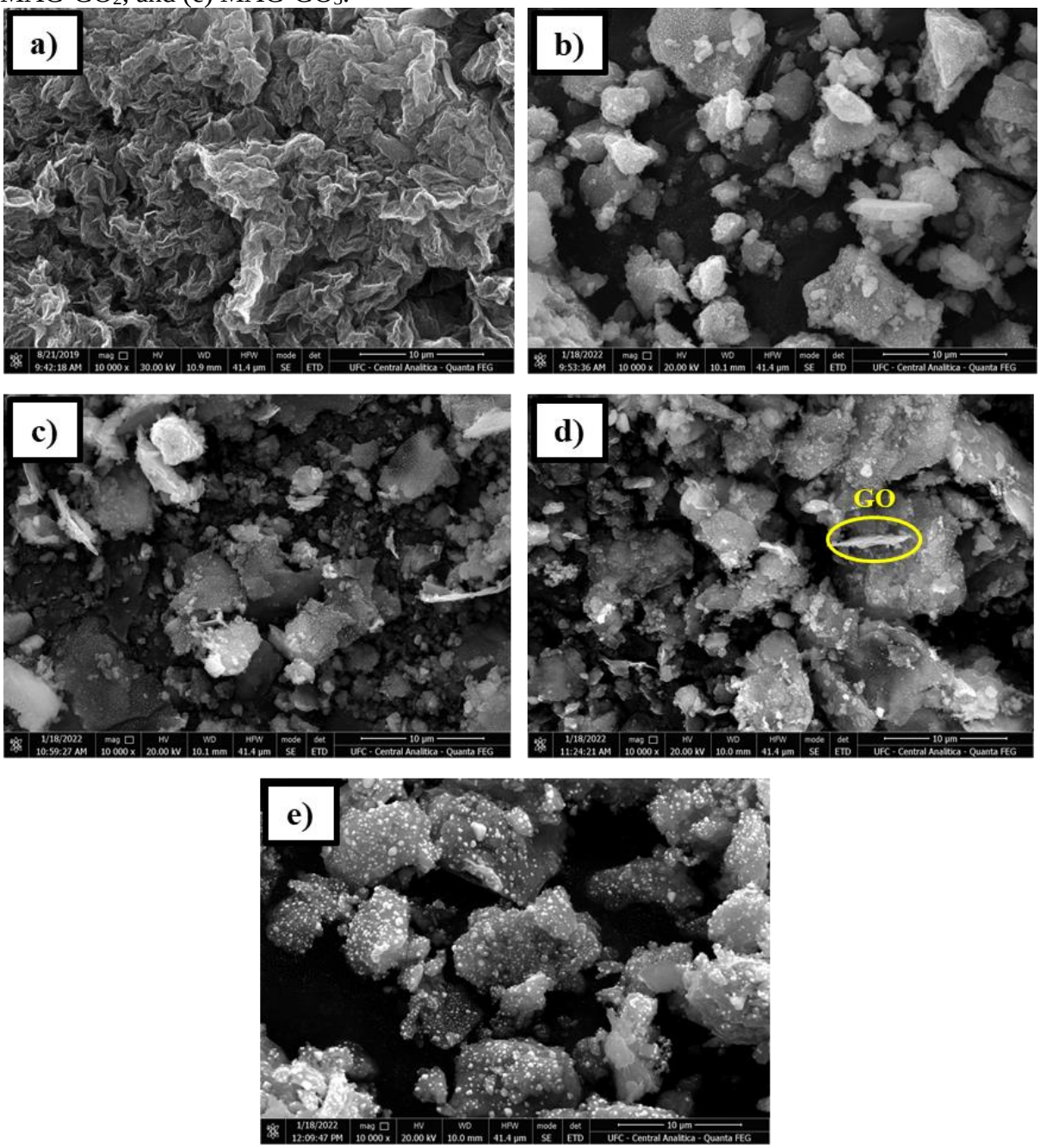

Source: the author.

SEM images (Fig. 12) were used to assess the morphological properties of GO, magnetite, and MAG-GO_x composites. Fig. 12a depicts that GO displays a crinkled surface with clusters that are flattened across the entire surface area. In turn, magnetite is composed of different-sized agglomerates (Fig. 12b), some of which appear to consist of flat layers. The MAG-GO_x composites (Figs. 12c, 12d and 12e) are shown to have agglomerates of irregular form and shape, which can be attributed to Fe_3O_4 particles attached to small GO sheets. Additionally, larger GO sheets are dispersed throughout the samples (highlighted in Fig. 12d). As the GO content increases, the clusters on the surface of the agglomerates become larger and less dispersed, as demonstrated in Fig. A1. EDS mapping (illustrated in Fig. A2) provides further evidence for the presence of both magnetite and graphene oxide in the composites, and supports the results of the TGA analysis, which showed that the weight percentage of iron is exceeds that of carbon.

FTIR spectra of the synthesized samples are displayed in Fig. 13a. A broad band present in all materials in the range of 3400 to 3000 cm^{-1} is assigned to the O−H stretching vibrations. The spectrum of GO indicates the presence of various oxygenated functional groups on its structure. The absorptions at 1720 cm^{-1} and 1568 cm^{-1} can be assigned to C=O (carbonyl/carboxyl) groups and C=C bonds (aromatic rings), respectively, while the vibrations observed at 1176 cm^{-1} and 1070 cm^{-1} correspond to C−O stretching (GUO et al., 2016; LIU et al., 2019; SITKO et al., 2013). The presence of magnetite in the composites is confirmed by the typical absorption at 584 cm^{-1} corresponding to Fe−O stretching in the octahedral and tetrahedral sites of Fe_3O_4 (FREIRE et al., 2016). Also, a shoulder at 629 cm^{-1} and a small peak around 430 cm^{-1} suggest the presence of maghemite (γ-Fe_2O_3), an oxidized form of magnetite (STOIA; ISTRATIE; PA, 2016). The weak band at 1620 cm^{-1} is assigned to the O−H bending mode of H_2O molecules adsorbed on the surface of the materials. Moreover, MAG-GO_x samples exhibit a broad band in the range of 1290 to 860 cm^{-1}, centered at 1196 cm^{-1}, which may correspond to different overlapping absorptions, including C=C and C−O vibrations.

Figure 13 – (a) FTIR spectra of GO, magnetite, MAG-GO_x materials, and MAG-GO_1-NH_2 composite; (b) Mössbauer spectra of GO, MAG-GO_1, and MAG-GO_1-NH_2.

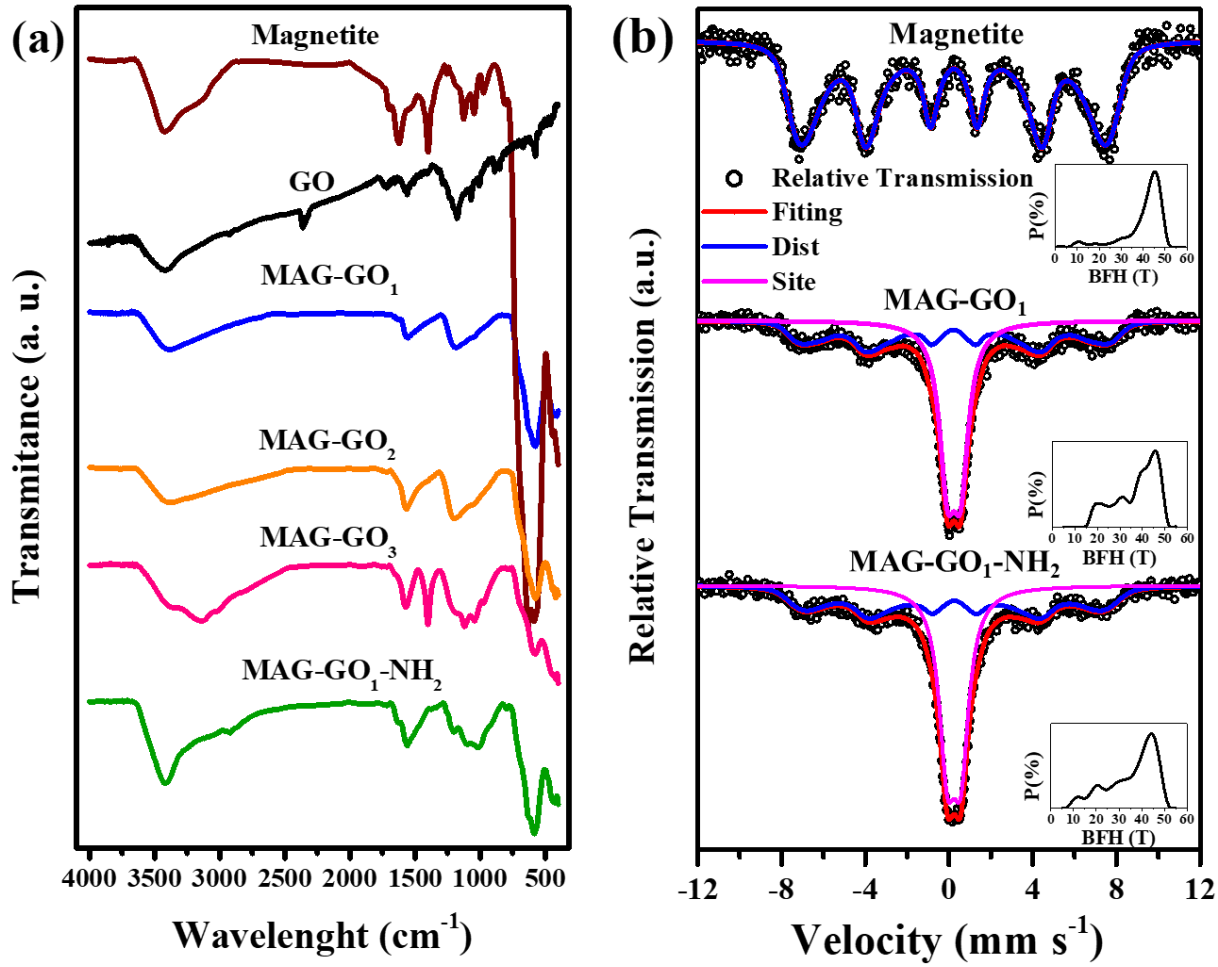

Source: the author.

The success of the MAG-GO_1 grafting can be confirmed by the appearance of bands in the FTIR spectrum of the MAG-GO_1-NH_2 composite (Fig. 13a) that correspond to functional groups of APTES. The higher intensity and narrowing of the broad band centered at 3420 cm^{-1} can be associated to N−H stretching, while N–H deformation is suggested by the increased intensity of the absorption band at 1626 cm^{-1}. These bands provide evidence of the presence of free amine, therefore suitable for metal adsorption. Furthermore, the weak band at 2920 cm^{-1} is assigned to the C–H stretching of $–CH_2$ in aliphatic groups present in the structure of APTES. The effectiveness of silanization is further demonstrated by the appearance of absorptions at 1100 cm^{-1}, 1014 cm^{-1}, and 798 cm^{-1} corresponding to Si–O–C, Si–O–Si, and Si–O vibrations, respectively. Although the formation of Fe–O–Si bonds is expected to be observed at 589 cm^{-1},

this stretching may overlap with the strong Fe−O vibration (KARADE et al., 2021; LEE; KIM, 2020).

It should be noted that both magnetite and GO may undergo silanization during the grafting procedure. In the case of GO, the reaction with APTES can occur via two major mechanisms: (i) the displacement of alkoxy groups on APTES by hydroxyl groups on GO, forming Si–O–C bond (as confirmed by the FTIR spectra in Fig. 13a), and (ii) the attack of amine on the epoxy rings, leading to the formation of a hydroxyl group (LEE; KIM, 2020). Meanwhile, magnetite and APTES can react via mecanism (i), which involves the attack of hydroxyls present in Fe_3O_4 and the formation of Fe–O–Si bonds.

Mössbauer spectra of Fe_3O_4, MAG-GO_1, and MAG-GO_1-NH_2 at room temperature are shown in Fig. 13b, and the hyperfine parameters obtained from the fits of the experimental data are reported in Table 1. The Mössbauer spectrum of Fe_3O_4 exhibits a characteristic ferromagnetic sextet that was fit using the magnetic hyperfine field distribution model (blue line). This result is expected for Fe_3O_4, as the Mössbauer spectrum shows the presence of Fe^{3+} in tetrahedral sites and Fe^{3+}/Fe^{2+} in octahedral ones. However, MAG-GO_1 and MAG-GO_1-NH_2 also show paramagnetic doublets (pink line) in addition to the ferromagnetic sextet (blue line).

The presence of doublets in Mössbauer spectra suggests that the Fe_3O_4 particles nucleated and grew independently of each other on the surface of GO sheets (AHLAWAT et al., 2011; KOLEN'KO et al., 2014; ZÉLIS et al., 2013). This may be a result of the coordination between Fe^{2+}/Fe^{3+} ions and oxygenated groups on the GO surface prior to the formation of magnetic particles (NETO et al., 2017). The reduced particle size and increased interparticle separation leads to a decrease in dipolar interactions between magnetic particles (FLEUTOT et al., 2013; PAULY et al., 2012), as indicated by the greater calculated area of the doublet (~54%) compared to the sextet (~46%). Furthermore, values of isomer shift (δ) ranging from 0.335 to 0.353 mm s^{-1} suggest that the magnetic particles are composed of partially oxidized (likely due to synthesis and air exposure) and nonstoichiometric Fe_3O_4, which is consistent with the presence of γ-Fe_2O_3 ($\delta = 0.32$ mm s^{-1}) (NETO et al., 2017) as indicated by FTIR analysis.

Table 1 – Mössbauer parameters of Fe_3O_4, MAG-GO_1 and MAG-GO_1-NH_2 samples obtained from hyperfine fits.

Sample	**Mössbauer parameters**				
	Fitting	B_{HT} (T)	δ (mm s^{-1})	Δ (mm s^{-1})	A (%)
Magnetite	Sextet (blue)	45	0.335	–0.015	100
MAG-GO_1	Sextet (blue)	46	0.350	–0.046	46.34
	Doublet (pink)	–	0.344	0.635	53.66
MAG-GO_1-NH_2	Sextet (blue)	44	0.342	–0.048	46.94
	Doublet (pink)	–	0.353	–0.646	53.06

Source: the author.

Raman spectroscopy provides important insights into the structural characteristics of carbon-based materials. The intensity ratio of the bands located at 1350 cm^{-1} (D-band) and 1580 cm^{-1} (G-band), i.e., I_D/I_G, is a measure of the sp^3/sp^2 carbon ratio in the material. Therefore, a higher I_D/I_G ratio indicates a higher number of $sp^2 \rightarrow sp^3$ transformations. Regarding graphene oxide, this implies an increase in the number of carbon atoms from the aromatic arrangement that are bonded to oxygen functionalities.

Therefore, the increase in I_D/I_G ratio ($I_D/I_G = 2.00$) observed in the MAG-GO_1 sample (as depicted from Fig. 14) compared to pure GO ($I_D/I_G = 1.02$) suggests that the GO is attached to the magnetic particles through carbon atoms rather than oxygen atoms. Conversely, the decrease in the I_D/I_G value of MAG-GO_1-NH_2 ($I_D/I_G = 1.51$) compared to MAG-GO_1 can be attributed to the bonding of APTES to magnetite and oxygenated groups of GO, which limits the freedom of sp^3 carbons and, consequently, the relative intensity of the D-band (TAYYEBI et al., 2015). The presence of Si–O–C and Fe–O–Si bonds in the FTIR spectrum of MAG-GO_1-NH_2 (Fig. 13a) supports this hypothesis.

Figure 14 – Raman spectra of GO, MAG-GO_1, and MAG-GO_1-NH_2.

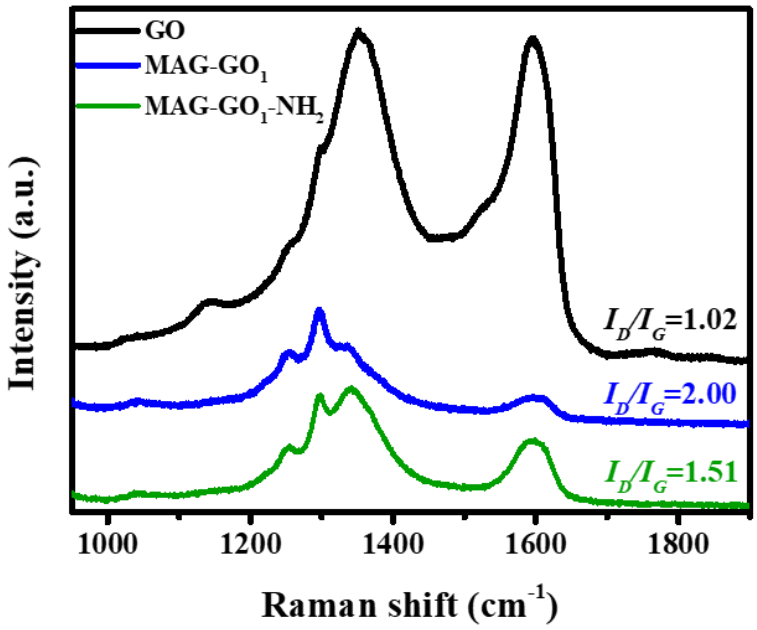

Source: the author.

XPS analyses were carried out to provide further information about the elemental composition and oxidation state of the atoms present in the samples. The survey spectra of MAG-GO_1 and MAG-GO_1-NH_2, as shown in Fig. A3, reveal the presence of C (~ 285 eV), O (~ 531 eV), and Fe (~ 711 eV), confirming the incorporation of magnetite into GO. Additionally, the presence of N1s (~ 400 eV) and Si2p (~ 101 eV) peaks in the amino-grafted material confirms the surface silanization process. High resolution spectra were acquired for C1s, O1s, Fe2p, and N1s (Fig. 15) and Table A1 summarizes the obtained data.

The C1s spectra (Figs 2.6a and 2.6d) can be deconvoluted into five peaks assigned to C–C/C=C (~284 eV), C–O (and C–N in MAG-GO_1-NH_2 samples) (284–285 eV), C–O–C (~285 eV), C=O (~286 eV), and O–C=O (~287 eV) (AL-GAASHANI et al., 2019; CHEN; WANG; FANG, 2020). The XPS profiles of O1s electrons (Figs 2.6b and 2.6e) show peaks around 529, 530, 531, and 532 eV that can be associated to O–C=O, Fe–O, C–OH, and C–O/Fe–OH bonds (AL-GAASHANI et al., 2019; FREIRE et al., 2020; YOO et al., 2020). The Fe2p spectra (Figs 2.6c and 2.6f) exhibit five doublets, corresponding to $Fe2p_{3/2}$ and $Fe2p_{1/2}$ core level electrons. Characteristic peaks of magnetite at 710 and 724 eV can be assigned to Fe^{2+} and Fe^{3+} in octahedral sites, while the peak at 711 eV is attributed to Fe^{3+} in tetrahedral sites. Other deconvolutions are ascribed to Fe^{2+} and Fe^{3+} species as oxides and/or

oxyhydroxides (FREIRE et al., 2020; RAJAN; SHARMA; SAHU, 2020; VINODHA; SHIMA; CINDRELLA, 2019). The N1s spectrum for MAG-GO_1-NH_2 (Fig. 15g) exhibits two peaks with binding energies at 399.91 and 401.81 eV, corresponding to $–NH_2$ and $–NH_3^+$, respectively (ZHANG et al., 2018), suggesting the presence of free groups able to interact with analytes.

Figure 15 – (a,b,c) High resolution XPS spectra of MAG-GO_1; (d,e,f,g) High resolution XPS spectra of MAG-GO_1-NH_2.

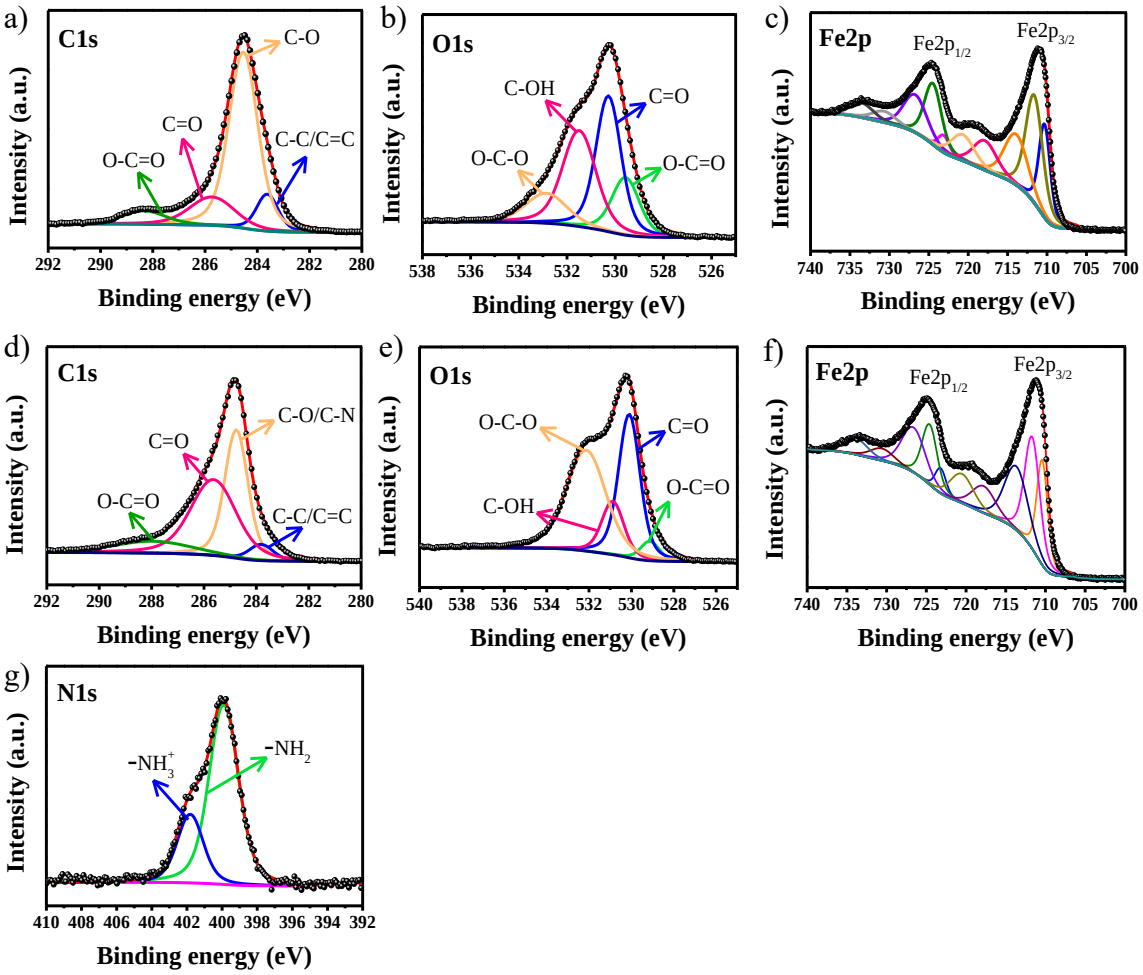

Source: the author.

2.3.2 Adsorption experiments using MAG-GO_x composites

Adsorptions assays were performed at pH 4.9 ± 0.1, where the predominant species for Cd are Cd^{2+} > $Cd(CH_3COO)^+$ > $Cd(CH_3COOH)_2$, for Cu are $Cu(CH_3COO)^+$ > Cu^{2+} > $Cu(CH_3COOH)_2$, and for Cr are $HCrO_4^-$ >> $Cr_2O_7^{2-}$ > CrO_4^- (Fig. A4). For the purpose of

simplification, the species of Cu, Cd and Cr will be referred to as Cu(II), Cd(II), and Cr(VI), respectively.

Experiments were initially conducted in multielement solutions containing 0.1 mmol L^{-1} of ions to evaluate the effect of GO on the adsorption capacity of the materials. Fig. 16a shows that the amount of adsorbed ions increased as the GO:magnetite mass ratio increased. The MAG-GO_1, MAG-GO_2, and MAG-GO_3 samples removed 0.087, 0.099, and 0.095 mmol g^{-1} of ions, respectively, while pure GO and magnetite removed 0.085 and 0.067 mmol g^{-1}, respectively. Hence, the MAG-GO_x composites combine the adsorption capacity of both GO and magnetite, along with magnetic properties, to produce materials with higher capacity to remove toxic ions and easy removal from aqueous media. Moreover, the composites preferentially adsorb Cr(VI) over Cd(II) and Cu(II). This can be related to the higher mass percentage of Fe_3O_4 in all the materials compared to GO (76 wt.% in MAG-GO_1, 66 wt.% in MAG-GO_2, and 53 wt.% in MAG-GO_3). Zeta potential analyses reveal values of +16.8 ± 0.4 mV and –24.4 ± 1.0 mV for magnetite and GO, respectively, which explains why magnetite preferentially adsorbs negative species (Cr(VI)) and GO positive species (Cd(II) and Cu(II)), indicating an electrostatically driven adsorption process. The positive nature of magnetite is associated with the formation of $\equiv Fe(II,III)OH_2^+$ species at acidic pH (SUN et al., 1998), while the acidic nature of GO is due to the presence of carboxyl groups, incompletely hydrolyzed sulfates (as shown in EDS mapping, Fig. A2), and vinylogous acids (DIMIEV et al., 2012; DIMIEV; ALEMANY; TOUR, 2013).

Figure 16 – (a) Relative amount of adsorbed ions and total amount of adsorbed ions in multielement solutions of Cd(II), Cu(II), and Cr(VI) by GO, Fe_3O_4, and MAG-GO_x materials; (b) Percentual of ions adsorbed in multielement solutions of Cd(II), Cu(II), and Cr(VI) by GO, Fe_3O_4, and MAG-GO_x materials.

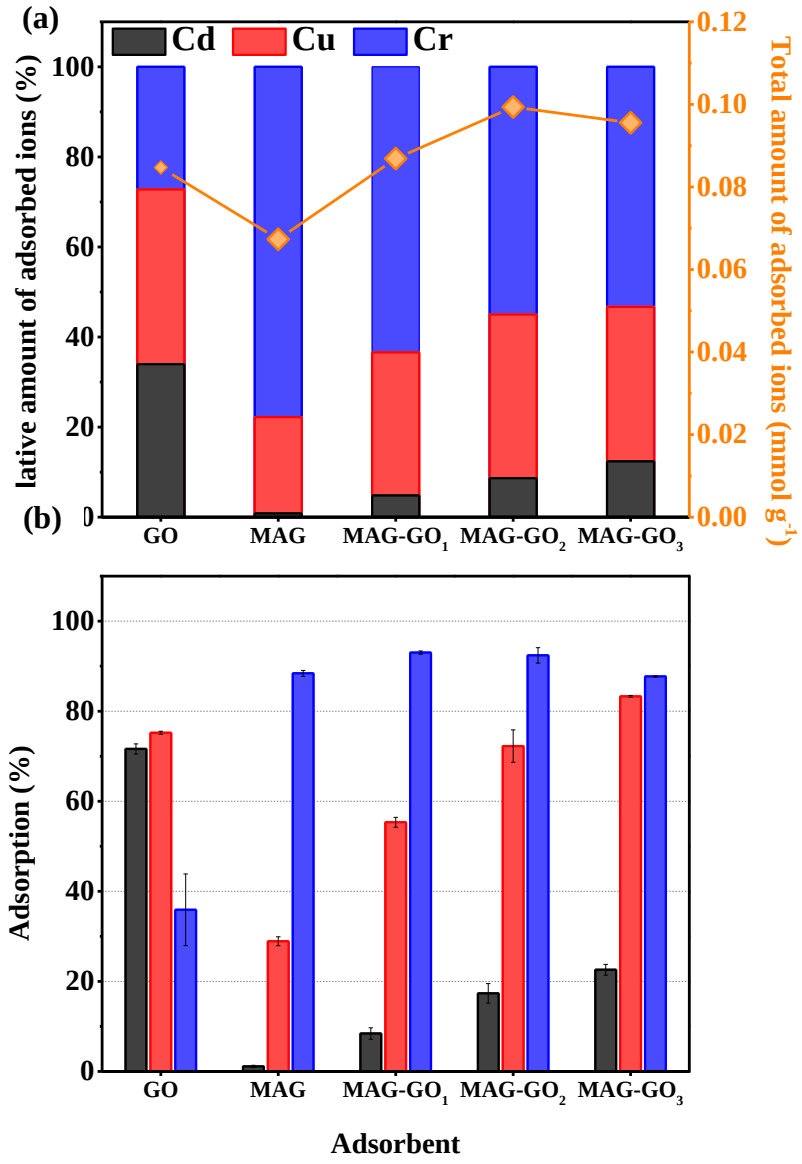

Source: the author.

Moreover, as shown in Fig. 16b, the adsorption of Cd(II) and Cu(II) increases with the GO content. MAG-GO_1 adsorbs 8.4% and 55.3% of the initial Cd(II) and Cu(II), respectively, whereas for MAG-GO_3 these percentages rise to 22.6% and 83.3%. Conversely, the adsorption of Cr(VI) decreases with the increase of GO content, falling from 93.0% (MAG-GO_1) to 87.7% (MAG-GO_3). This decline is primary attributed to the charge nature of the

adsorbents. The zeta potential values were determined as follows: MAG-GO_1 (+ 15.2 ± 0.6 mV) > MAG-GO_2 (+ 5.9 ± 0.6 mV) > MAG-GO_3 (– 7.1 ± 0.6 mV), which is consistent with the percentage of GO in the samples, indicating that there will be an improvement in the removal of positive species (i.e., $Cu(CH_3COO)^+$, Cu^{2+}, $Cd(CH_3COO)^+$, and Cd^{2+}) and a decline, although to a lesser extension, in the uptake of negative ones (i.e., $HCrO_4^-$ and $Cr_2O_7^{2-}$). This same behavior is observed when 0.1 mmol L^{-1} monoelement solutions were used (Fig. 17), where MAG-GO_1 adsorbed 17.8%, 65.8%, and 97.0% of the initial Cd(II), Cu(II), and Cr(VI), respectively, while MAG-GO_3 removed 47.8%, 95.4%, and 86.9%, respectively.

Figure 17 – Adsorption of Cd(II), Cu(II), and Cr(VI) in monoelement solutions by MAG-GO_x materials.

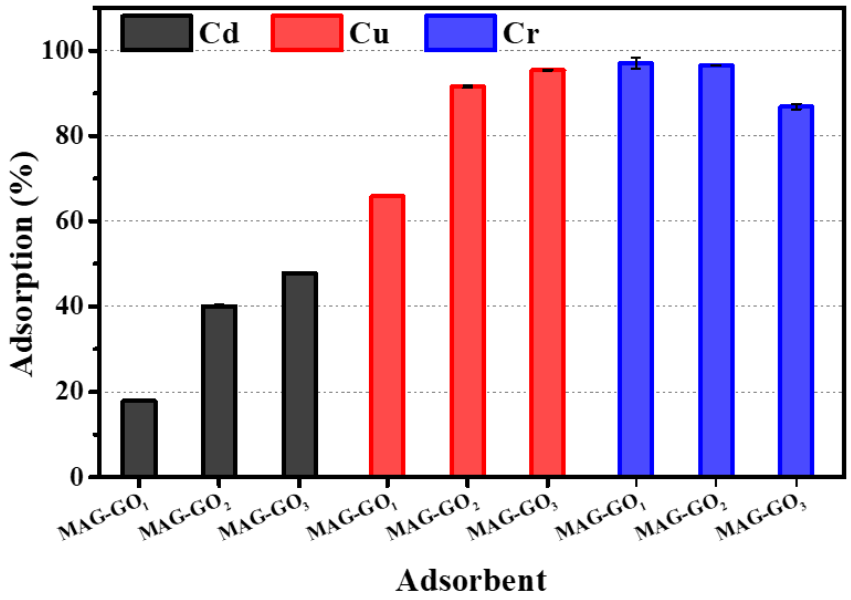

Source: the author.

When considering exclusively the total amount of ions removed, both MAG-GO_2 and MAG-GO_3 could be suitable for surface modifications to improve Cr(VI) adsorption. However, these materials exhibit low selectivity for these ions and low magnetization, implicating on the removal of the adsorbents after removing the solutes from the aqueous media. In fact, some of these composites remain in the solution after magnetic separation (Fig. 11c). Hereupon, due to its optimized features, such as higher adsorption capacity compared to Fe_3O_4 and suitable magnetization, MAG-GO_1 was selected for functionalization with amino groups to enhance Cr(VI) selectivity. At pH 4.9, the amino moieties are protonated (DOADRIO

et al., 2014) and considering that Cr(VI) is a hard acid (MIESSLER; FISCHER; TARR, [s.d.]), it is feasible to hypothesize that the amino functionalization will make the material more selective for Cr(VI) at the expense of the other metals.

2.3.3 Adsorption experiments using MAG-GO$_1$-NH$_2$ composites

2.3.3.1 Adsorption isotherms

In order to understand the adsorption mechanism of Cd(II), Cu(II), and Cr(VI) by MAG-GO$_1$ and MAG-GO$_1$-NH$_2$, Langmuir and Freundlich isotherm models were applied to the experimental adsorption data. The nonlinear plots obtained from the adsorption equations are shown in Fig. 18 and the calculated parameters are displayed in Table A2. For both samples, the Langmuir model provided a better description of the experimental results, indicating that the adsorption of each metal occurs as a homogeneous monolayer coverage in the correspondent adsorption site. Although a decrease in adsorption capacity towards Cr(VI) has been observed for MAG-GO$_1$-NH$_2$ (0.57 mmol g^{-1}) compared to MAG-GO$_1$ (0.61 mmol g^{-1}), an enhancement in Cr(VI) selectivity was obtained: MAG-GO$_1$-NH$_2$ adsorbed Cr(VI) at 39.0 and 6.5 times more than Cd(II) and Cu(II), respectively, while MAG-GO$_1$ adsorbed 5 times more Cr(VI) than Cd(II) and Cu(II). This effect is probably due to the presence of $-NH_3^+$ moieties, which enable electrostatic interactions with negative Cr(VI) species, and to the hard-hard interactions, according to the Hard and Soft Acid and Base (HSAB) theory, between $HCrO_4^-$ (the main specie at pH 4.9) and the $-NH_3^+$ groups.

Figure 18 – Adsorption isotherms of Cd(II), Cu(II), and Cr(VI) using (a) MAG-GO_1 and (b) MAG-GO_1-NH_2 composites at 298 K. Symbols represent the experimental data, solid lines represent Freundlich model, and dashed lines represent Langmuir model.

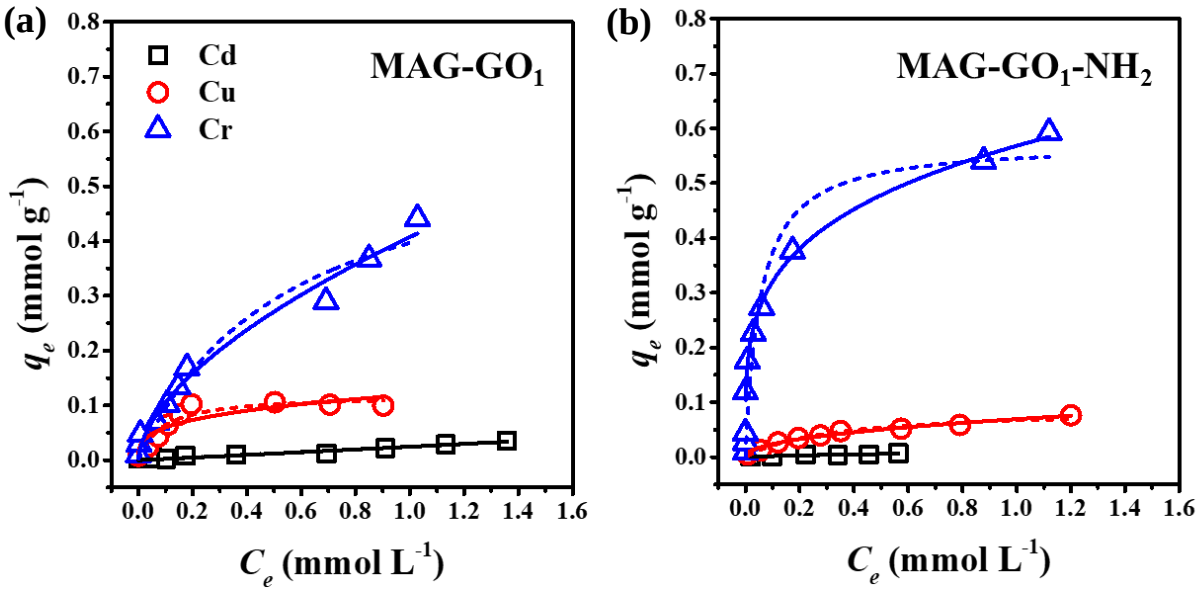

Source: the author.

The thermodynamic parameters for the adsorption of Cd(II), Cu(II), and Cr(VI) onto MAG-GO_1-NH_2 were determined using Van't Hoff plot analysis (Fig. A5) based on the adsorption isotherms data obtained at 298, 308, and 318 K (Fig. 19, Table A3 summarizes the data). The calculated values of entropy, enthalpy, and Gibbs free energy are presented in Table 2. The results indicated that the adsorption of Cu(II) and Cr(VI) onto MAG-GO_1-NH_2 is spontaneous, as reflected by ΔG negative values, while the adsorption of Cd(II) is non-spontaneous, with positive ΔG values. Moreover, as the temperature increases, ΔG decreases for the three toxic metals. The ΔH values show that the adsorption is endothermic, which corroborates the lower values of ΔG with temperature. The positive values of ΔS suggest possible structural changes or rearrangements in the adsorbate-adsorbent active complex. Furthermore, the calculations of the separation factor (R_L) at the studied temperature range indicate that the adsorption of Cr(VI) and Cu(II) is favorable (R_L values ranging from 0.01 to 0.71), while the adsorption of Cd(II) is unfavorable (R_L values ranging from 1.01 to 5.56), agreeing with ΔG values .

Figure 19 – Adsorption isotherms of Cd(II), Cu(II), and Cr(VI) by MAG-GO$_1$-NH$_2$ obtained at 298, 308, and 318 K. Symbols represent the experimental data, solid lines represent Freundlich model, and dashed lines represent Langmuir model.

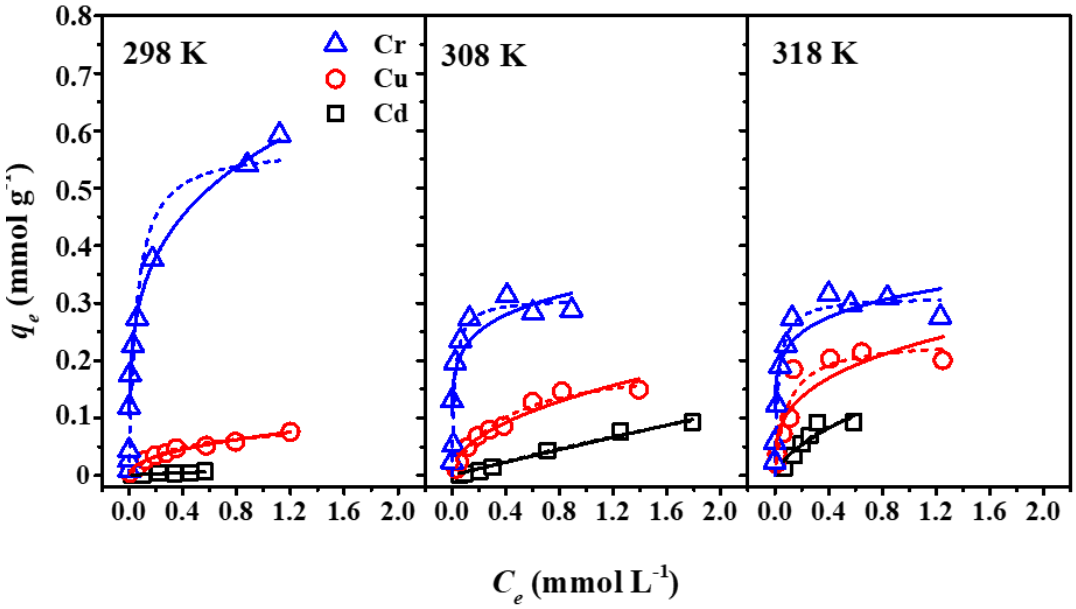

Source: the author.

Table 2 – Thermodynamic parameters of Cd(II), Cu(II), and Cr(VI) adsorption by MAG-GO$_1$-NH$_2$.

Metal	ΔS (J mol^{-1} K^{-1})	ΔH (J mol^{-1})	ΔG (J mol^{-1})		
			298 K	308 K	318 K
Cr	125.67	29770.49	- 7679.17	- 8935.87	- 10192.57
Cu	163.13	46424.25	- 2188.49	- 3819.79	- 5451.09
Cd	64.93	21061.86	1702.28	1052.96	403.63

Source: the author.

2.3.3.2 Adsorption kinetics

The adsorption kinetics of MAG-GO$_1$-NH$_2$ at different ion concentrations are displayed in Fig. 20. It was observed that the adsorption equilibrium was reached within 20 min for a 0.1 mmol L^{-1} solution, 30 min for a 0.5 mmol L^{-1} solution, and 60 min for a 1.0 mmol L^{-1} solution. A significant increase in Cr(VI) adsorption was noted presented with the increase in

ion concentration. For instance, with a multielement solution of 0.1 mmol L^{-1}, Cr(VI) removal was about 0.050 mmol g^{-1}, while for a multielement solution of 1.0 mmol L^{-1}, the adsorption increased to approximately 0.32 mmol g^{-1}, representing a 6.4-fold increase. On the other hand, the improvement in ion removal for Cu(II) and Cd(II) was estimated to be 3.3 and 4.5 times, respectively, demonstrating an improvement in an Cr(VI) selectivity as the ion concentration increases. In addition, the pseudo-first order and pseudo-second order models were employed to fit the experimental data, and the kinetic parameters are summarized in Table A4.

Figure 20 – Adsorption kinetics of Cd(II), Cu(II), and Cr(VI) by MAG-GO_1-NH_2 at different ion concentration. Symbols represent the experimental data and lines represent the theoretical values obtained from pseudo-second-order model.

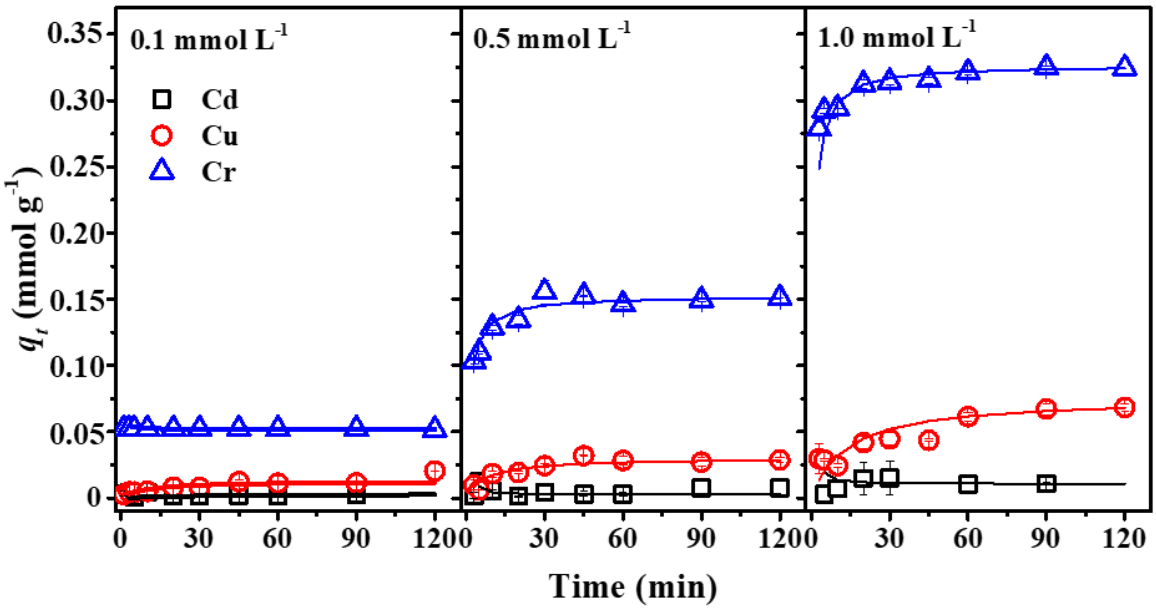

Source: the author.

The best linear fit was obtained using the pseudo-second-order model for all ions at the studied concentration range (Fig. 21). The calculated q_e values from the pseudo-second-order model were in close agreement with the experimental results, suggesting that the ion removal is mainly controlled by chemical adsorption. It is important to highlight, however, that electrostatic forces also play a role in the ion removal process, since the adsorbates are charged species and their migration from the bulk solution is likely driven by electrostatic forces (ZHANG et al., 2018).

Figure 21 – Kinetic studies at different ion concentration: (a) pseudo-first order, (b) pseudo-second order.

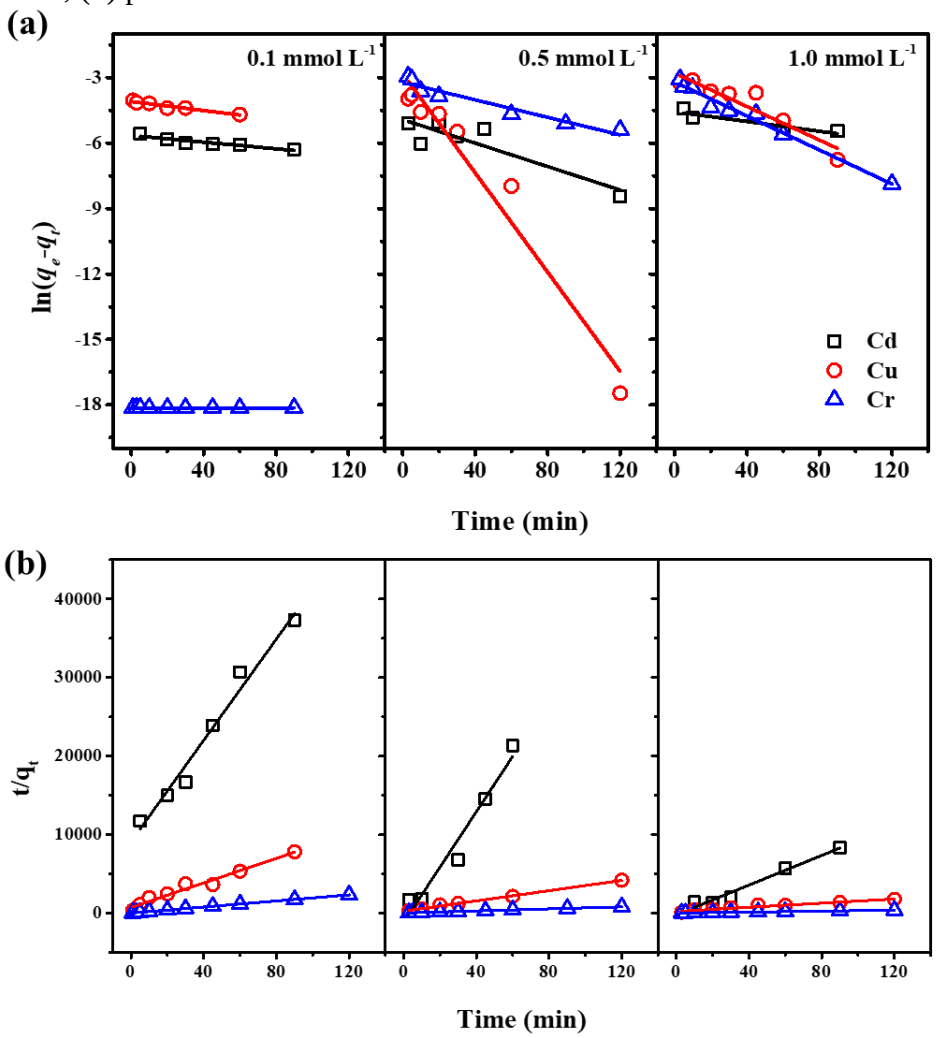

Source: the author.

The results of XPS analysis performed on MAG-GO_1-NH_2 after one and five cycles of ion adsorption/desorption are presented in Fig. 22. After one cycle of adsorption Cd, Cu, and Cr were present in the adsorbent as weak signals in the high resolution spectra, indicating a limited quantity of these species. However, after five cycles of adsorption, Cd was not detected, whereas a weaker signal for Cu was found, and a stronger signal for Cr appeared. This is likely due to the higher adsorption of Cr(VI) on MAG-GO_1-NH_2. The deconvolution of Cr2p (Fig. 22i) showed two doublets corresponding to Cr(III) (577.16 and 587.02 eV) and Cr(VI) (578.39 and 588.25 eV), suggesting that a portion of the Cr(VI) was reduced to Cr(III), probably due to the electron donation of the sp^2-hybridized carbons in GO, as well as the presence of magnetite, which enhances charge transfer through Cr(VI) adsorption (ZHANG et al., 2018).

In addition, the N1s spectrum (Fig. 22h) displayed a single peak at 400.13 eV that might be related to the presence of only $–NH_2$, suggesting full $–NH_3^+$ neutralization with NaOH.

Figure 22 – (a,b,c,d) High resolution XPS spectra of MAG-GO_1-NH_2 after the first cycle of adsorption; (e,f,g,h,i) High resolution XPS spectra of MAG-GO_1-NH_2 after the fifth cycle of adsorption.

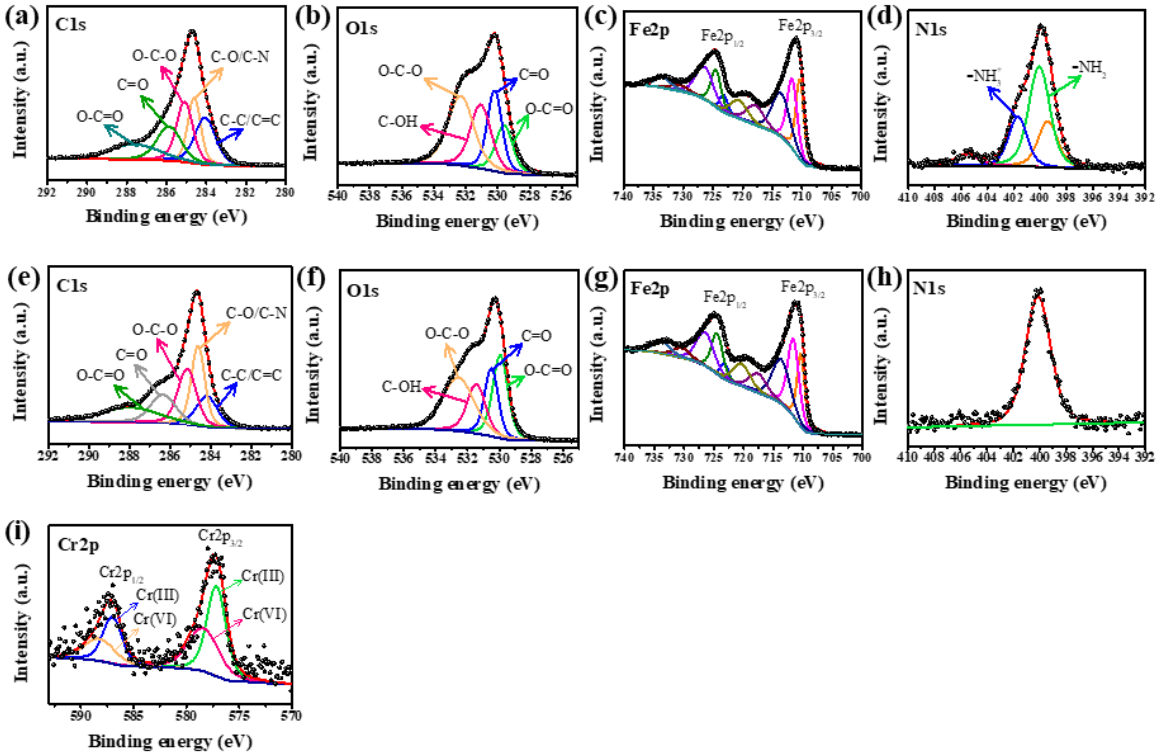

Source: the author.

Hereupon, the adsorption of the solutes by MAG-GO_1-NH_2 can be attributed to different mechanisms due to the surface groups present, including (i) binding of metals with oxygenated groups from Fe_3O_4/GO and amino groups from APTES (GUO et al., 2016; YOO et al., 2020; ZHANG et al., 2018); (ii) formation of Lewis acid-base pairs, where GO act as a Lewis base through delocalized π electron systems, while species of Cd(II) (Cd^{2+} and $Cd(CH_3COO)^+$) and Cu(II) (Cu^{2+} and $Cu(CH_3COO)_2$) act as Lewis acids; on the other hand, negative Cr(VI) species (mainly $HCrO_4^-$) can act as a Lewis base and $–NH_3^+$ as a Lewis acid (TAN et al., 2015); (iii) formation of hydrogen bonds between oxygenated/amino groups with acetate complexes of cadmium ($Cd(CH_3COO)^+$ and $Cd(CH_3COO)_2$) and copper ($Cu(CH_3COO)^+$ and $Cu(CH_3COO)_2$), and with chromium species (LIU et al., 2017a); and (iv) partial reduction of Cr(VI) to Cr(III).

2.3.4 Reuse and cyclability

Desorption experiments were performed using 0.10 mol L^{-1} solutions of HCl and NaOH. The use of HCl solution resulted in the desorption of cadmium (50.1%) and copper (85.5%) and presented a lower capacity to desorb chromium (15.8%). This is related to the ion exchange between protons and Cd(II) and Cu(II) species, and Cr(III) ions (shown by XPS analysis). A negligible amount of iron (< 0.5 wt.%) was leached due to the dissolution of magnetite. On the other hand, the use of NaOH solution resulted in the desorption of only chromium (84.6%), possibly due to the ion exchange between hydroxyl ions and Cr(VI) species and the neutralization of $–NH_3^+$ groups. Besides, the coprecipitation of cadmium and copper may occur due to the high pH (12.9) of the NaOH solution, which also prevents their detection by AAS analysis and also the leaching of iron. This allows for the separation/preconcentration of only Cr(VI).

Fig. 23 displays the reuse of MAG-GO_1-NH_2 over five adsorption/desorption cycles. It is shown that the removal of Cr(VI) remains fairly constant at 100% with a slight decrease in the 5^{th} cycle. Meanwhile, the adsorption of Cu(II) increases significantly, which can be attributed to the small amount of iron leaching, which favors the adsorption of positive species. In turn, Cd(II) adsorption remains unchanged at about 12%. The preferential adsorption of Cu(II) over Cd(II) can be associated with the electronegativity of the metals and the stability constant of $M(OH)^+$ and $M(Ac)^+$ species (SITKO et al., 2013), probably formed through complexation of M^{2+} with −COOH and −COH groups on GO. The electronegativity and the stability constants increase as $Cu^{2+} > Cd^{2+}$ (AD, 1999), which corresponds to the observed order of preferential adsorption.

Figure 23 – Experiments of reuse of MAG-GO_1-NH_2 towards Cd(II), Cu(II), and Cr(VI) adsorption.

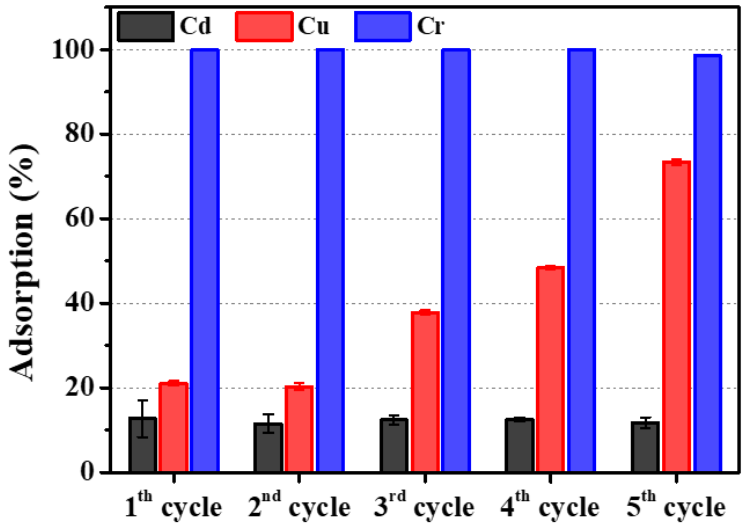

Source: the author.

2.4 Conclusion

A composite material of magnetite and graphene oxide grafted with amino groups (MAG-GO_1-NH_2) was successfully synthesized, showing promising results in the selective adsorption of chromium. Experiments in multielement solutions containing Cd(II), Cu(II), and Cr(VI) revealed that the content of GO in the composite impacts ion removal and selectivity, as a result of the surface charge of the material. The adsorption behavior of MAG-GO_1 and MAG-GO_1-NH_2 followed the Langmuir model and displayed pseudo-second order kinetics. The adsorption capacity of MAG-GO_1 towards Cr(VI) was 5 times higher than for Cd(II) and Cu(II), while for MAG-GO_1-NH_2 this value was improved to 39.0 and 6.5 times, respectively. This improvement in Cr(VI) uptake can primarily be attributed to the presence of nitrogen atoms and $-NH_3^+$ groups, which allow for easy binding of negatively charged chromium species. The thermodynamic parameters indicated that the adsorption of Cd(II), Cu(II), and Cr(VI) onto MAG-GO_1-NH_2 was a spontaneous and energetically favorable, while the adsorption of was non-spontaneous and energetically unfavorable. Over the course of five adsorption/desorption cycles, the amino grafted composite maintained preferential removal of chromium, with adsorption levels around 100%. Therefore, MAG-GO_1-NH_2 holds great potential as a platform for selective adsorption of chromium species.

3 CHAPTER III – STRATEGIES TO BOOST CAPACITIVE DEIONIZATION PERFORMANCE OF 3D ELECTRODES

Graphite Felt (GF) 3D composite electrodes are promising candidates for emerging electrochemical water treatments such as capacitive deionization (CDI). In the present work, simple strategies to improve their performance based on modifying electrode thickness, activated carbon (AC) mass loading, and its distribution over GF were explored. Electrochemical characterizations showed that by reducing electrode thickness and increasing mass loading, increments of 45% in the case of total capacitance (F) and 70% in terms of specific capacitance (F gAC^{-1}) could be achieved. CDI experiments demonstrate that values of salt adsorption capacity (*SAC*) and concentration reduction (Δc) can be improved by more than 200% when reducing GF electrode thickness from 5.0 mm to 2.0 mm. Additionally, by using the thinnest electrodes and increasing AC mass loading, values of Δc over 50% higher were reached in accordance with the electrochemical analysis. However, this achievement was obtained penalizing *SAC*, *ASAR*, productivity (*P*) and, energy consumption (*EV*) mainly due to the larger occurrence of Faradaic reactions. Moreover, microscopy images showed that the AC was not uniformly distributed over the GF structure, just on the outer surface, impairing the penetration of electrolyte inside the electrodes. Further research, focused on adjusting the synthesis conditions, enabled us to prepare electrodes with a more homogeneous dispersion of AC. These highly distributed GF composites produced a significant enhancement in terms of *ASAR* (45%) and *P* (59%). This progress on optimizing the preparation of GF composite materials by using simple strategies has paved the way for improving the electrochemical separation of ions.

3.1 Introduction

Capacitive deionization (CDI) has emerged as a promising water treatment technology attracting the attention of the scientific community (ANDERSON; CUDERO; PALMA, 2010; CHOI et al., 2019; OREN, 2008; PORADA et al., 2013; SUSS et al., 2015; WELGEMOED; SCHUTTE, 2005). In this technology, ions are removed from water via electrosorption. By means of a low potential application, the electrodes are polarized forcing

the ions to be removed and stored in the Electrical Double Layer (EDL) formed at the electrode/electrolyte interface. Since the working principle is similar to the one used by electrochemical supercapacitors, capacitive deionization is a perfect example of the Water-Energy Nexus (ANDERSON; CUDERO; PALMA, 2010). After promoting the desalination, the electrodes are short-circuited or discharged, leading to the ion desorption forming a brine. Furthermore, the energy stored during the ion removal step can be efficiently recovered in this ion desorption step in a similar way as in the discharging phase of a supercapacitor (DŁUGOŁECKI; VAN DER WAL, 2013; GARCÍA-QUISMONDO et al., 2013b; KANG et al., 2016b; OYARZUN et al., 2020).

Carbon-based materials have been extensively used as electrodes for CDI purposes (JIA; ZHANG, 2016) and energy storage devices (CHEN; PAUL; DAI, 2017). Among them, activated carbon (AC) has been widely employed in CDI studies due to its low cost, high specific surface area (SSA) and chemical stability (LADO et al., 2019b; SANTOS et al., 2018; ZORNITTA; RUOTOLO, 2018). However, the dominant presence of micropores on AC structure hinders the effective access of the electrolytes to inner pores. This issue makes ion diffusion difficult throughout the pore network (VAQUERO et al., 2012), limiting the electrode capability of salt removal. Although micropores are mainly responsible for providing high SSA and adsorption sites for deionization, the presence of larger pores is desired in order to decrease the resistance to mass transfer and to allow ion access to inner micropores. Considering this perspective, hierarchical materials containing different pore size distributions are beneficial for CDI applications, since meso and macropores facilitate ion transport throughout the electrode (DUTTA et al., 2016; OUYANG et al., 2018b; ZHAO et al., 2016; ZORNITTA et al., 2016).

Graphite felt (GF) is a macroporous material, with a 3D pore network, high mechanical stability, outstanding electric conductivity, and is widely used for energy storage and additional environmental applications (HUONG LE; BECHELANY; CRETIN, 2017). Although the use of GF is still scarce on CDI devices (WANG et al., 2019), it has been widely applied in the field of vanadium redox flow batteries (VRFB) (BANERJEE et al., 2019a, 2019b; DAVIES; TUMMINO, 2018; PARK et al., 2014; SGL GROUP - THE CARBON COMPANY, [s.d.]; WEI et al., 2016). For this purpose, improvements in the performance of VRFBs have been achieved by increasing the compression of the felt, which has resulted in a lower ohmic resistance within the cell (BANERJEE et al., 2019b; DAVIES; TUMMINO,

2018; PARK et al., 2014). Moreover, it is important to highlight the fact that the thickness of the electrode is considered to be one of the most important contributors to internal resistance in battery fashion-like cells (QU et al., 2015). Accordingly, this parameter is considered to be mainly responsible for the loss of specific capacitance and energy density (LIU et al., 2017b). In this sense, Wei et al (WEI et al., 2016) investigated the performance of GFs having different thickness, 2.5 and 6.0 mm, observing lower ohmic losses for the thinner electrodes, similarly to what was observed by increasing the compression of the felt.

In previous works, GF was successfully coated with AC for CDI application, exhibiting good stability over cycling and emerging as a promising platform for large-scale CDI (LADO et al., 2021b; WANG et al., 2019). The general scope of that research was to fabricate a GF-AC composite that is easily scalable combining both macro porosity of GF and the high surface area of AC. However, parameters such as electrode thickness or mass loading of active material were not optimized in those studies. Since these parameters are considered to be highly significant to the improvement of electrode materials for energy storage but also for CDI applications (KIM et al., 2014; LEE et al., 2018; SANTOS et al., 2018; WANG et al., 2011; ZORNITTA et al., 2016), it was decided to explore this approach further in this new study.

In this work, the effect of electrode thickness on the performance of hierarchical 3D GF-AC electrodes in CDI application was evaluated. For this purpose, GFs with 2.5, 4.6, and 6.0 mm of thickness were coated with AC and submitted to different charge/discharge currents and potentials. Also, the effect of mass loading was evaluated by using the GFs of 2.5 mm thickness and differing mass loadings of AC. Our guiding hypothesis has been that by decreasing the electrode thickness specific capacitance could be improved, resulting in better CDI performance. In addition, by increasing the mass loading of AC, one expects an increase in salt removal in absolute terms although penalizing other variables, such as the kinetics of the CDI process.

3.2 Experimental Procedure

3.2.1 Materials and Methods

3.2.1.1 Electrode preparation

The carbon slurry was prepared in a ball mill with 80% activated carbon (PICACTIF SuperCap BP10 type, PICA France, specific surface area = 2400 $m^2 g^{-1}$, hereinafter AC), 10% carbon black (acetylene, 100% compressed, > 99.9%, Alfa Aesar), 10% Polyvinylidene Fluoride (PVDF, MTI) and isopropanol as a dispersive medium. The carbon ink with a concentration of 14 g mL^{-1} was mixed and homogenized for 30 min at 400 rpm.

Graphite felts (SGL carbon, Germany, hereinafter GFs) with different thicknesses (2.5, 4.6, and 6.0 mm) were used as a support for the carbon slurry. Additional information about the used GFs is displayed in Table 3. As received, GFs were treated in a furnace at 400 °C for 3 h, using a heating rate of 5 °C min^{-1}, under air atmosphere, and were left to cool naturally in the furnace. Next, these GFs were cut into pieces of 3.0 × 3.0 cm and immersed in the AC carbon slurry by dip coating (after 10 s of immersion, the pieces were removed). Subsequently, the GF-AC electrodes were dried in a vacuum furnace at 140 ˚C for 4 h (hereinafter GF-AC, where x is the electrode thickness after cell assembling) and can be seen in Fig. 24. Several electrodes (at least 4 electrodes of each thickness) were prepared and the average mass loading obtained was 39.3 ± 1.6 mg of AC cm^{-2}. Additional GF-AC electrodes were prepared using the GF of 2.5 mm of thickness, however changing the mass loading of AC (31.6 ± 2.1 mg AC cm^{-2} and 55.5 ± 1.7 mg AC cm^{-2}). Moreover, to evaluate the effect of AC dispersion on GF in terms of electrode performance, electrodes containing 32.7 ± 1.8 mg AC cm^{-2} were prepared using a carbon ink with a concentration of 7 g mL^{-1}.

Table 3 – Material data for the graphite felts used in this work according to the manufacturer.

Typical properties	Unit	GFD 2.5 EA	GFD 4.6 EA	GFA 6 EA
Carbon fiber precursor		PAN	PAN	Rayon
Bulk density	g cm^{-3}	0.09	0.09	0.08
Nominal thickness	mm	2.5	4.6	6.0
Area weight	g m^{-2}	250	465	500
Open porosity	%	94	94	95
BET surface area	$m^2 g^{-1}$	0.4	0.4	0.8
Electrical resistivity ⊥	Ω mm	< 5	< 5	< 12
Electrical resistivity ‖	Ω mm	< 3	< 3	< 4
Total impurities	%	< 0.05	< 0.05	< 0.1

Source: adapted from (SGL GROUP - THE CARBON COMPANY, [s.d.]).

PAN – poliacrilonitrile; ⊥ vertical to longitudinal direction of felt; || parallel to longitudinal direction of felt

Figure 24 – GF-AC_x electrodes prepared via dip coating.

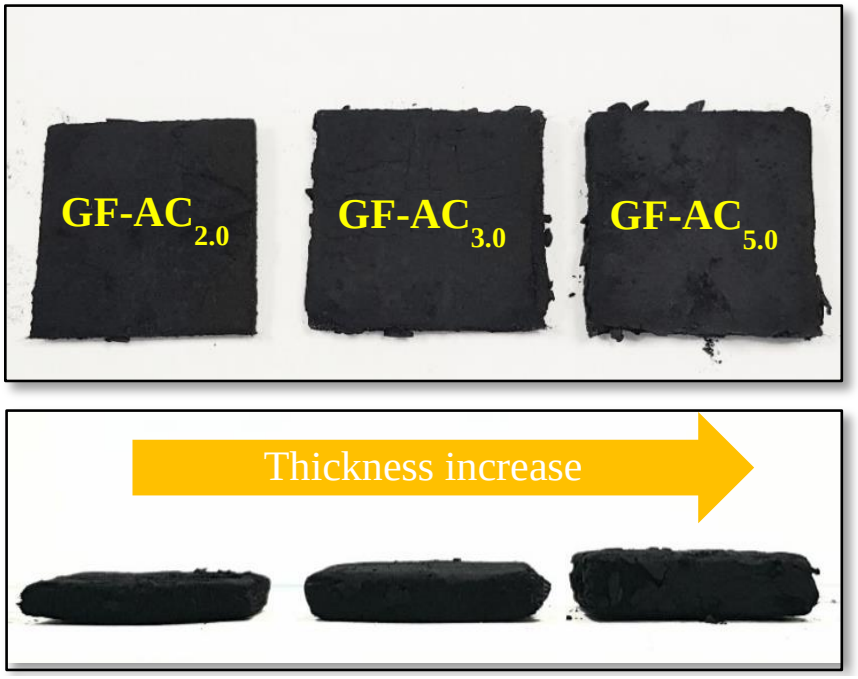

Source: the author.

3.2.1.2 Electrode characterization

In order to evaluate the electrochemical performance of the electrodes, cyclic voltammetry (CV) and electrochemical impedance spectroscopy (EIS) techniques were used. A K_2SO_4 solution 0.5 mol L^{-1} was used as electrolyte. CV and EIS experiments were performed using a "T-type" Swagelok® cell in a three-electrode configuration, wherein GF-AC_x electrodes were cut into a circular-shape (0.785 cm^2), a platinum mesh and an $Ag_{(s)}|AgCl_{(s)}$, $Cl^-_{(aq)}$ (3.5 M) electrode were employed as working (WE), counter (CE) and reference (RE) electrodes, respectively. A cellulosic separator was used between WE and CE. The measurements were conducted using an electrochemical workstation (Biological VMP3 multichannel potentiostat-galvanostat) coupled with EC-Lab v10.44 software.

Analyses of CV curves were performed at different scan rates ranging from 200 to 1 mV s^{-1}, in the voltage window of -0.2 to 0.8 V. It is important to highlight that the electrodes were electrochemically conditioned using 100 CV cycles at 20 mV s^{-1}, using the aforementioned voltage window. Capacitance values were calculated from the CV curves

using Equation 12 (WANG et al., 2019). In order to evaluate the stability of the system, EIS experiments were conducted after finishing each CV analysis at determined scan rates, by applying an amplitude sinusoidal perturbation of 10 mV at 0 V potential over a frequency range from 200 kHz to 10 MHz at open circuit potential (WANG et al., 2019).

$$C(F) = \frac{\int_{V_1}^{V_2} i\, dV}{\nu \cdot \Delta V} \qquad (12)$$

where i (A) is the current, ΔV (V) is the potential window, and ν (V s^{-1}) is the scan rate. To calculate specific capacitance (C_{sp}), C was divided by the electrode mass (g).

In addition, scanning electron microscopy (SEM) images were obtained using a SEM Tabletop Microscope (TM-1000, Hitachi) to examine the surface of the electrodes. The samples were cut with a blade and the images were acquired from the inner structure of the materials

3.3.1 CDI system

CDI experiments were performed in batch mode using a flow cell (10 cm^2) consisting of two GF-AC electrodes, a microporous separator (Celgard®), titanium foils as current collectors, and gaskets (Viton® rubber) of 1 and 2 mm thick. The cell was held together using propylene carbonate pieces (Proingesa), steel plates, and screws (Fig. 25). According to the number of gaskets used, the electrodes prepared using GFs of 2.5, 4.6, and 6.0 mm of thickness were compressed to 2.0, 3.0, and 5.0 mm, respectively, in the assembled cell. A Masterflex Model 77521-47 pump fitted with a Masterflex pump head (Type 7518-00) was connected to the CDI cell with Viton tubing via PTFE connectors. The flow rate was adjusted to 1.8 mL s^{-1}. Aqueous solutions 2000 mg L^{-1} of NaCl (pH 6.0 ± 1.0) were freshly prepared with Milli-Q water (18 MΩ cm resistivity) and used as electrolyte. Typically, the experiments were performed at 298 K, using 65 mL of the electrolyte solution.

Figure 25 – (a) Schematic CDI cell and its elements. (b) Pictures of the CDI cell assembled and (c) the CDI system.

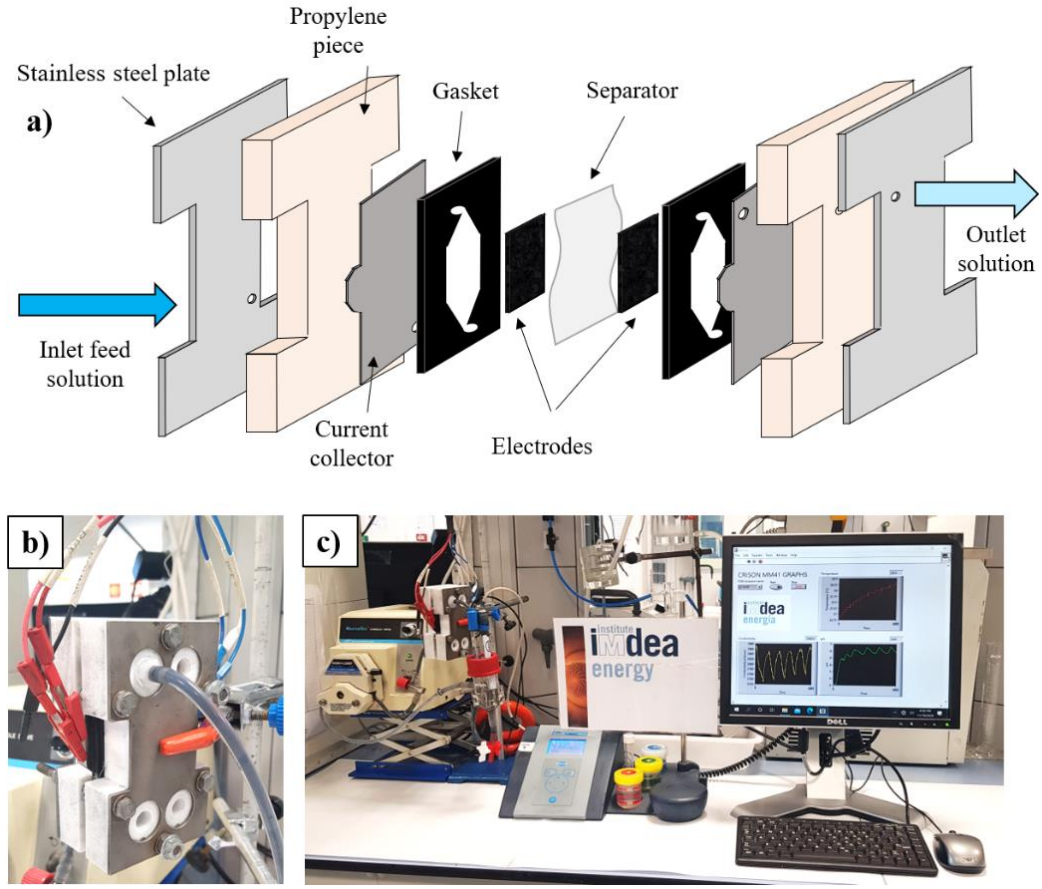

Source: the author.

Electrochemical measurements were controlled and monitored by an electrochemical workstation (Biologic VMP3) using EC-Lab v10.44 software. The variables studied in this work are displayed in Table 4 (based on Hawks et al. (HAWKS et al., 2019)) and represented by Equations 13 – 18. Calculations were based on the average value of the last three consecutive deionization/regeneration cycles (out of five cycles) conducted in the assembled cell when steady-state had been reached. The experiments were conducted using different charge/discharge currents (20/-10, 30/-15, 40/-20 mA) and maximum cell voltages (1.0, 1.1, 1.2 V) under constant current mode. Conductivity, pH, and temperature were monitored in a recycle vessel using an MM41 Kit, Crison, and the data were recorded on a computer by LabView software. The correlation between conductivity and salt concentration was determined according to a calibration curve (Fig. B1). Fluctuations in pH had been observed during the CDI assays (maximum of 2.0 units of pH) and can be attributed to the adsorption/desorption of H_3O^+/OH^- ions, since these changes are reversible (HAN et al.,

2013). Their contribution to the conductivity values was considered neglectable for purposes of calculations presented in this work.

Table 4 – Metrics of CDI performance.

Variable	Description	Unit
Δc	Concentration reduction after desalination	mg L^{-1}
[a]SAC	Salt adsorption capacity in terms of active mass	mg g^{-1}
[a]$ASAR$	Average salt removal rate in terms of active mass considering the whole cycle	mg g^{-1} min^{-1}
Λ_{cycle}	Charge Efficiency	%
[b]E_V	Energy consumption per cubic meter of solution	Wh m^{-3}
[c]P	Water production in terms of the electrode face area	L m^{-2} h^{-1}

Source: the author.

[a]mass of the active material of both electrodes was used for these calculations; [b]no energy recovery was considered; [c]50% water recovery was considered

$$\Delta c = c_{feed} - c_{out} \quad (13)$$

$$SAC = \frac{\Delta c \cdot V}{m_{AC}} \quad (14)$$

$$ASAR = \frac{SAC}{\Delta t} \quad (15)$$

$$\Lambda_{cycle} = \frac{F \cdot \Delta c \cdot V}{q_{in}} \quad (16)$$

$$E_V = \frac{E_{in}}{V} \quad (17)$$

$$P = \frac{V_{50\%}}{A_{face} \cdot \Delta t} \quad (18)$$

Wherein c_{feed} (mg L^{-1}) and c_{out} (mg L^{-1}) are the feed and effluent concentrations, V (L) is the volume of electrolyte, m_{AC} (g) is the mass of activated carbon in both electrodes, Δt (min) is the time for the whole CDI cycle, F (96485 C mol^{-1}) is the Faraday's constant, E_{in} (Wh) is the total energy input during CDI charging process (considering no energy recovery) and $V_{50\%}$ (L) is the volume considering 50% of water recovery.

3.4 Results and Discussion

3.4.1 Electrochemical characterization

Fig. 26 shows the results of CV and EIS experiments of GF-AC electrodes of different thicknesses (2.0, 3.0, and 5.0 mm) but with similar mass loadings (29.8 ± 2.5 mg of AC cm^{-2}). As depicted by the rectangular shape in CV profiles obtained at 10 mV s^{-1} in Fig. 26a, the electrodes exhibited the typical behavior of double layer capacitors, with a noticeable increase in specific capacitance (F g_{AC}^{-1}) when decreasing electrode thickness (Fig. 26b). The lower charge transfer resistance and higher ion penetrability associated with thinner electrodes are the main reasons for this improvement (KIM et al., 2014). Ion penetrability evaluates the depth of ion penetration observed by alternating current, relative to the average pore length, which is the mean distance an ion travels inside the electrode to reach the EDL. Moreover, when it comes to thinner electrodes, the lower contact resistance with the current collector and lower ionic resistance within the electrode itself contribute to the smaller high-frequency results as shown in the EIS spectra (Fig. 26c) (KUO et al., 2020; WANG et al., 2019). These arcs, resulting from the aforementioned resistances, are related to the equivalent series resistance (ESR), whose values for GF-$AC_{2.0}$, GF-$AC_{3.0}$ and GF-$AC_{5.0}$ were 4.0 Ω cm^2, 6.1 Ω cm^2 and 21.3 Ω cm^2, respectively. Therefore, based on these results, one could hypothesize that GF-$AC_{2.0}$ should exhibit the best performance in terms of salt adsorption capacity (*SAC*), followed by GF-$AC_{3.0}$ and GF-$AC_{5.0}$.

Figure 26 – Comparison of GF-AC$_x$ performance using (a) CV analyses at 10 mV s^{-1}, (b) specific capacitance at different scan rates, and (c) EIS measurements. Performance evaluation of GF-AC$_{2.0}$ with different AC mass loadings in terms of (d) capacitance and (e) specific capacitance.

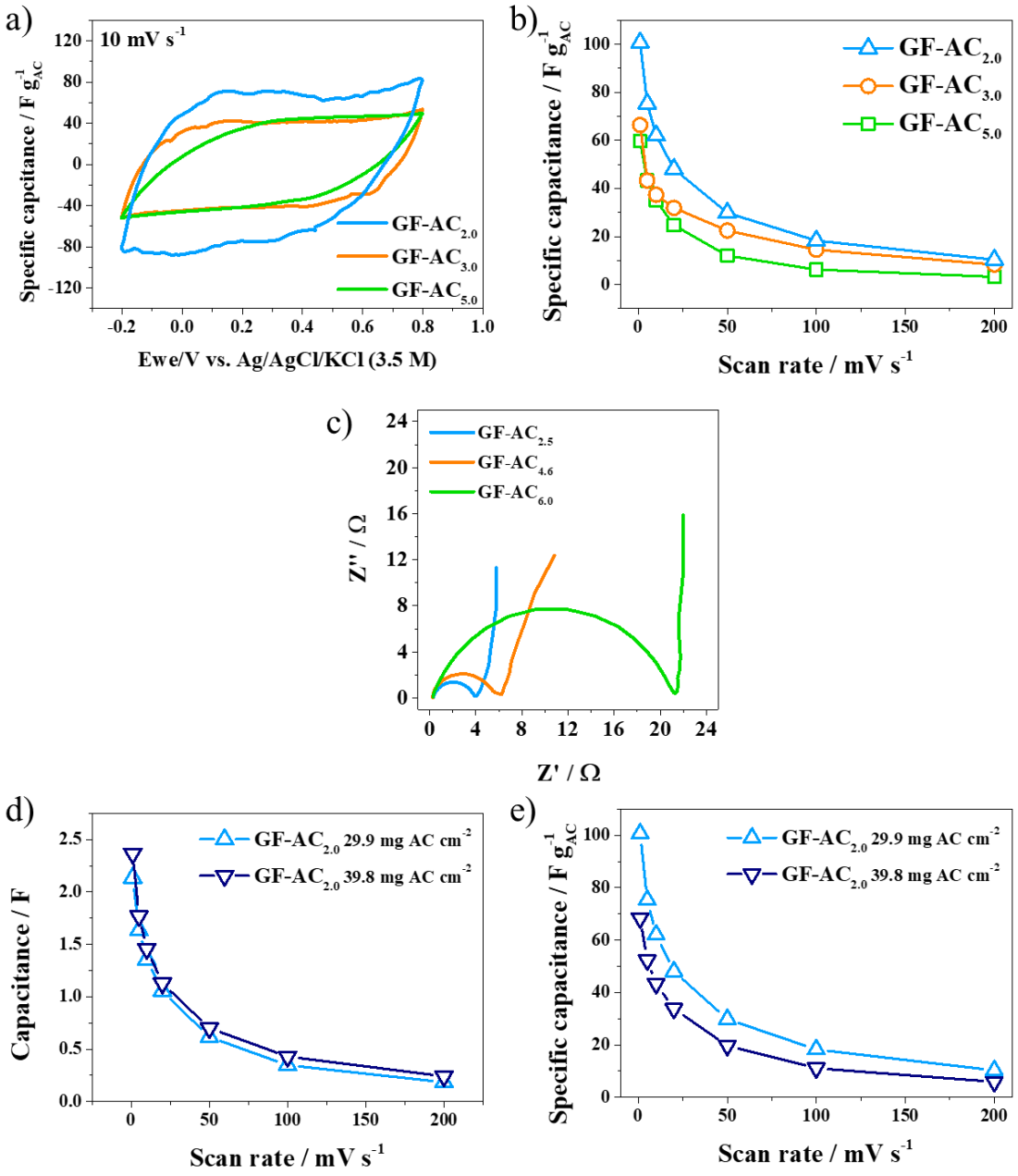

Source: the author.

Furthermore, the CV results indicate that the electrode thickness of the graphite felt is mainly responsible for the observed losses in specific capacitance. This can be inferred because the mass loading of activated carbon is essentially the same for all the materials, and

the GF itself has a negligible contribution to ion storage, which is related to its low surface area (0.4 – 0.8 $m^2 g^{-1}$), as previously demonstrated (WANG et al., 2019). Despite the favorable electrical properties and open three-dimensional structure of the GFs, longer pathways (as electrode thickness increases) contribute to hindering ion penetration and thereby decreasing specific capacitance (KIM et al., 2014).

Our second hypothesis in this study relates to the impact of increasing the mass loading on the ion storage capacity of the GF-AC. In an attempt to improve total capacitance (as an indication of a potentially positive impact on the removal of salts), GF-$AC_{2.0}$ electrodes with a higher mass loading of AC (39.8 mg AC cm^{-2}) were synthesized and characterized by cyclic voltammetry. Fig. 26d shows slightly higher capacitance (in Farads) for this material over the whole range of scan rates. The difference between these two materials with different mass loadings is more significant (23.3 and 30.8%) at higher scan rates (100 mV s^{-1} and 200 mV s^{-1}, respectively), while for scan rates below 50 mV s^{-1}, the difference ranged between 6.9% and 13.8%. Nevertheless, when normalized by the mass of active material (Fig. 26e), the electrode with the lower mass loading (29.9 mg AC cm^{-2}) clearly outperformed the electrode with the higher content of AC (39.8 mg AC cm^{-2}). These conclusions are in accordance with the results obtained using carbon film electrodes, wherein a larger capacity (F) was obtained by increasing the mass loading, although with a decay in specific capacitance (F g_{AC}^{-1}) (KIM et al., 2014; SANTOS et al., 2018). These results reveal that, in terms of ion electrosorption, an increment in the amount of activated carbon could enable a higher ion removal (the higher the capacitance, the higher its capacity to store ions), although with a lower *SAC* (the lower the specific capacitance, the lower its capacity to store ions per gram of active material) (ZORNITTA et al., 2016) and *ASAR* (for the same scan rate, the electrode with a higher content of active material resulted in a lower specific capacitance) (KIM et al., 2014).

3.4.2 Effect of electrode thickness on CDI performance

3.4.2.1 SAC and ASAR

The effects of current rate and cell voltage on the variables *SAC* and *ASAR* using the GF-AC_x electrodes are displayed in Fig. 27. In general, increasing the voltage positively

impacted the salt adsorption capacity of the electrodes. Based on Equation 12, the amount of charges stored at the electrode/electrolyte interface can be defined as the product between the capacitance and the applied voltage. Therefore, the charges stored and consequently the amount of ions electrosorbed should increase with the cell potential. Additionally, the enhancement of salt removal would be also explained by the thinner EDL formed within the AC pores when applying higher potentials, which would increase the amount of active sites available for ion adsorption (HAN et al., 2013; ZORNITTA et al., 2016). When working with microporous materials, the EDL overlapping inside the pores is detrimental for the electrosorption capacity and occurs in pores with a width smaller than a specific value, the called cutoff pore width (YANG et al., 2001).

Figure 27 – Effect of electrode thickness on the performance of GF-AC$_x$ at different voltages and currents in terms of (a) *SAC* and (b) *ASAR* at 1.2 V.

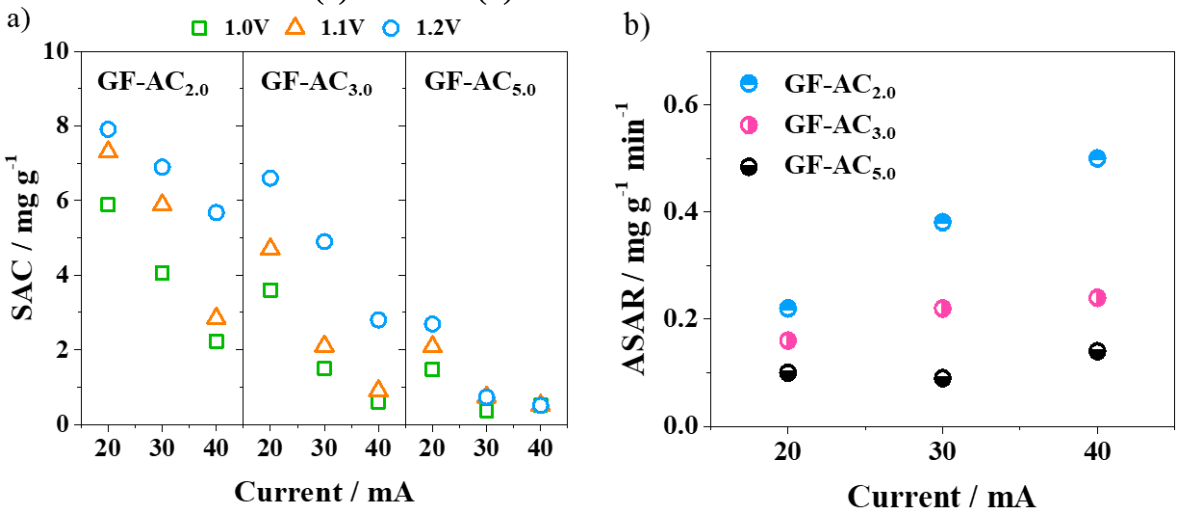

Source: the author.

On the other hand, increasing the current was detrimental for the removal capacity, since high currents may not enable an effective ion diffusion throughout the electrode, lowering the salt removal. In addition, Choi reported that as the current density increases, the electrode potential is reduced and so is the adsorption of ions (CHOI, 2014). For example, when the current density changed from 5.0 to 20.0 A m^{-2}, the final calculated electrode potential reduced from 0.54 to 0.41 V, due to the increase in voltage drop in the solution. The electrosorption is therefore proportional to the electrode potential instead of the cell potential. Moreover, Reale and Smith stated that by examining CV curves, they found that the higher the electrode thickness, the longer is the time for capacitance to be fully developed, thus

explaining the substantial reductions observed here in the specific capacitance of thicker electrodes (REALE; SMITH, 2018). Thereby, higher currents contributed to the drop in ion adsorption, especially for thicker electrodes, wherein the longer period to develop the capacitance also impacts the *SAC* values.

Based on the results shown in Fig. 27a, one might note that the effect of the current and the potential on *SAC* was more pronounced for GF-$AC_{2.0}$ and GF-$AC_{3.0}$ electrodes than in GF-$AC_{5.0}$. As previously observed when modifying the cell potential, *SAC* decreased as the electrode thickness increased, reaching the maximum values of 7.9 mg g_{AC}^{-1} (GF-$AC_{2.0}$), 6.6 mg g_{AC}^{-1} (GF-$AC_{3.0}$), and 2.7 mg g_{AC}^{-1} (GF-$AC_{5.0}$) at 1.2 V and charge/discharge currents of 20 mA/10 mA. This result correlates well with previous works that report that an increment in the electrode thickness of carbon films does not necessarily increase the percentual of usable mass of active material in the electrode (this is reflected in lower *SAC* values) (AGARTAN et al., 2019; SANTOS et al., 2018; ZORNITTA et al., 2016). In our study the mass loading of carbon is essentially the same for the three electrodes, so the increase in thickness is not accompanied by an increase in the mass of active material, as in the case of carbon films. However, the explanation for the drop in electrode performance by increasing the thickness is still valid, wherein longer pore lengths of thicker electrodes diminish ion penetrability and thus the amount of salt removed when normalized by the mass of active material.

In terms of kinetics, Fig. 27b displays the values of *ASAR* at 1.2 V, where the highest *SAC* values were obtained, and it was observed that the higher the current density, the faster the salt removal (WANG; LIN, 2018). Also, as can be seen in Table B1, high voltages improved the kinetics of adsorption, agreeing with previous studies employing activated carbon electrodes (HEMMATIFAR et al., 2016; MOSSAD; ZOU, 2013b; ZHAO et al., 2016), and moderately high levels of *SAC* were obtained (maximum of 7.9 mg g_{AC}^{-1} at 1.2V, 20/10 mA) without sacrificing *ASAR* (0.22 mg g^{-1} min^{-1}). Additionally, GF-AC_x electrodes resulted to be competitive when compared to others using flow through architecture (Table 5), making the use of GF as support of active materials promising in terms of adsorption kinetics due to its more open three-dimensional structure (better electrolyte permeability).

Among the electrodes prepared in this work, GF-$AC_{2.0}$ was the most influenced by the increment in current density with respect to adsorption kinetics (Table B1). A boost in *ASAR* by 2.3 times (from 0.22 to 0.50 mg g^{-1} min^{-1}) was observed when the charge currents

increased from 20 mA to 40 mA at 1.2 V. Regarding the thicker electrodes, it was noted that they were also positively impacted, although experiencing a lower improvement in their performance (from 0.16 to 0.24 mg g^{-1} min^{-1} for GF-$AC_{3.0}$ and from 0.10 to 0.14 mg g^{-1} min^{-1} for GF-$AC_{5.0}$). Additionally, the highest reduction in feed concentration (67.2 mg L^{-1}) was obtained for GF-$AC_{2.0}$, which is in accordance with the highest value of *SAC* observed (7.9 mg g^{-1}). In this way, although electrodes with higher thickness could enable a higher distribution of active material on its structure, the presence of longer pore lengths are detrimental to both salt removal and kinetic of ion adsorption.

Table 5 – Comparative table with other carbon materials using flow through CDI.

Materials	***SAC*** **mg g^{-1}**	***ASAR*** **mg g^{-1} min^{-1}**	***Δc*** **mg L^{-1}**	Λ_{cycle} **%**	**Reference**
Graphite felt coated activated carbon [a]	5.7–7.9	0.22–0.50	48.5–67.2	42–62	This work
Carbon aerogel monoliths [b]	1.7	0.17	432.5	57	(HAWKS et al., 2019)
Carbon aerogel monoliths [c]	4.2	~ 0.43	~ 233.8	~80	(HAWKS et al., 2018)
Activated carbon cloths [d]	10-16	-	-	75-89	(KIM et al., 2017)
Activated carbon cloth[e]	~ 7.0	-	81.8	51	(ALGURAINY; CALL, 2020a)
Activated carbon cloth [f]	3.7	0.32	17.5	< 20	(REMILLARD et al., 2018a)
Carbon nanofoam [f]	2.9	0.18	11.7	< 20	(REMILLARD et al., 2018a)
TiO_2@carbon nanofiber [g]	12	-	-	~50	(GUO et al., 2020)

[a] C_{feed} = 2000 mg L^{-1}, E_{cell} = 1.2 V; [b] C_{feed} = 1170 mg L^{-1}, E_{cell} = 0.9 V; [c] C_{feed} = 2925 mg L^{-1}, E_{cell} = 1.2 V; [d] C_{feed} = 292 mg L^{-1}, E_{cell} = 1.2 V; [e] C_{feed} = 585 mg L^{-1}, E_{cell} = 1.2 V; [f] C_{feed} = 292 mg L^{-1}, E_{cell} = 1.2 V; [g] C_{feed} = 2500 mg L^{-1}, E_{cell} = 1.2 V.

3.4.2.2 Charge efficiency

Charge efficiency (Λ_{cycle}) was evaluated for the different GF-AC$_x$ electrodes to provide additional information about the effectiveness of the CDI process (HAWKS et al., 2019). Table B2 shows the values of Λ_{cycle} for the GF-AC$_x$ electrodes at different voltages and currents. GF-AC$_{2.0}$ achieved values of Λ_{cycle} from 42% to 76% by only modifying the current rate and voltage, indicating more effective utilization of the input charges. These results are higher than the average values reported elsewhere (ALGURAINY; CALL, 2020b; GAO et al., 2014; HAWKS et al., 2018; LI et al., 2015; REMILLARD et al., 2018b), especially considering that charge efficiency for CDI is typically below 80% (PORADA et al., 2013) (values above 80% were achieved by implementing ion exchange membranes in CDI). On the other hand, Λ_{cycle} substantially decreased to 13 – 39% when using thick electrodes. Overall, the results show a drop in Λ_{cycle} as the electrode thickness is increased and as the cell is charged at higher potentials, likely due to resistive and Faradaic losses, respectively. Therefore, to examine these results more closely, a comparison of the inefficiencies occurring at 1.2 V is shown in Fig. 28.

Figure 28 – Effect of voltage and current on GF-AC$_x$ performance in terms of (a) Λ_{cycle}, (b) voltage drop and (c) estimated Faradaic loss at 1.2 V using different currents.

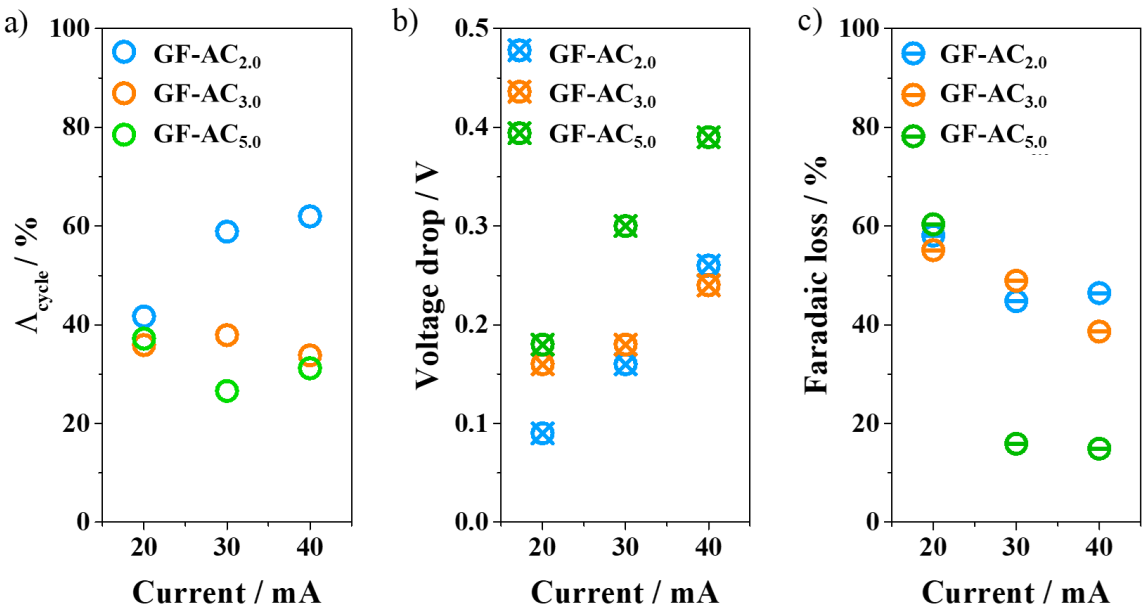

Source: the author.

In Fig. 28a, a drop in Λ_{cycle} was observed when increasing the thickness from 2.0 mm (42 – 62%) to 5.0 mm (27 – 37%) by considering the same conditions of current at 1.2 V. These results indicate that either resistive or Faradaic losses were more significant in thicker electrodes. Figs. 3.5b and 3.5c illustrate these losses by measuring the voltage drop and the impact of parasitic redox reactions, respectively (the details for the calculation of the Faradaic losses are described in the Annex B).

Values of voltage drop plotted in Fig. 28b clearly indicate that it has a larger impact of resistive losses for thicker electrodes. By increasing the current, the effect of the ohmic processes i.e., series resistance, was even more relevant (higher voltage drop). On the other hand, increasing the current minimize losses due to Faradaic processes (Fig. 28c) by reducing the potential developed at the electrode (CHOI, 2014) and by shortening the period that the electrodes experience higher voltages (HEMMATIFAR et al., 2016). Regarding the thin electrodes, despite being the most affected by Faradaic reactions, they showed the lowest impact due to ohmic losses. Since the highest values of Λ_{cycle} were achieved for the thin electrodes, it can be inferred that the resistive process is the main responsible factor for the drop in Λ_{cycle} (HEMMATIFAR et al., 2016).

In summary, thicker electrodes were more penalized by ohmic process and thinner electrodes by Faradaic losses. Therefore, a balance between these two effects should be taken into account when selecting the most suitable electrode thickness and operational conditions for CDI applications. In our case, the thinnest electrode exhibited the highest Λ_{cycle}, which enabled one to improve the CDI performance in terms of both *SAC* (2.2 – 7.9 mg g_{AC}^{-1}) and Δc (19.3 – 67.2 mg L^{-1}).

3.4.2.3 Energy and productivity

Productivity (*P*) and energy consumption (E_V) and are two important parameters in CDI systems directly affected by the operational conditions used to run the desalination process. While *P* is expected to have a strong impact on the capital costs, operational costs will be influenced by E_V (HAWKS et al., 2019). When considering *P*, it is important to consider that the experiments performed in this study were conducted in a batch mode using the same constant flow rate for all the experiments with 50% of water recovery. Furthermore, the calculation of E_V did not consider energy recovery during regeneration.

Figure 29 – Effect of voltage and current on GF-AC$_x$ performance in terms of (a) productivity and (b) energy consumption. The arrows indicate the increment of current or voltage.

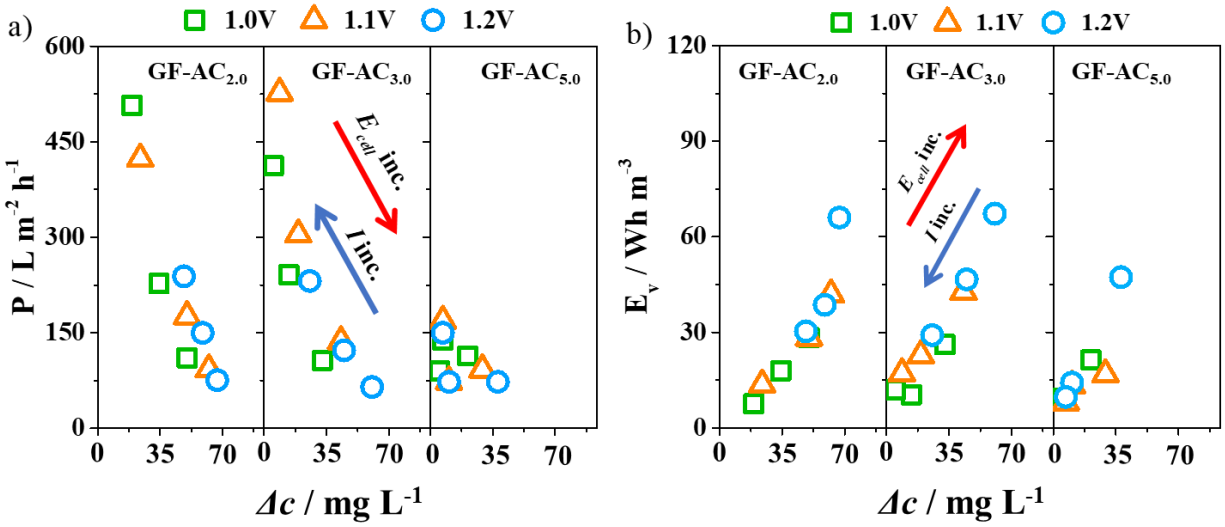

Source: the author.

Results shown in Fig. 29a displayed the trend already observed in previous CDI studies in which larger concentration reductions are associated to lower production and higher energy demand (HAWKS et al., 2019). Thus, a clear tradeoff between P and E_V is observed. CDI experiments using more time-consuming operational conditions, i.e., by employing lower currents and higher potentials, achieved higher salt reductions (higher Δc) but also obtained a lower production and required more of an energy input.

By comparing the three electrode thicknesses, one can notice the narrower range of P for the GF-AC$_{5.0}$ electrode (Fig. 29a). Along with this, Δc achieved a maximum value of 38.0 mg L^{-1} for this electrode, while GF-AC$_{2.0}$ and GF-AC$_{3.0}$ reached maximum values higher than 58.4 mg L^{-1}. Moreover, when considering, for instance, a Δc of ca. 35.1 mg L^{-1}, the productivity of GF-AC$_{2.0}$ was about double and triple of that attained for GF-AC$_{3.0}$ and GF-AC$_{5.0}$, respectively. Regarding E_V (Fig. 29b), although similar ranges were obtained for the three materials, when examining a similar value of Δc, ca. 35.1 mg L^{-1}, the volumetric energies demand increased when larger electrode thickness were employed: 17.9 Wh m^{-3} (GF-AC$_{2.0}$), 26.1 Wh m^{-3} (GF-AC$_{3.0}$), and 47.3 Wh m^{-3} (GF-AC$_{5.0}$).

Since the thinnest material exhibited the best performance for this CDI application under the different parameters and conditions studied, additional experiments were performed

using GF-$AC_{2.0}$ electrodes. In this case, in a further attempt to increase ion removal, the effect of the mass loading of active material was evaluated.

3.4.3.4 Effect of mass loading on CDI performance

The influence of the active material amount on the CDI performance was further analyzed by preparing additional electrodes. Along with the GF-$AC_{2.0}$ electrodes already tested (37.6 ± 0.2 mg AC cm^{-2}), electrodes having two different mass loadings (31.6 ± 2.1 mg AC cm^{-2} and 55.5 ± 1.8 mg AC cm^{-2}) were prepared and tested. In general terms (Table B3), the maximum values of *SAC* achieved for the three different electrodes were in the same range (7.5 mg g^{-1} – 8.1 mg g^{-1}). These results imply that increasing the mass loading do not proportionally increase the usable mass of active material for ion adsorption, which agrees with the results obtained from specific capacitance measurements (Fig. 26e). A higher mass loading can produce more packed electrodes, negatively impacting the electrolyte access to adsorption sites (SANTOS et al., 2018).

The second hypothesis drawn from the electrochemical characterization was related to the increment of total ion removal by increasing the mass loading. Although a clear trend was not presented in terms of *SAC* (Table B3), when salt concentration reduction (Δc) is considered, the highest removal (93.5 mg L^{-1}) was obtained for those electrodes with the highest mass loading (55.5 mg AC cm^{-2}), see Fig 30a. This result agrees with capacitance data obtained from CV analyses (Fig. 26d), wherein an increment in total capacitance, although small, was obtained by increasing the mass loading.

Figure 30 – Evaluation of the effect of different mass loadings of activated carbon on the performance of GF-$AC_{2.0}$ electrodes in terms of (a) salt removal (Δc) and (b) kinetics of salt adsorption (*ASAR*).

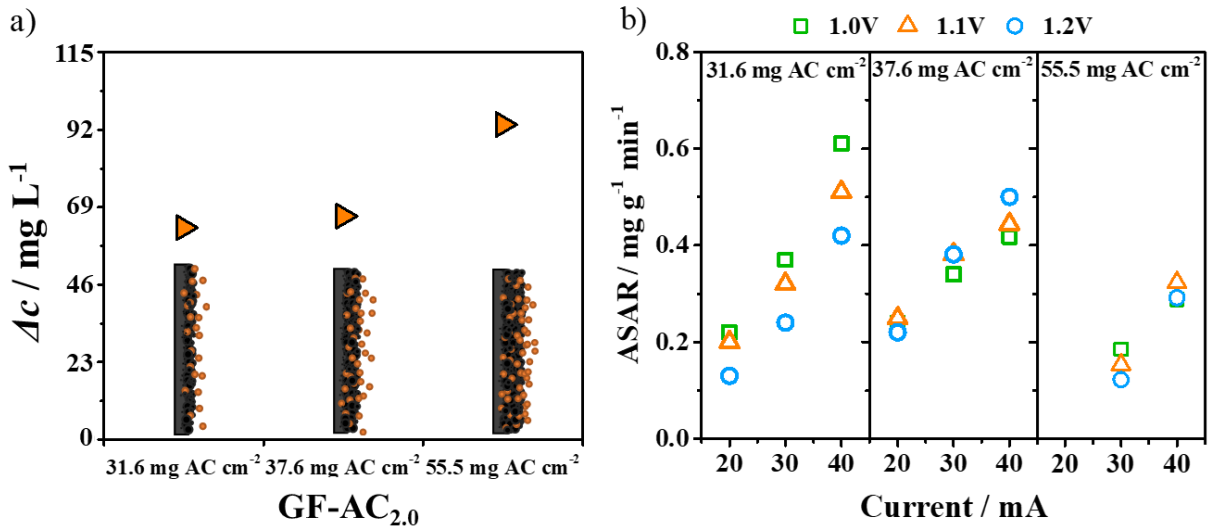

Source: the author.

Regarding ion removal kinetics, a decline in the *ASAR* values was observed when increasing mass loading of AC (Fig. 30b). This effect can be more clearly appreciated when comparing the set of experiments performed with the electrodes containing 31.6 mg AC cm^{-2} and 55.5 mg AC cm^{-2}. For example, the results obtained at 40 mA reached a maximum of 0.61 mg g^{-1} min^{-1} for the 31.6 mg AC cm^{-2} electrodes, decreasing to a maximum of 0.32 mg g^{-1} min^{-1} when 55.5 mg AC cm^{-2} electrodes were employed. These values of *ASAR* seems to be in accordance with the ~ 48% of mass loading increment. One possible explanation, suggested by the higher overpressure observed in the tubing during the experiment performed with the highest mass loading, is that the GF outer structure resulted overloaded of AC during the coating process. Thus, the access of the electrolyte to the internal part of the GF would be hindered by the superficial deposits of AC. As a consequence, the kinetics of adsorption would decrease in comparison with those electrodes with a lower mass loading and a better active material distribution.

To confirm this hypothesis, SEM images were obtained for the electrodes with the three different mass loadings (Fig. 31). The micrographs showed that the carbon ink, in fact, did not properly penetrate the structure of the GF, remaining mainly on its outer surface. However, the images did not allow one to clearly determine whether the increase of the mass loading led to an increment of the carbon layer over the graphite felt. This is due to the fact that some of the activated carbon particles situated on the surface ended up being detached

from the electrode when preparing the samples for SEM analysis. This poses a problem of properly evaluating the thickness of the carbon coating. Our supposition here is that the increment of the mass loading, could either affect the thickness of the AC surface layer or might increase the packing at the surface thereby hampering the flow of solution through the electrode.

Figure 31 – SEM images of GF-$AC_{2.0}$ with different mass loadings.

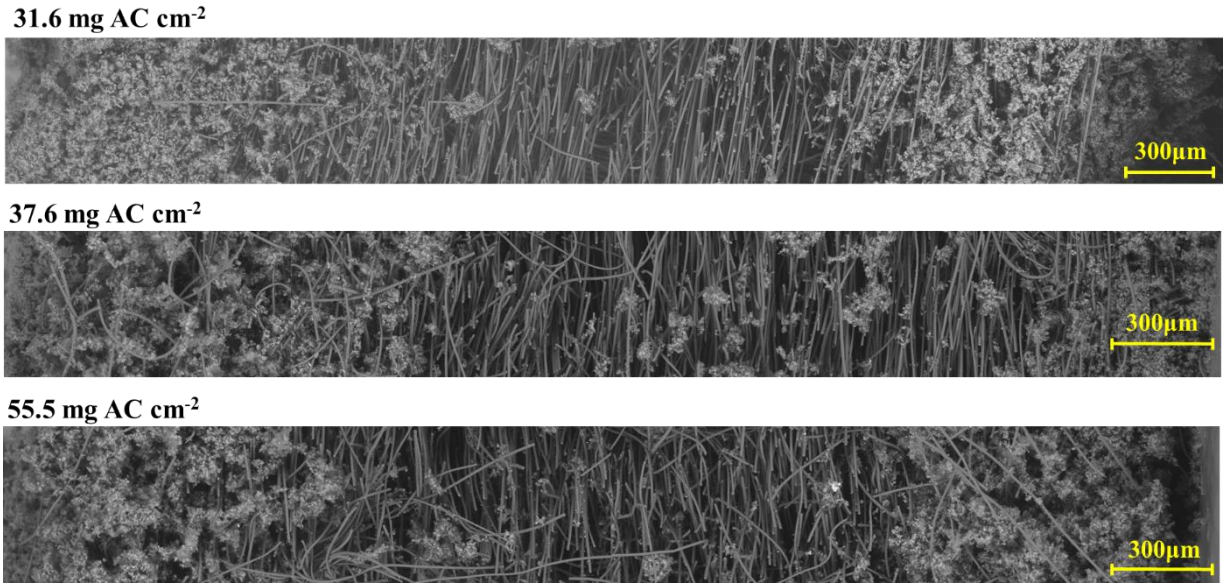

Source: the author.

In addition to this issue, it was observed that the increment of the amount of activated carbon extended the charge/discharge cycles (Fig. 32a). This effect could be related to two different contributions: first, due to the higher amount of active material, a higher salt removal was observed, therefore a larger extension of the cycle was expected; secondly, due to a higher leakage of current related to ohmic and/or Faradaic processes, consequently hindering the electrode polarization and lowering the kinetics of salt removal.

Figure 32 – Effect of current and cell potential on performance of GF-$AC_{2.0}$ electrodes with different mass loadings: (a) charge/discharge cycles at 1.0 V, 30 mA/15 mA, (b) charge efficiency, and (c) charge/discharge cycles for GF-$AC_{2.0}$ 55.5 mg AC g^{-1} under different currents and voltages.

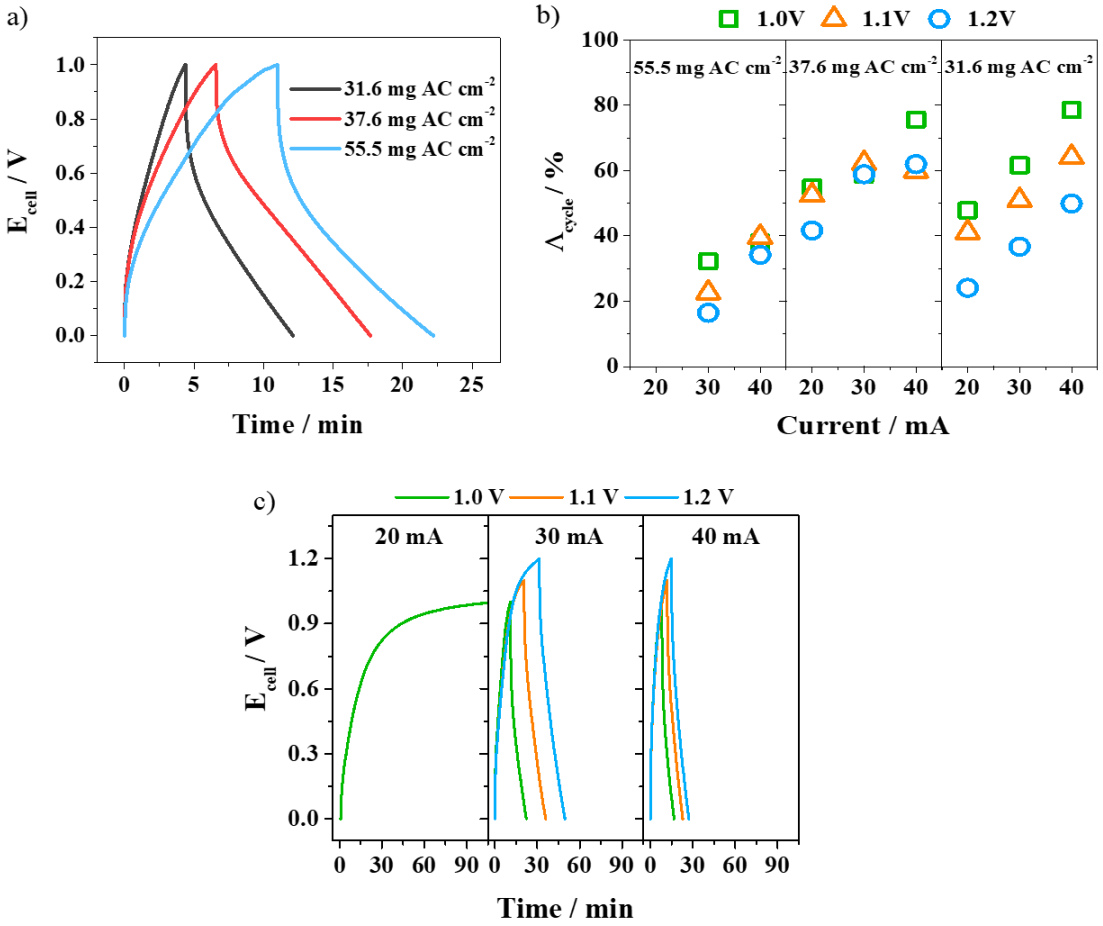

Source: the author.

To further evaluate the extent of these processes, the values of voltage drop (*iR*) for each one of the electrodes were measured when applying different current densities (Table 6). The results show that *iR* values are in a very narrow range when comparing electrodes with different mass loadings at the same operational conditions, therefore ohmic losses are not the main contributors to difficult electrode polarization. On the other hand, by examining the influence of Faradaic processes in Fig. 29a, the cell potential plots show a higher inflexion of the charging curve as the content of active material increases: the more the charging curve moves away from linearity (that indicates an ideal capacitive behavior), the more evidenced is the occurrence of Faradaic processes (CHOI, 2014; HEMMATIFAR et al., 2016; SANTOS et al., 2020). This visual indication is supported by the reduction of charge efficiency values (Fig. 32b), particularly at the highest mass loading. In addition, the performance of the

electrodes with 55.5 mg AC cm^{-2} could not be assessed at 20 mA (Fig. 32c), since the electrodes did not reach the desired potential due to the magnitude of Faradaic reactions at this current rate. Those experiments clearly demonstrate the impact of the Faradaic process on the extension of the charging cycles, being detrimental for CDI performance from two points of view, kinetics and Λ_{cycle}.

Table 6 – Voltage drop from charge/discharge curves of GF-$AC_{2.0}$ electrodes with different mass loadings (1.0 V – 1.2 V).

I_c / I_d mA	***iR* drop** V		
	31.6 mg AC cm^{-2}	37.6 mg AC cm^{-2}	55.5 mg AC cm^{-2}
20 / 10	0.08 ± 0.01	0.09 ± 0.01	-
30 / 15	0.12 ± 0.01	0.16 ± 0.02	0.11 ± 0.03
40 / 20	0.17 ± 0.01	0.19 ± 0.01	0.13 ± 0.02

Source: the author.

Regarding productivity and energetic demands (Fig. B3), a trend similar to the one obtained for the electrodes with different thickness was obtained: tradeoff between *P* and E_V, wherein higher values of Δc were achieved at the cost of productivity and energy demand. Comparing the electrodes at a common value of salt elimination (~ 58.4 mg L^{-1}), the sample with 31.6 mg AC cm^{-2} attained a productivity of 191 L m^{-2} h^{-1}, while the other electrodes did not surpass 160 L m^{-2} h^{-1}. Once again, the slower salt removal kinetics of the high mass loading electrodes negatively impacted water production. In terms of E_V, the values were respectively 25.2 Wh m^{-3}, 38.6 Wh m^{-3}, and 49.6 Wh m^{-3} as mass loading increased. Here, the Faradaic losses clearly raised the energy consumption when increasing mass loading.

Based on the results obtained with different amounts of activated carbon we could conclude that, although it is possible to improve salt removal by using electrodes with high mass loadings, parameters such as *ASAR*, *P*, and E_V will determine whether the process could be commercial. Thus, if the goal would be to obtain a high level of desalination, high mass loadings would be interesting, although at a cost of removal kinetics, affecting productivity, and resulting in higher energy demand. Moreover, high mass loading led to increasing the occurrence of Faradaic processes, which would be deleterious for the CDI performance, especially under long-term operation (COHEN et al., 2013; LADO et al., 2015; TANG et al., 2017). In this sense, the selection of these materials might lead to the necessity of replacing

electrodes at shorter time intervals and consequently increasing process cost. By comparing the electrodes in a similar range of salt removal (46.7 – 70.1 mg L^{-1}), the ones having lower amounts of activated carbon exhibited a better performance in terms of *ASAR*, Λ_{cycle}, *P*, and E_V. Furthermore, since these electrodes have less carbon, the costs to produce the electrode would be lower.

3.4.3 Effect of the AC distribution on the GF structure

Considering the SEM results reported in the previous section and with the aim of improving the AC distribution along the GF structure, electrodes were prepared using a carbon slurry with reduced concentration (from 14 to 7 g mL^{-1} by doubling the amount of isopropanol used). As result, GF-AC electrodes containing 32.7 ± 1.8 mg AC cm^{-2} with a more disperse distribution of AC along the GF structure were produced, as it can be appreciated in the SEM images (Fig. 33).

Figure 33 – SEM images of GF-$AC_{2.0}$ with more disperse distribution of AC.

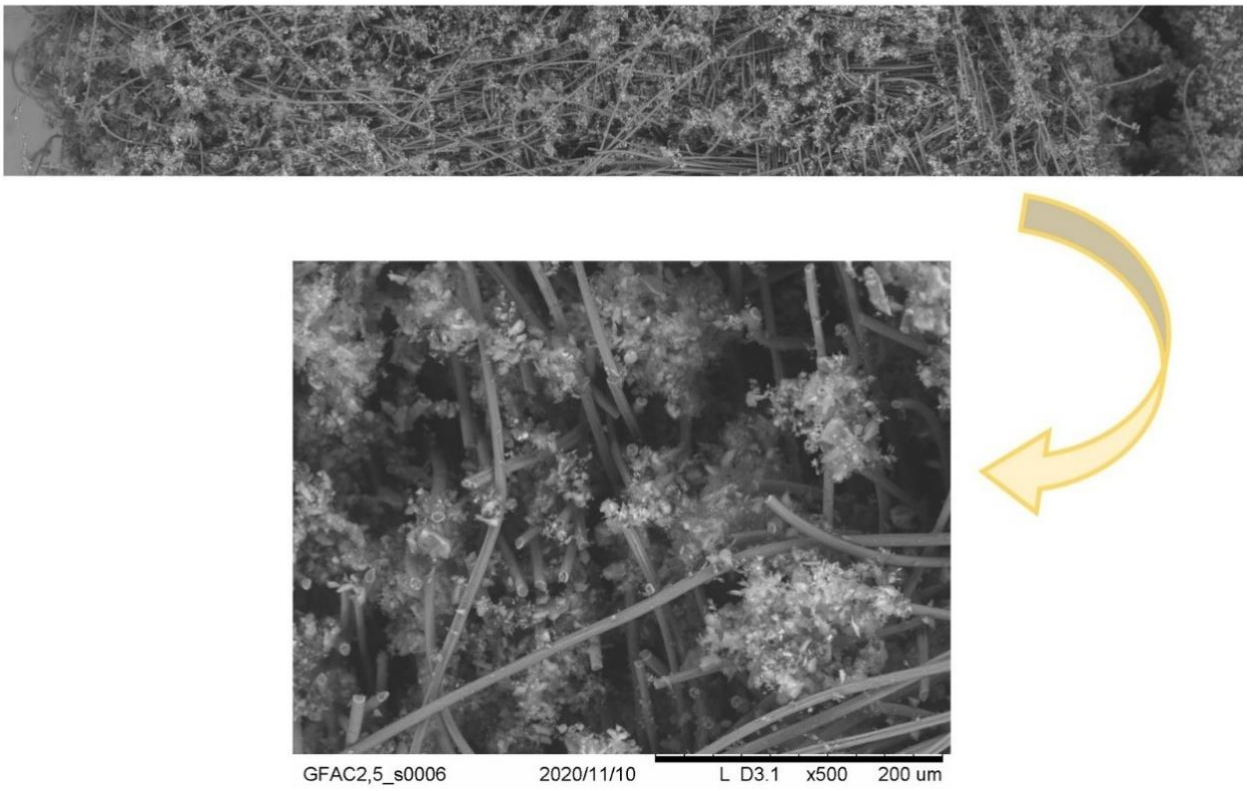

Source: the author.

Additional CDI tests were performed with the highly disperse GF-AC electrodes. As shown in the CDI Ragone plot (Fig. 34), these electrodes achieved a better performance (*SAC* 8.1 – 9.1 mg g^{-1} and *ASAR* 0.21 – 0.32 mg g^{-1} min^{-1}) than the electrodes with a non-homogenous AC distribution (*SAC* 5.7 – 7.5 mg g^{-1} and *ASAR* 0.13 – 0.22 mg g^{-1} min^{-1}). Moreover, a charge efficiency of ~ 54%, a productivity of 103 L m^{-2} h^{-1} and a quite low energy demand of 36.2 Wh m^{-3} were reached, along with superior Δc values (60.8 – 67.2 mg L^{-1}, high dispersed AC, *versus* 45.2 – 59.3 mg L^{-1}, low dispersed AC). These results show that a uniform distribution of the active materials improves the access of ions to the active adsorption sites by reducing the packing of AC, thus leading to a superior electrochemical performance (DELAPORTE et al., 2020; KOHLMEYER et al., 2016; WOUTERS et al., 2016, 2018).

Figure 34 – CDI Ragone plot comparing the effect of AC dispersion on the performance of GF-$AC_{2.0}$ electrodes. Experiments performed at 1.0 V, using 20 mA/10 mA of charging/discharging currents.

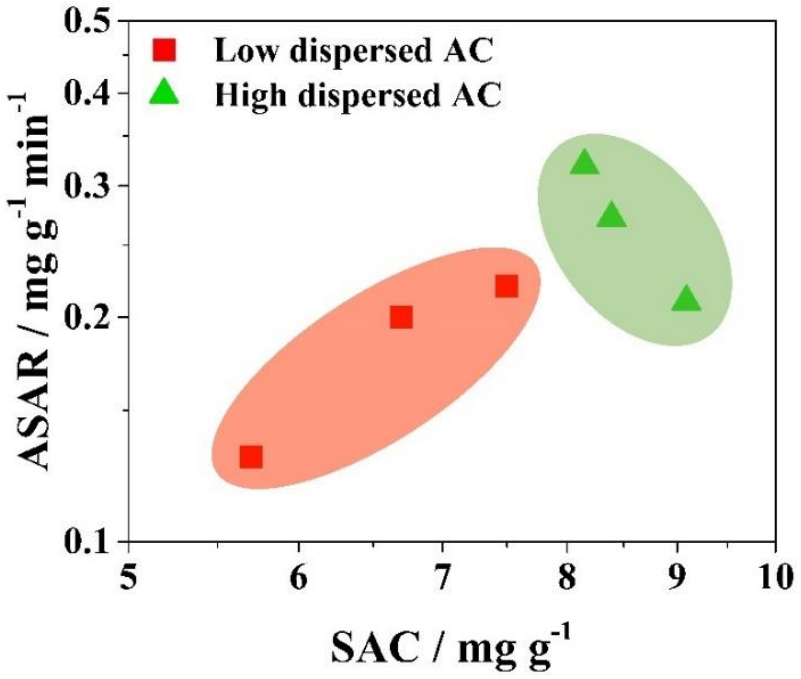

Source: the author.

Therefore, a brief analysis of the data reported herein demonstrated that, by combining a suitable electrode thickness and mass loading with a proper dispersion of active

material throughout the structure of the electrode, enable one to prepare an electrode with higher and faster ion removal capacities, without sacrificing Δc.

3.5 Conclusion

In this work, electrodes of AC supported on GF were prepared in order to evaluate the effect of electrode thickness, AC mass loading and its distribution on CDI performance. The electrochemical characterization of the synthesized samples led to propose that increasing specific capacitance (F g^{-1}) by decreasing electrode thickness, one can improve *SAC*, and that improving the capacitance (F) by using higher mass loading, one can enhance Δc. Electrosorption experiments demonstrated that by decreasing the thickness of the GF-AC from 5.0 mm to 2.0 mm, values of *SAC* (in some cases) 200% higher were achieved, which proved our first statement, without sacrificing the kinetic of adsorption. In addition, GF-$AC_{2.0}$ exhibited superior productivity at lower energy demand by comparing similar values of Δc (35.1 mg L^{-1}). Additional studies using GF-$AC_{2.0}$ electrodes having different mass loadings revealed that the electrode with the highest mass loading was able to improve Δc by ~ 50%, supporting the electrochemical analyses. However, the boost in Δc was detrimental for *ASAR*, reducing productivity, and led to more energy demand. Additionally, a higher mass loading caused more Faradaic processes, thereby compromising long-term operational performance. Finally, the study of the AC coating distribution showed that a good dispersion of the active material inside the structure of the GF is fundamental to improve CDI performance. More specifically, an enhancement in *SAC*, along with lower E_V demand, was observed, being parameters linked to kinetics the most impacted variables.

To conclude, the results reported in this study show three different simple strategies for modifying GF-AC 3D electrodes with the aim of enhancing the different aspects of CDI performance (not just *SAC* and *ASAR*, but also E_V and *P*). These results pave the way for the future use of GF in electrochemical ion separation technologies, having positive implications for those processes involving water treatments and ion recovery. These topics are extremely relevant nowadays when looking for a more efficient use of resources.

4 CHAPTER IV – GENERAL CONCLUSIONS

The first study reported on the successful synthesis of magnetic graphene oxide modified with amino groups (MAG-GO_1-NH_2), which demonstrated promising results in selectively removing Cr(VI) ions. The ratio of GO to magnetite showed to be crucial to ion removal and selectivity due to changes in the surface charge of the composite. The modified material showed improved performance in Cr(VI) adsorption in relation to Cd(II) and Cu(II) species, which was mainly related to hard-hard and electrostatic interactions between chromium and $–NH_3^+$ groups that can easily bind negative charged chromium species. Moreover, MAG-GO_1-NH_2 was stable and efficient in Cr(VI) removal over 5 cycles of adsorption/desorption, making it a potential platform for selective adsorption of this analyte.

The second study investigated the potential of using simple strategies of electrode preparation to enhance the performance of GF-AC electrodes in capacitive deionization (CDI). As indicated by electrochemical characterization, the electrode thickness and the mass loading of active material played an important role in the capacity and kinetics of salt removal, directly impacting water production and energy demand. In this sense, thinner electrodes with optimal mass loading were capable to achieve higher removal of salts undergoing less Faradaic reactions which are deleterious for long-term operation. This outcome mainly from the lower equivalent series resistances and better electrolyte permeability promoted by the thinner electrode. Additionally, better dispersion of activated carbon in the graphite felt improved ion access to AC micropores throughout the electrode, further boosting CDI efficiency. This study highlights the importance of electrode design and the potential of using GF in electrochemical ion separation technologies, particularly in water treatment and ion recovery.

5 CHAPTER V – SCIENTIFIC PRODUCTION

Published articles

1. Da Silva, Juliana M.; Da Silva, Carlos E.P.; **Freire, Jessica M.A.**; Becker, Helena; Diógenes, Izaura C.N.; Longhinotti, Elisane. Industrial steel waste-based adsorbent: An effective phosphate removal from aqueous media. MATERIALS CHEMISTRY AND PHYSICS, v. 292, p. 126828, 2022.
2. **Freire, Jessica M.A.**; Lado, Julio J.; García-Quismondo, Enrique; Burillo, Gonzalo C.; Palma, Jesús; Loiola, Adonay R.; Longhinotti, Elisane; Anderson, Marc A. Strategies to boost capacitive deionization performance of 3D electrodes. SEPARATION AND PURIFICATION TECHNOLOGY, v. 273, p. 118977, 2021.
3. **Freire, Jessica M.A.**; Matos, Maria A.F.; Abreu, Dieric S.; Becker, Helena; Diógenes, Izaura C.N.; Valentini, Antoninho; Longhinotti, Elisane. Nitrate photocatalytic reduction on TiO_2: Metal loaded, synthesis and anions effect. JOURNAL OF ENVIRONMENTAL CHEMICAL ENGINEERING, v. 8, p. 103844, 2020.

Submitted articles

1. **Freire, Jessica M. A.;** Moreira, Ícaro O.; França, Antonia M. de M.; da Silva, Luiz T. V.; dos Santos, Luis P. M.; Medeiros, Samuel L.S.; de Vasconcelos, Igor F.; Loiola, Adonay R.; Antunes, Renato A.; do Nascimento, Ronaldo F.; Longhinotti, Elisane. Functionalized Magnetic Graphene Oxide Composites for Selective Toxic Metal Adsorption. JOURNAL OF ENVIRONMENTAL CHEMICAL ENGINEERING.
2. do Nascimento, Carlos P.G.; Costa, Mateus S. M. A.; **Freire, Jessica M. A.**; da Silva, Luiz T. V.; Coutinho, Lucas P.; Monteiro, Norberto K. V.; Zampieri, Davila de S.; Oliveira, Juliene T.; do Nascimento, Ronaldo F.; de Carvalho, Idalina M. M.; Becker, Helena; Longhinotti, Elisane. Degradation of xanthene-based dyes by photoactivated persulfate: experimental and computational studies. PHOTOCHEMICAL & PHOTOBIOLOGICAL SCIENCES.
3. da Silva, Juliana M.; Freire, Jessica M. A.; Taniguchi, Carlos A. K.; Diógenes, Izaura C N.; Becker, Helena; Longhinotti, Elisane. Blast furnace sludge loaded with phosphate: evidence of a potential fertilizer. ENVIRONMENTAL SCIENCE AND POLLUTION RESEARCH.

REFERENCES

AD, John. **Lange's handbook of chemistry**. 15th ed ed. [s.l.] : McGrawHill, 1999.

AGARTAN, Lutfi; HAYES-OBERST, Brendan; BYLES, Bryan W.; AKUZUM, Bilen; POMERANTSEVA, Ekaterina; CAGLAN KUMBUR, E. Influence of operating conditions and cathode parameters on desalination performance of hybrid CDI systems. **Desalination**, *[S. l.]*, v. 452, n. August 2018, p. 1–8, 2019. DOI: 10.1016/j.desal.2018.10.025.

AGÊNCIA NACIONAL DE ÁGUAS. **Conjuntura Recursos Hídricos Brasil**. [s.l: s.n.].

AGÊNCIA NACIONAL DE ÁGUAS E SANEAMENTO BÁSICO. Conjuntura Recursos Hídricos Brasil. *[S. l.]*, 2022.

AHLAWAT, Anju; SATHE, V. G.; REDDY, V. R.; GUPTA, Ajay. Mossbauer, Raman and X-ray diffraction studies of superparamagnetic NiFe2O4 nanoparticles prepared by sol – gel auto-combustion method. **Journal of Magnetism and Magnetic Materials**, *[S. l.]*, v. 323, n. 15, p. 2049–2054, 2011. DOI: 10.1016/j.jmmm.2011.03.017.

AL-GAASHANI, R.; NAJJAR, A.; ZAKARIA, Y.; MANSOUR, S.; ATIEH, M. A. XPS and structural studies of high quality graphene oxide and reduced graphene oxide prepared by different chemical oxidation methods. **Ceramics International**, *[S. l.]*, v. 45, n. 11, p. 14439–14448, 2019. DOI: 10.1016/j.ceramint.2019.04.165.

ALGURAINY, Yazeed; CALL, Douglas F. Asymmetrical removal of sodium and chloride in flow-through capacitive deionization. **Water Research**, *[S. l.]*, v. 183, p. 116044, 2020. a. DOI: 10.1016/j.watres.2020.116044.

ALGURAINY, Yazeed; CALL, Douglas F. Asymmetrical removal of sodium and chloride in flow-through capacitive deionization. **Water Research**, *[S. l.]*, v. 183, p. 116044, 2020. b. DOI: 10.1016/j.watres.2020.116044.

AL-JASSIM, Nada; ANSARI, Mohd Ikram; HARB, Moustapha; HONG, Pei-ying. Removal of bacterial contaminants and antibiotic resistance genes by conventional wastewater treatment processes in Saudi Arabia: Is the treated wastewater safe to reuse for agricultural irrigation ? **Water Research**, *[S. l.]*, v. 73, p. 277–290, 2015. DOI: 10.1016/j.watres.2015.01.036.

AL-KARAGHOULI, Ali; KAZMERSKI, Lawrence L. Energy consumption and water production cost of conventional and renewable-energy-powered desalination processes. **Renewable and Sustainable Energy Reviews**, *[S. l.]*, v. 24, p. 343–356, 2013. DOI: 10.1016/j.rser.2012.12.064.

ANDERSON, Marc A.; CUDERO, Ana L.; PALMA, Jesus. Capacitive deionization as an electrochemical means of saving energy and delivering clean water. Comparison to present

desalination practices: Will it compete? **Electrochimica Acta**, *[S. l.]*, v. 55, n. 12, p. 3845–3856, 2010. DOI: 10.1016/j.electacta.2010.02.012.

ANDRES, Ginno L.; YOSHIHARA, Yoshinobu. A capacitive deionization system with high energy recovery and effective re-use. **Energy**, *[S. l.]*, v. 103, p. 605–617, 2016. DOI: 10.1016/j.energy.2016.03.021.

BABY, Rabia; SAIFULLAH, Bullo. Carbon Nanomaterials for the Treatment of Heavy Metal-Contaminated Water and Environmental Remediation. **Nanoscale Research Letters**, *[S. l.]*, v. 14, n. 341, 2019.

BANERJEE, R.; BEVILACQUA, N.; EIFERT, L.; ZEIS, R. Characterization of carbon felt electrodes for vanadium redox flow batteries – A pore network modeling approach. **Journal of Energy Storage**, *[S. l.]*, v. 21, n. September 2018, p. 163–171, 2019. a. DOI: 10.1016/j.est.2018.11.014.

BANERJEE, Rupak; BEVILACQUA, Nico; MOHSENINIA, Arezou; WIEDEMANN, Benjamin; WILHELM, Florian; SCHOLTA, Joachim; ZEIS, Roswitha. Carbon felt electrodes for redox flow battery: Impact of compression on transport properties. **Journal of Energy Storage**, *[S. l.]*, v. 26, p. 100997, 2019. b. DOI: 10.1016/j.est.2019.100997.

BASIRICÒ, L.; LANZARA, G. Moving towards high-power, high-frequency and low-resistance CNT supercapacitors by tuning the CNT length, axial deformation and contact resistance. **Nanotechnology**, *[S. l.]*, v. 305401, 2012. DOI: 10.1088/0957-4484/23/30/305401.

BHATERIA, Rachna; SINGH, Rimmy. A review on nanotechnological application of magnetic iron oxides for heavy metal removal. **Journal of Water Process Engineering**, *[S. l.]*, v. 31, n. March, p. 100845, 2019. DOI: 10.1016/j.jwpe.2019.100845.

BLAIR, JOHN W.; MURPHY, GEORGE W. Electrochemical Demineralization of Water with Porous Electrodes of Large Surface Area. *Em*: **Saline Water Conversion**. [s.l.] : American Chemical Society, 1960. p. 206–223. DOI: 10.1021/ba-1960-0027.ch020.

BOLISETTY, Sreenath; PEYDAYESH, Mohammad; MEZZENGA, Raffaele. Sustainable technologies for water purification from heavy metals: review and analysis. **Chemical Society Reviews**, *[S. l.]*, v. 48, n. 2, p. 463–487, 2019. DOI: 10.1039/c8cs00493e.

BRODIE, Benjamin Collins. On the Atomic Weight of Graphite. **Philosophical Transactions of the Royal Society**, *[S. l.]*, v. 149, p. 249–259, 1859.

CAROLIN, C. Femina; KUMAR, P. Senthil; SARAVANAN, A.; JOSHIBA, G. Janet; NAUSHAD, Mu. Efficient techniques for the removal of toxic heavy metals from aquatic environment: A review. **Journal of Environmental Chemical Engineering**, *[S. l.]*, v. 5, n. 3, p. 2782–2799, 2017. DOI: 10.1016/j.jece.2017.05.029.

CHEN, Bingbing; FENG, Aihu; DENG, Ruixiang; LIU, Kun; YU, Yun; SONG, Lixin. MXene as a Cation-Selective Cathode Material for Asymmetric Capacitive Deionization. **ACS Applied Materials and Interfaces**, *[S. l.]*, v. 12, n. 12, p. 13750–13758, 2020. DOI: 10.1021/acsami.9b19684.

CHEN, Jinghan; ZHANG, Lijuan; LI, Haotian; LU, Menghua; XIE, Jinghan; GUAN, Shaoqi; WANG, Xiang; LIU, Xijian; LU, Jie. Preparation and adsorbability of magnetic composites based on cellulose nanofiber/graphene oxide. **Colloids and Surfaces A: Physicochemical and Engineering Aspects**, *[S. l.]*, v. 639, n. 333, p. 128373, 2022. DOI: 10.1016/j.colsurfa.2022.128373.

CHEN, Xiangnan; WANG, Xiaohui; FANG, De. A review on C1s XPS-spectra for some kinds of carbon materials. **Fullerenes, Nanotubes and Carbon Nanostructures**, *[S. l.]*, v. 28, n. 12, p. 1048–1058, 2020. DOI: 10.1080/1536383X.2020.1794851.

CHEN, Xuli; PAUL, Rajib; DAI, Liming. Carbon-based supercapacitors for efficient energy storage. **National Science Review**, *[S. l.]*, v. 4, n. 3, p. 453–489, 2017. DOI: 10.1093/nsr/nwx009.

CHEN, Yao; ZHANG, Xiong; ZHANG, Haitao; SUN, Xianzhong; ZHANG, Dacheng; MA, Yanwei. High-performance supercapacitors based on a graphene-activated carbon composite prepared by chemical activation. **RSC Advances**, *[S. l.]*, v. 2, p. 7747–7753, 2012. DOI: 10.1039/c1pp05072a.

CHI, Zifang; ZHU, Yuhuan; LIU, Wanting; HUANG, Huazheng; LI, Huai. Selective removal of As (III) using magnetic graphene oxide ion-imprinted polymer in porous media : Potential effect of external magnetic field. **Journal of Environmental Chemical Engineering**, *[S. l.]*, v. 9, n. May, p. 105671, 2021.

CHOI, Jae-Hwan. Determination of the electrode potential causing Faradaic reactions in membrane capacitive deionization. **Desalination**, *[S. l.]*, v. 347, p. 224–229, 2014. DOI: 10.1016/j.desal.2014.06.004.

CHOI, Jongmoon; DORJI, Pema; SHON, Ho Kyong; HONG, Seungkwan. Applications of capacitive deionization: Desalination, softening, selective removal, and energy efficiency. **Desalination**, *[S. l.]*, v. 449, n. June 2018, p. 118–130, 2019. DOI: 10.1016/j.desal.2018.10.013.

COHEN, Izaak; AVRAHAM, Eran; BOUHADANA, Yaniv; SOFFER, Abraham; AURBACH, Doron. Long term stability of capacitive de-ionization processes for water desalination: The challenge of positive electrodes corrosion. **Electrochemica Acta**, *[S. l.]*, v. 106, p. 91–100, 2013. DOI: 10.1016/j.electacta.2013.05.029.

CUONG, Dinh Viet et al. A critical review on biochar-based engineered hierarchical porous carbon for capacitive charge storage. **Renewable and Sustainable Energy Reviews**, *[S. l.]*, v. 145, n. April, p. 111029, 2021. DOI: 10.1016/j.rser.2021.111029. Disponível em: https://doi.org/10.1016/j.rser.2021.111029.

DAHAGHIN, Zohreh; MOUSAVI, Hassan Zavvar; SAJJADI, S. Maryam. Trace amounts of Cd(II), Cu(II) and Pb(II) ions monitoring using Fe3O4@graphene oxide nanocomposite modified via 2-mercaptobenzothiazole as a novel and efficient nanosorbent. **Journal of Molecular Liquids**, *[S. l.]*, v. 231, p. 386–395, 2017. DOI: 10.1016/j.molliq.2017.02.023.

DA'NA, Enshirah. Adsorption of heavy metals on functionalized-mesoporous silica: A review. **Microporous and Mesoporous Materials**, *[S. l.]*, v. 247, p. 145–157, 2017. DOI: 10.1016/j.micromeso.2017.03.050. Disponível em: http://dx.doi.org/10.1016/j.micromeso.2017.03.050.

DAVIES, Trevor; TUMMINO, Joseph. High-Performance Vanadium Redox Flow Batteries with Graphite Felt Electrodes. **Journal of Carbon Research**, *[S. l.]*, v. 4, n. 1, p. 8, 2018. DOI: 10.3390/c4010008.

DELAPORTE, N. et al. Facile formulation and fabrication of the cathode using a self-lithiated carbon for all-solid-state batteries. **Scientific Reports**, *[S. l.]*, v. 10, n. 1, p. 1–11, 2020. DOI: 10.1038/s41598-020-68865-8.

DIMIEV, Ayrat; KOSYNKIN, Dmitry V.; ALEMANY, Lawrence B.; CHAGUINE, Pavel; TOUR, James M. Pristine Graphite Oxide. **Journal of the American Chemical Society**, *[S. l.]*, v. 134, p. 2815–2822, 2012. DOI: dx.doi.org/10.1021/ja211531y.

DIMIEV, Ayrat M.; ALEMANY, Lawrence B.; TOUR, James M. Graphene oxide. Origin of acidity, its instability in water, and a new dynamic structural model. **ACS Nano**, *[S. l.]*, v. 7, n. 1, p. 576–588, 2013. DOI: 10.1021/nn3047378.

DŁUGOŁECKI, Piotr; VAN DER WAL, Albert. Energy recovery in membrane capacitive deionization. **Environmental Science and Technology**, *[S. l.]*, v. 47, n. 9, p. 4904–4910, 2013. DOI: 10.1021/es3053202.

DOADRIO, Antonio L.; SÁNCHEZ-MONTERO, José M.; DOADRIO, Juan C.; SALINAS, Antonio J.; VALLET-REGÍ, María. A molecular model to explain the controlled release from SBA-15 functionalized with APTES. **Microporous and Mesoporous Materials**, *[S. l.]*, v. 195, p. 43–49, 2014. DOI: 10.1016/j.micromeso.2014.04.019.

DUAN, Feng; DU, Xuan; LI, Yuping; CAO, Hongbin; ZHANG, Yi. Desalination stability of capacitive deionization using ordered mesoporous carbon: Effect of oxygen-containing surface groups and pore properties. **Desalination**, *[S. l.]*, v. 376, n. 1, p. 17–24, 2015. a. DOI: 10.1016/j.desal.2015.08.009.

DUAN, Feng; LI, Yuping; CAO, Hongbin; WANG, Yi; CRITTENDEN, John C.; ZHANG, Yi. Activated carbon electrodes: Electrochemical oxidation coupled with desalination for wastewater treatment. **Chemosphere**, *[S. l.]*, v. 125, p. 205–211, 2015. b.

DUBEY, Ashutosh; BHAVSAR, Nidhi; PACHCHIGAR, Vivek; SAINI, Mahesh; RANJAN, Mukesh; LATA, Charu. Microwave assisted ultrafast synthesis of graphene oxide

based magnetic nano composite for environmental remediation. **Ceramics International**, *[S. l.]*, v. 48, n. 4, p. 4821–4828, 2022. DOI: 10.1016/j.ceramint.2021.11.018.

DUTTA, Saikat; HUANG, Shu Yun; CHEN, Cephas; CHEN, Jeffrey E.; ALOTHMAN, Zeid A.; YAMAUCHI, Yusuke; HOU, Chia Hung; WU, Kevin C. W. Cellulose Framework Directed Construction of Hierarchically Porous Carbons Offering High-Performance Capacitive Deionization of Brackish Water. **ACS Sustainable Chemistry and Engineering**, *[S. l.]*, v. 4, n. 4, p. 1885–1893, 2016. DOI: 10.1021/ acssuschemeng.5b01587.

DYKSTRA, J. E.; PORADA, S.; VAN DER WAL, A.; BIESHEUVEL, P. M. Energy consumption in capacitive deionization – Constant current versus constant voltage operation. **Water Research**, *[S. l.]*, v. 143, p. 367–375, 2018.

ELSAID, Khaled; KAMIL, Mohammed; SAYED, Enas Taha; ABDELKAREEM, Mohammad Ali; WILBERFORCE, Tabbi; OLABI, A. Environmental impact of desalination technologies: A review. **Science of the Total Environment**, *[S. l.]*, v. 748, 2020.

FARMER, J. C.; FIX, D. V.; MACK, G. V.; PEKALA, R. W.; POCO, J. F. The Use of Capacitive Deionization with Carbon Aerogel Electrodes to Remove Inorganic Contaminants from Water, internal document, Lawrence Livermore National Laboratory. *Em*: LOW LEVEL WASTE CONFERENCE 1995, Orlando. **Anais** [...]. Orlando

FENG, Xiaofang; LONG, Runxuan; WANG, Lingling; LIU, Chenchen; BAI, Zhongxiang; LIU, Xiaobo. A review on heavy metal ions adsorption from water by layered double hydroxide and its composites. **Separation and Purification Technology**, *[S. l.]*, v. 284, n. November 2021, p. 120099, 2022. DOI: 10.1016/j.seppur.2021.120099. Disponível em: https://doi.org/10.1016/j.seppur.2021.120099.

FLEUTOT, S. et al. Spacing-Dependent Dipolar Interactions in Dendronized Magnetic Iron Oxide Nanoparticle 2D Arrays and Powders. **Nanoscale**, *[S. l.]*, v. 5, p. 1507–1516, 2013. DOI: 10.1039/c2nr32117c.

FREIRE, T. M. et al. Fast ultrasound assisted synthesis of chitosan-based magnetite nanocomposites as a modified electrode sensor. **Carbohydrate Polymers**, *[S. l.]*, v. 151, p. 760–769, 2016. DOI: 10.1016/j.carbpol.2016.05.095.

FREIRE, Tiago M. et al. Magnetic Porous Controlled Fe3O4 – Chitosan Nanostructure: An Ecofriendly Adsorbent for Efficient Removal of Azo Dyes. **Nanomaterials**, *[S. l.]*, v. 10, n. 1194, p. 1–25, 2020.

FREUNDLICH, Herbert. Über die Adsorption in Lösungen. **Zeitschrift für Physikalische Chemie**, *[S. l.]*, v. 57U, n. 1, p. 385–470, 1907. DOI: 10.1515/zpch-1907-5723.

GAO, Xin; OMOSEBI, Ayokunle; LANDON, James; LIU, Kunlei. Enhancement of charge efficiency for a capacitive deionization cell using carbon xerogel with modified potential of

zero charge. **Electrochemistry Communications**, *[S. l.]*, v. 39, p. 22–25, 2014. DOI: 10.1016/j.elecom.2013.12.004.

GARCÍA-QUISMONDO, Enrique; GÓMEZ, Roberto; VAQUERO, Fernando; CUDERO, Ana López; PALMA, Jesús; ANDERSON, Marc. New testing procedures of a capacitive deionization reactor. **Physical Chemistry Chemical Physics**, *[S. l.]*, v. 15, n. 20, p. 7648–7656, 2013. a.

GARCÍA-QUISMONDO, Enrique; SANTOS, Cleis; LADO, Julio; PALMA, Jesús; ANDERSON, Marc A. Optimizing the energy efficiency of capacitive deionization reactors working under real-world conditions. **Environmental Science and Technology**, *[S. l.]*, v. 47, n. 20, p. 11866–11872, 2013. b. DOI: https://doi.org/10.1021/es4021603.

GU, Dungang; FEIN, Jeremy B. Adsorption of metals onto graphene oxide: Surface complexation modeling and linear free energy relationships. **Colloids and Surfaces A: Physicochemical and Engineering Aspects**, *[S. l.]*, v. 481, p. 319–327, 2015. DOI: 10.1016/j.colsurfa.2015.05.026.

GUO, Lu et al. High speed capacitive deionization system with flow-through electrodes. **Desalination**, *[S. l.]*, v. 496, n. September, p. 114750, 2020. DOI: 10.1016/j.desal.2020.114750.

GUO, Yongfu; DENG, Juan; ZHU, Junyan; ZHOU, Xiaoji; BAI, Renbi. Removal of mercury(II) and methylene blue from a wastewater environment with magnetic graphene oxide: Adsorption kinetics, isotherms and mechanism. **RSC Advances**, *[S. l.]*, v. 6, n. 86, p. 82523–82536, 2016. DOI: 10.1039/c6ra14651a.

GUYES, Eric N.; MALKA, Tahel; SUSS, Matthew E. Enhancing the ion-size-based selectivity of capacitive deionization electrodes. **Environmental Science and Technology**, *[S. l.]*, v. 53, n. 14, p. 8447–8454, 2019. DOI: 10.1021/acs.est.8b06954.

HAN, Linchen; KARTHIKEYAN, K. G.; ANDERSON, M. A.; WOUTERS, J. J.; GREGORY, Kelvin B. Mechanistic insights into the use of oxide nanoparticles coated asymmetric electrodes for capacitive deionization. **Electrochimica Acta**, *[S. l.]*, v. 90, p. 573–581, 2013. DOI: 10.1016/j.electacta.2012.11.069.

HAN, Linchen; KARTHIKEYAN, K. G.; GREGORY, Kelvin B. Energy Consumption and Recovery in Capacitive Deionization Using Nanoporous Activated Carbon Electrodes. **Journal of The Electrochemical Society**, *[S. l.]*, v. 162, n. 12, p. E282–E288, 2015. DOI: 10.1149/2.0431512jes.

HARIPRIYAN, U.; GOPINATH, K. P.; ARUN, J. Chitosan based nano adsorbents and its types for heavy metal removal: A mini review. **Materials Letters**, *[S. l.]*, v. 312, n. November 2021, p. 131670, 2022. DOI: 10.1016/j.matlet.2022.131670.

HASAN, Hassimi Abu; MUHAMMAD, Mohd Hafizuddin; ISMAIL, Nur Izzati. A review of biological drinking water treatment technologies for contaminants removal from polluted

water resources. **Journal of Water Process Engineering**, *[S. l.]*, v. 33, n. May 2019, p. 101035, 2020. DOI: 10.1016/j.jwpe.2019.101035.

HASSANVAND, A.; CHEN, G. Q.; WEBLEY, P. A.; KENTISH, S. E. An investigation of the impact of fouling agents in capacitive and membrane capacitive deionisation. **Desalination**, *[S. l.]*, v. 457, n. November 2018, p. 96–102, 2019. DOI: 10.1016/j.desal.2019.01.031.

HAWKS, Steven A.; KNIPE, Jennifer M.; CAMPBELL, Patrick G.; LOEB, Colin K.; HUBERT, McKenzie A.; SANTIAGO, Juan G.; STADERMANN, Michael. Quantifying the flow efficiency in constant-current capacitive deionization. **Water Research**, *[S. l.]*, v. 129, p. 327–336, 2018. DOI: 10.1016/j.watres.2017.11.025.

HAWKS, Steven A.; RAMACHANDRAN, Ashwin; PORADA, Slawomir; CAMPBELL, Patrick G.; SUSS, Matthew E.; BIESHEUVEL, P. M.; SANTIAGO, Juan G.; STADERMANN, Michael. Performance metrics for the objective assessment of capacitive deionization systems. **Water Research**, *[S. l.]*, v. 152, p. 126–137, 2019. DOI: 10.1016/j.watres.2018.10.074.

HE, Di; WONG, Chi Eng; TANG, Wangwang; KOVALSKY, Peter; WAITE, T. David. Faradaic Reactions in Water Desalination by Batch-Mode Capacitive Deionization. **Environmental Science & Technology Letters**, *[S. l.]*, v. 3, p. 222–226, 2016. DOI: 10.1021/acs.estlett.6b00124.

HEMMATIFAR, Ali; PALKO, James W.; STADERMANN, Michael; SANTIAGO, Juan G. Energy breakdown in capacitive deionization. **Water Research**, *[S. l.]*, v. 104, p. 303–311, 2016. DOI: 10.1016/j.watres.2016.08.020.

HO, Y. S.; MCKAY, G. Pseudo-second order model for sorption processes. **Process Biochemistry**, *[S. l.]*, v. 34, p. 451–465, 1999.

HOANG, Anh Tuan; KUMAR, Sunil; LICHTFOUSE, Eric; CHENG, Chin Kui; VARMA, Rajender S.; SENTHILKUMAR, N.; NGUYEN, Phuoc Quy Phong; NGUYEN, Xuan Phuong. Remediation of heavy metal polluted waters using activated carbon from lignocellulosic biomass: An update of recent trends. **Chemosphere**, *[S. l.]*, v. 302, n. May, p. 134825, 2022. DOI: 10.1016/j.chemosphere.2022.134825.

HONG, Mei; YU, Lingyun; WANG, Yanding; ZHANG, Jian; CHEN, Zhuwen; DONG, Lei; ZAN, Qijie; LI, Ruili. Heavy metal adsorption with zeolites: The role of hierarchical pore architecture. **Chemical Engineering Journal**, *[S. l.]*, v. 359, n. November 2018, p. 363–372, 2019. DOI: 10.1016/j.cej.2018.11.087. Disponível em: https://doi.org/10.1016/j.cej.2018.11.087.

HUMMERS, William S.; OFFEMAN, Richard E. Preparation of Graphitic Oxide. **Journal of the American Chemical Society**, *[S. l.]*, v. 80, n. 6, p. 1339, 1958. DOI: 10.1021/ja01539a017.

HUONG LE, Thi Xuan; BECHELANY, Mikhael; CRETIN, Marc. Carbon felt based-electrodes for energy and environmental applications: A review. **Carbon**, *[S. l.]*, v. 122, p. 564–591, 2017. DOI: 10.1016/j.carbon.2017.06.078.

ISLAM, Aminul; AHMAD, Hilal; ZAIDI, Noushi; KUMAR, Suneel. Graphene oxide sheets immobilized polystyrene for column preconcentration and sensitive determination of lead by flame atomic absorption spectrometry. **ACS Applied Materials and Interfaces**, *[S. l.]*, v. 6, n. 15, p. 13257–13265, 2014. DOI: 10.1021/am5031215.

JAIN, Chakresh Kumar; MALIK, Davendra Singh. Applicability of plant based biosorbents in the removal of heavy metals: a review. **Environmental Processes**, *[S. l.]*, v. 3, p. 495–523, 2016. DOI: 10.1007/s40710-016-0143-5.

JIA, Baoping; ZHANG, Wei. Preparation and Application of Electrodes in Capacitive Deionization (CDI): a State-of-Art Review. **Nanoscale Research Letters**, *[S. l.]*, v. 11, n. 1, p. 1–25, 2016. DOI: 10.1186/s11671-016-1284-1.

JIA, Fan; LI, Zhiping. Iron-catalyzed/mediated oxidative transformation of C-H bonds. **Organic Chemistry Frontiers**, *[S. l.]*, v. 1, n. 2, p. 194–214, 2014. DOI: 10.1039/c3qo00087g.

JIANG, Xingguo; LIU, Jinxian; MA, Shengming. Iron-Catalyzed Aerobic Oxidation of Alcohols: Lower Cost and Improved Selectivity. **Organic Process Research and Development**, *[S. l.]*, v. 23, n. 5, p. 825–835, 2019. DOI: 10.1021/acs.oprd.8b00374.

JOHNSON, A. M.; NEWMAN, John. Desalting by Means of Porous Carbon Electrodes. **Journal of the Electrochemical Society**, *[S. l.]*, v. 118, n. 3, p. 510–517, 1971. DOI: 10.1149/1.2408094.

JOHNSON, Allan M.; VENOLIA, A. Wayne; WILBOURNE, Robert G.; NEWMAN, John. **The Electrosorb Process for Desalting Water**. [s.l: s.n.].

JUCHEN, Patricia T.; BARCELOS, Kamilla M.; OLIVEIRA, Kaíque S. G. C.; RUOTOLO, Luís A. M. Using crude residual glycerol as precursor of sustainable activated carbon electrodes for capacitive deionization desalination. **Chemical Engineering Journal**, *[S. l.]*, v. 429, n. July 2021, p. 132209, 2022. DOI: 10.1016/j.cej.2021.132209. Disponível em: https://doi.org/10.1016/j.cej.2021.132209.

KALFA, Ayelet; SHAPIRA, Barak; SHOPIN, Alexey; COHEN, Izaak; AVRAHAM, Eran; AURBACH, Doron. Capacitive deionization for wastewater treatment: Opportunities and challenges. **Chemosphere**, *[S. l.]*, v. 241, n. 125003, 2020.

KANG, Jong Hun et al. Hidden Second Oxidation Step of Hummers Method. **Chemistry of Materials**, *[S. l.]*, v. 28, p. 756–764, 2016. a. DOI: 10.1021/acs.chemmater.5b03700.

KANG, Junil; KIM, Taeyoung; JO, Kyusik; YOON, Jeyong. Comparison of salt adsorption capacity and energy consumption between constant current and constant voltage operation in capacitive deionization. **Desalination**, *[S. l.]*, v. 352, p. 52–57, 2014.

KANG, Junil; KIM, Taeyoung; SHIN, Hojoon; LEE, Jiho; HA, Jung-ik; YOON, Jeyong. Direct energy recovery system for membrane capacitive deionization. **Desa**, *[S. l.]*, v. 398, p. 144–150, 2016. b. DOI: 10.1016/j.desal.2016.07.025.

KARADE, V. C. et al. APTES monolayer coverage on self-assembled magnetic nanospheres for controlled release of anticancer drug Nintedanib. **Scientific Reports**, *[S. l.]*, v. 11, n. 1, p. 5674, 2021. DOI: 10.1038/s41598-021-84770-0.

KAUR, Navneet; KAUR, Manpreet; SINGH, Dhanwinder. Fabrication of mesoporous nanocomposite of graphene oxide with magnesium ferrite for efficient sequestration of Ni (II) and Pb (II) ions: Adsorption, thermodynamic and kinetic studies. **Environmental Pollution**, *[S. l.]*, v. 253, p. 111–119, 2019. DOI: 10.1016/j.envpol.2019.05.145.

KEERTHANA, D. Shanthini; NAMRATHA, K.; BYRAPPA, K.; YATHIRAJAN, H. S. Facile one-step fabrication of magnetite particles under mild hydrothermal conditions. **Journal of Magnetism and Magnetic Materials**, *[S. l.]*, v. 378, p. 551–557, 2015. DOI: 10.1016/j.jmmm.2014.10.176. Disponível em: http://dx.doi.org/10.1016/j.jmmm.2014.10.176.

KIM, Choonsoo; SRIMUK, Pattarachai; LEE, Juhan; FLEISCHMANN, Simon; ASLAN, Mesut; PRESSER, Volker. Influence of pore structure and cell voltage of activated carbon cloth as a versatile electrode material for capacitive deionization. **Carbon**, *[S. l.]*, v. 122, p. 329–335, 2017. DOI: 10.1016/j.carbon.2017.06.077.

KIM, T.; DYKSTRA, J. E.; PORADA, S.; VAN DER WAL, A.; YOON, J.; BIESHEUVEL, P. M. Enhanced charge efficiency and reduced energy use in capacitive deionization by increasing the discharge voltage. **Journal of Colloid and Interface Science**, *[S. l.]*, v. 446, p. 317–326, 2015.

KIM, Taeyoung; YOO, Hyun Deog; OH, Seung M.; YOON, Jeyong. Potential sweep method to evaluate rate capability in capacitive deionization. **Electrochimica Acta**, *[S. l.]*, v. 139, p. 374–380, 2014. DOI: 10.1016/j.electacta.2014.07.034.

KOHLMEYER, Ryan R.; BLAKE, Aaron J.; HARDIN, James O.; CARMONA, Eric A.; CARPENA-NÚÑEZ, Jennifer; MARUYAMA, Benji; DANIEL BERRIGAN, J.; HUANG, Hong; DURSTOCK, Michael F. Composite batteries: A simple yet universal approach to 3D printable lithium-ion battery electrodes. **Journal of Materials Chemistry A**, *[S. l.]*, v. 4, n. 43, p. 16856–16864, 2016. DOI: 10.1039/c6ta07610f.

KOLEN'KO, Yury V et al. Large-Scale Synthesis of Colloidal Fe3O4 Nanoparticles Exhibiting High Heating Efficiency in Magnetic Hyperthermia. **The Journal of Physical Chemistry C**, *[S. l.]*, v. 118, p. 8691–8701, 2014.

KONG, Qiaoping; SHI, Xueqing; MA, Weiwei; ZHANG, Fengzhen; YU, Tong; ZHAO, Fei; ZHAO, Dandan; WEI, Chaohai. Strategies to improve the adsorption properties of graphene-based adsorbent towards heavy metal ions and their compound pollutants : A review. **Journal of Hazardous Materials**, *[S. l.]*, v. 415, n. February, p. 125690, 2021. DOI: 10.1016/j.jhazmat.2021.125690. Disponível em: https://doi.org/10.1016/j.jhazmat.2021.125690.

KUMAR, Suneel; ISLAM, Aminul; AHMAD, Hilal; ZAIDI, Noushi. Graphene Oxide Supported on Amberlite Resin for the Analytical Method Development for Enhanced Column Preconcentration/Sensitive Flame Atomic Absorption Spectrometric Determination of Toxic Metal Ions in Environmental Samples. **Industrial and Engineering Chemistry Research**, *[S. l.]*, v. 58, n. 19, p. 8309–8316, 2019. DOI: 10.1021/acs.iecr.9b00576.

KUO, Helen A.; RAMACHANDRAN, Ashwin; OYARZUN, Diego I.; CLEVENGER, Erica C.; SANTIAGO, Juan G.; STADERMANN, Michael; CAMPBELL, Patrick G.; HAWKS, Steven A. Understanding resistances in capacitive deionization devices. **Environmental Science: Water Research Technology**, *[S. l.]*, v. 6, p. 1842–1854, 2020. DOI: 10.1039/D0EW00169D.

LADO, Julio J.; CARTOLANO, Vincenzo; GARCÍA-QUISMONDO, Enrique; GARCÍA, Guzmán; ALMONACID, Ignacio; SENATORE, Vincenzo; NADDEO, Vincenzo; PALMA, Jesús; ANDERSON, Marc A. Performance analysis of a capacitive deionization stack for brackish water desalination. **Desalination**, *[S. l.]*, v. 501, p. 114912, 2021. a. DOI: 10.1016/j.desal.2020.114912.

LADO, Julio J.; CARTOLANO, Vincenzo; GARCÍA-QUISMONDO, Enrique; GARCÍA, Guzmán; ALMONACID, Ignacio; SENATORE, Vincenzo; NADDEO, Vincenzo; PALMA, Jesús; ANDERSON, Marc A. Performance analysis of a capacitive deionization stack for brackish water desalination. **Desalination**, *[S. l.]*, v. 501, p. 114912, 2021. b. DOI: 10.1016/j.desal.2020.114912.

LADO, Julio J.; PÉREZ-ROA, Rodolfo E.; WOUTERS, Jesse J.; TEJEDOR-TEJEDOR, M. Isabel; FEDERSPILL, Cade; ANDERSON, Marc A. Continuous cycling of an asymmetric capacitive deionization system: An evaluation of the electrode performance and stability. **Journal of Environmental Chemical Engineering**, *[S. l.]*, v. 3, n. 4, p. 2358–2367, 2015. DOI: 10.1016/j.jece.2015.08.025.

LADO, Julio J.; ZORNITTA, Rafael L.; VÁZQUEZ RODRÍGUEZ, Inés; MALVERDI BARCELOS, Kamila; RUOTOLO, Luís A. M. Sugarcane Biowaste-Derived Biochars as Capacitive Deionization Electrodes for Brackish Water Desalination and Water-Softening Applications. **ACS Sustainable Chemistry and Engineering**, *[S. l.]*, v. 7, n. 23, p. 18992–19004, 2019. a. DOI: 10.1021/acssuschemeng.9b04504.

LADO, Julio J.; ZORNITTA, Rafael L.; VÁZQUEZ RODRÍGUEZ, Inés; MALVERDI BARCELOS, Kamila; RUOTOLO, Luís A. M. Sugarcane Biowaste-Derived Biochars as Capacitive Deionization Electrodes for Brackish Water Desalination and Water-Softening Applications. **ACS Sustainable Chemistry and Engineering**, *[S. l.]*, v. 7, n. 23, p. 18992–19004, 2019. b. DOI: 10.1021/acssuschemeng.9b04504.

LANGMUIR, I. The adsorption of gases on plane surfaces of glass, mica and platinum. **Journal of the American Chemical Society**, *[S. l.]*, v. 40, n. 1914, p. 1361–1403, 1918.

LEE, Bin; PARK, Namsoo; KANG, Kyung Suk; RYU, Ho Jin; HONG, Soon Hyung. Enhanced Capacitive Deionization by Dispersion of CNTs in Activated Carbon Electrode. **ACS Sustainable Chemistry and Engineering**, *[S. l.]*, v. 6, n. 2, p. 1572–1579, 2018. DOI: 10.1021/acssuschemeng.7b01750.

LEE, Jinhyeong; PARK, Jeong-ann; KIM, Hee-gon; LEE, Jung-hyun; CHO, So-hye; CHOI, Keunsu; JUNG, Kyung-won; YONG, Seung; CHOI, Jae-Woo. Most suitable amino silane molecules for surface functionalization of graphene oxide toward hexavalent chromium adsorption. **Chemosphere**, *[S. l.]*, v. 251, p. 126387, 2020. DOI: 10.1016/j.chemosphere.2020.126387. Disponível em: https://doi.org/10.1016/j.chemosphere.2020.126387.

LEE, Joo Hyung; KIM, Seong Jun. Fabrication of silane-grafted graphene oxide and its effect on the structural, thermal, mechanical, and hysteretic behavior of polyurethane. **Scientific Reports**, *[S. l.]*, v. 10, p. 19152, 2020.

LEONG, Zhi Yi; ZHANG, Jintao; VAFAKHAH, Sareh; DING, Meng; GUO, Lu; YANG, Hui Ying. Electrochemically activated layered manganese oxide for selective removal of calcium and magnesium ions in hybrid capacitive deionization. **Desalination**, *[S. l.]*, v. 520, n. July, p. 115374, 2021. DOI: 10.1016/j.desal.2021.115374.

LESTER, Yaal; SHAULSKY, Evyatar; EPSZTEIN, Razi; ZUCKER, Ines. Capacitive deionization for simultaneous removal of salt and uncharged organic contaminants from water. **Separation and Purification Technology**, *[S. l.]*, v. 237, n. November 2019, p. 116388, 2020. DOI: 10.1016/j.seppur.2019.116388.

LI, Haibo; LIANG, Sen; GAO, Mangmang; LI, Guolong; LI, Jin; HE, Lijun. The study of capacitive deionization behavior of a carbon nanotube electrode from the perspective of charge efficiency. **Water Science and Technology**, *[S. l.]*, v. 71, n. 1, p. 83–88, 2015. DOI: 10.2166/wst.2014.457.

LI, Jing; JI, Bingxue; JIANG, Rui; ZHANG, Panpan; CHEN, Nan; ZHANG, Guofeng; QU, Liangti. Hierarchical hole-enhanced 3D graphene assembly for highly efficient capacitive deionization. **Carbon**, *[S. l.]*, v. 129, p. 95–103, 2018. a. DOI: 10.1016/j.carbon.2017.11.095.

LI, Lixia; ZOU, Linda; SONG, Huaihe; MORRIS, Gayle. Ordered mesoporous carbons synthesized by a modified sol-gel process for electrosorptive removal of sodium chloride. **Carbon**, *[S. l.]*, v. 47, n. 3, p. 775–781, 2009. DOI: 10.1016/j.carbon.2008.11.012.

LI, Longxin; SUN, Fei; GAO, Jihui; WANG, Lijie; PI, Xinxin; ZHAO, Guangbo. Broadening the pore size of coal-based activated carbon via a washing-free chem-physical activation method for high-capacity dye adsorption. **RSC Advances**, *[S. l.]*, v. 8, p. 14488–14499, 2018. b. DOI: 10.1039/c8ra02127a.

LI, Shijie; TAN, Xiaopeng; LI, Hui; GAO, Yan; WANG, Qian; LI, Guoning; GUO, Min. Investigation on pore structure regulation of activated carbon derived from sargassum and its application in supercapacitor. **Scientific Reports**, *[S. l.]*, v. 12, n. 10106, p. 1–17, 2022. a. DOI: 10.1038/s41598-022-14214-w. Disponível em: https://doi.org/10.1038/s41598-022-14214-w.

LI, Wenyuan; ZHANG, Chenyang; WEI, Xin; ZHANG, Hongliang; HAN, Mingjun; SUN, Wei. Efficient resource treatment of hexavalent chromium wastewater based on lead carbonate (cerussite)-induced precipitation separation. **Process Safety and Environmental Protection**, *[S. l.]*, v. 165, n. May, p. 475–486, 2022. b. DOI: 10.1016/j.psep.2022.07.039. Disponível em: https://doi.org/10.1016/j.psep.2022.07.039.

LIU, Chong et al. Direct/Alternating Current Electrochemical Method for Removing and Recovering Heavy Metal from Water Using Graphene Oxide Electrode. **ACS Nano**, *[S. l.]*, v. 13, p. 6431–6437, 2019. DOI: 10.1021/acsnano.8b09301.

LIU, Cuiyun; LIU, Hongyu; XU, Airong; TANG, Keyong; HUANG, Yu; LU, Chang. In situ reduced and assembled three-dimensionl graphene aerogel for efficient dy removal. **Journal of Alloys and Compounds**, *[S. l.]*, v. 714, p. 522–529, 2017. a.

LIU, Jun; DU, Hongyan; YUAN, Shaowei; HE, Wanxia; LIU, Zhanhong. Synthesis of thiol-functionalized magnetic graphene as adsorbent for Cd(II) removal from aqueous systems. **Journal of Environmental Chemical Engineering**, *[S. l.]*, v. 3, n. 2, p. 617–621, 2015. a. DOI: 10.1016/j.jece.2015.01.016.

LIU, Xilong et al. Experimental and theoretical studies of nonlinear dependence of the internal resistance and electrode thickness for high performance supercapacitor. **Scientific Reports**, *[S. l.]*, v. 7, n. March, p. 1–8, 2017. b. DOI: 10.1038/srep45934.

LIU, Xitong; SHANBHAG, Sneha; BARTHOLOMEW, Timothy V; WHITACRE, Jay F.; MAUTER, Meagan S. Cost Comparison of Capacitive Deionization and Reverse Osmosis for Brackish Water Desalination. **Environmental Science & Technology - Engineering**, *[S. l.]*, v. 1, p. 261–273, 2021. DOI: 10.1021/acsestengg.0c00094.

LIU, Yong; NIE, Chunyang; LIU, Xinjuan; XU, Xingtao; SUN, Zhuo; PAN, Likun. Review on carbon-based composite materials for capacitive deionization. **RSC Advances**, *[S. l.]*, v. 5, n. 20, p. 15205–15225, 2015. b. DOI: 10.1039/C4RA14447C.

LIU, Yong; PAN, Likun; XU, Xingtao; LU, Ting; SUN, Zhuo; CHUA, Daniel H. C. Enhanced desalination efficiency in modified membrane capacitive deionization by introducing ion-exchange polymers in carbon nanotubes electrodes. **Electrochimica Acta**, *[S. l.]*, v. 130, p. 619–624, 2014. DOI: 10.1016/j.electacta.2014.03.086.

LUO, Wenbin; ZHENG, Baolin; HE, Jie. Enhanced electrochemical performance of LiNi0.5Co0.2Mn0.3O2 cathode material after surface modification with graphene oxide. **Journal of Alloys and Compounds**, *[S. l.]*, v. 705, p. 405–412, 2017. DOI: 10.1016/j.jallcom.2017.02.114.

MAHESH, Narayanan; BALAKUMAR, Srinivasan; SHYAMALAGOWRI, Shanmugasundaram; MANJUNATHAN, Jagadeesan; PAVITHRA, M. K. S.; SURESH, Palanisamy; KAMARAJ, Murugesan; GOVARTHANAN, Muthusamy. Carbon-based adsorbents as proficient tools for the removal of heavy metals from aqueous solution: A state of art-review emphasizing recent progress and prospects. **Environmental Research**, *[S. l.]*, v. 213, n. May, p. 113723, 2022. DOI: 10.1016/j.envres.2022.113723. Disponível em: https://doi.org/10.1016/j.envres.2022.113723.

MENDOZA-CASTILLO, Didilia Ileana; REYNEL-A, Hilda Elizabeth. Introduction. *Em*: BONILLA-PETRICIOLET, Adrián; MENDOZA-CASTILLO, Didilia Ileana; REYNEL-ÁVILA, Hilda Elizabeth (org.). **Adsorption Processes for Water Treatment and Purification**. 1. ed. [s.l.] : Springer Cham, 2017. p. 1–18. DOI: 10.1007/978-3-319-58136-1.

MIESSLER, Gary L.; FISCHER, Paul J.; TARR, Donald A. **Inorganic Chemistry**. Fifth ed. [s.l: s.n.].

MOSSAD, Mohamed; ZOU, Linda. Study of fouling and scaling in capacitive deionisation by using dissolved organic and inorganic salts. **Journal of Hazardous Materials**, *[S. l.]*, v. 244–245, p. 387–393, 2013. a. DOI: 10.1016/j.jhazmat.2012.11.062.

MOSSAD, Mohamed; ZOU, Linda. Evaluation of the salt removal efficiency of capacitive deionisation: Kinetics, isotherms and thermodynamics. **Chemical Engineering Journal**, *[S. l.]*, v. 223, p. 704–713, 2013. b. DOI: 10.1016/j.cej.2013.03.058.

MURPHY, G. W.; CAUDLE, D. D. Mathematical theory of electrochemical demineralization in flowing systems. **Electrochimica Acta**, *[S. l.]*, v. 12, n. 12, p. 1655–1664, 1967. DOI: 10.1016/0013-4686(67)80079-3.

MURPHY, G. W.; TUCKER, J. H.; CAUDLE, D.; HOCK, R. **Electrochemical demineralization of water with carbon electrodesResearch and Development Progress Report**. [s.l: s.n.].

NETO, Davino M. A. et al. Rapid Sonochemical Approach Produces Functionalized Fe3O4 Nanoparticles with Excellent Magnetic, Colloidal, and Relaxivity Properties for MRI Application. **The Journal of Physical Chemistry C**, *[S. l.]*, v. 121, p. 24206–24222, 2017. DOI: 10.1021/acs.jpcc.7b04941.

OLIVEIRA, Alexandra M. L.; MACHADO, M.; SILVA, Gabriela A.; BITOQUE, Diogo B.; FERREIRA, Joana Tavares; FERREIRA, Quirina. Graphene Oxide Thin Films with Drug Delivery Function. **Graphene oxide thin films with drug delivery function**, *[S. l.]*, v. 12, n. 1149, p. 1–20, 2022.

OREN, Yoram. Capacitive deionization (CDI) for desalination and water treatment - past, present and future (a review). **Desalination**, *[S. l.]*, v. 228, n. 1–3, p. 10–29, 2008. DOI: 10.1016/j.desal.2007.08.005.

OUYANG, Tian et al. High-throughput fabrication of porous carbon by chemical foaming strategy for high performance supercapacitor. **Chemical Engineering Journal**, *[S. l.]*, v. 352, n. June, p. 459–468, 2018. a. DOI: 10.1016/j.cej.2018.06.184.

OUYANG, Tian et al. **High-throughput fabrication of porous carbon by chemical foaming strategy for high performance supercapacitor**. **Chemical Engineering Journal**, 2018. b. DOI: 10.1016/j.cej.2018.06.184.

OYARZUN, Diego I.; HAWKS, Steve A.; CAMPBELL, Patrick G.; HEMMATIFAR, Ali; KRISHNA, Ashish; SANTIAGO, Juan G.; STADERMANN, Michael. Energy transfer for storage or recovery in capacitive deionization using a DC-DC converter. **Journal of Power Sources**, *[S. l.]*, v. 448, n. 227409, 2020. DOI: 10.1016/j.jpowsour.2019.227409.

PARK, Se Kook; SHIM, Joonmok; YANG, Jung Hoon; JIN, Chang Soo; LEE, Bum Suk; LEE, Young Seak; SHIN, Kyoung Hee; JEON, Jae Deok. The influence of compressed carbon felt electrodes on the performance of a vanadium redox flow battery. **Electrochimica Acta**, *[S. l.]*, v. 116, p. 447–452, 2014. DOI: 10.1016/j.electacta.2013.11.073.

PAULY, Matthias; PICHON, Benoit P.; PANISSOD, Pierre; FLEUTOT, Solenne; RODRIGUEZ, Pedro; DRILLON, Marc; BEGIN-COLIN, Sylvie. Size dependent dipolar interactions in iron oxide nanoparticle monolayer and multilayer Langmuir-Blodgett films. **Journal of Materials Chemistry**, *[S. l.]*, v. 22, n. 13, p. 6343–6350, 2012. DOI: 10.1039/c2jm15797g.

PENG, Weijun; LI, Hongqiang; LIU, Yanyan; SONG, Shaoxian. A review on heavy metal ions adsorption from water by graphene oxide and its composites. **Journal of Molecular Liquids**, *[S. l.]*, v. 230, p. 496–504, 2017. DOI: 10.1016/j.molliq.2017.01.064.

PIRVEYSIAN, Mahtab; GHIACI, Mehran. Synthesis and characterization of sulfur functionalized graphene oxide nanosheets as efficient sorbent for removal of Pb2+, Cd2+, Ni2+ and Zn2+ ions from aqueous solution: A combined thermodynamic and kinetic studies. **Applied Surface Science**, *[S. l.]*, v. 428, p. 98–109, 2018. DOI: 10.1016/j.apsusc.2017.09.105.

PORADA, S.; ZHAO, R.; VAN DER WAL, A.; PRESSER, V.; BIESHEUVEL, P. M. Review on the science and technology of water desalination by capacitive deionization. **Progress in Materials Science**, *[S. l.]*, v. 58, n. 8, p. 1388–1442, 2013. DOI: 10.1016/j.pmatsci.2013.03.005.

QU, Yatian; BAUMANN, Theodore F.; SANTIAGO, Juan G.; STADERMANN, Michael. Characterization of Resistances of a Capacitive Deionization System. **Environmental Science and Technology**, *[S. l.]*, v. 49, p. 9699–9706, 2015. DOI: 10.1021/acs.est.5b02542.

QU, Yatian; CAMPBELL, Patrick G.; GU, Lei; KNIPE, Jennifer M.; DZENITIS, Ella; SANTIAGO, Juan G.; STADERMANN, Michael. Energy consumption analysis of constant voltage and constant current operations in capacitive deionization. **Desalination**, *[S. l.]*, v. 400, p. 18–24, 2016.

RAD, Leila Roshanfekr; ANBIA, Mansoor. Zeolite-based composites for the adsorption of toxic matters from water: A review. **Journal of Environmental Chemical Engineering**, *[S. l.]*, v. 9, n. 5, p. 106088, 2021. DOI: 10.1016/j.jece.2021.106088. Disponível em: https://doi.org/10.1016/j.jece.2021.106088.

RAJAN, Arunima; SHARMA, Madhulika; SAHU, Niroj Kumar. Assessing magnetic and inductive thermal properties of various surfactants functionalised Fe3O4 nanoparticles for hyperthermia. **Scientific Reports**, *[S. l.]*, v. 10, n. 1, p. 1–15, 2020. DOI: 10.1038/s41598-020-71703-6.

REALE, Erik R.; SMITH, Kyle C. Capacitive Performance and Tortuosity of Activated Carbon Electrodes with Macroscopic Pores. **Journal of The Electrochemical Society**, *[S. l.]*, v. 165, n. 9, p. A1685–A1693, 2018. DOI: 10.1149/2.0601809jes.

REMILLARD, E. Marielle; SHOCRON, Amit N.; RAHILL, John; SUSS, Matthew E.; VECITIS, Chad D. A direct comparison of flow-by and flow-through capacitive deionization. *[S. l.]*, v. 444, n. January, p. 169–177, 2018. a. DOI: 10.1016/j.desal.2018.01.018.

REMILLARD, E. Marielle; SHOCRON, Amit N.; RAHILL, John; SUSS, Matthew E.; VECITIS, Chad D. A direct comparison of flow-by and flow-through capacitive deionization. *[S. l.]*, v. 444, n. January, p. 169–177, 2018. b. DOI: 10.1016/j.desal.2018.01.018.

RIZZO, Luigi et al. Consolidated vs new advanced treatment methods for the removal of contaminants of emerging concern from urban wastewater. **Science of the Total Environment**, *[S. l.]*, v. 655, n. October 2018, p. 986–1008, 2019. DOI: 10.1016/j.scitotenv.2018.11.265.

S., Lagergren. Zur Theorie der sogenannten Adsorption gelöster Stoffe. **Zeitschrift für Chemie und Industrie der Kolloide**, *[S. l.]*, v. 2, n. 15, 1907. DOI: https://doi.org/10.1007/BF01501332.

SANTOS, Cleis; GARCÍA-QUISMONDO, Enrique; PALMA, Jesús; ANDERSON, Marc A.; LADO, Julio J. Understanding capacitive deionization performance by comparing its electrical response with an electrochemical supercapacitor: Strategies to boost round-trip efficiency. **Electrochimica Acta**, *[S. l.]*, v. 330, p. 135216, 2020. DOI: 10.1016/j.electacta.2019.135216.

SANTOS, Cleis; LADO, Julio J.; GARCÍA-QUISMONDO, Enrique; SORIA, Jorge; PALMA, Jesús; ANDERSON, Marc A. Maximizing Volumetric Removal Capacity in Capacitive Deionization by Adjusting Electrode Thickness and Charging Mode. **Journal of the Electrochemical Society**, *[S. l.]*, v. 165, n. 7, p. E294–E302, 2018. DOI: 10.1149/2.1011807jes.

SEMIAT, Raphael. Energy issues in desalination processes. **Environmental Science and Technology**, *[S. l.]*, v. 42, n. 22, p. 8193–8201, 2008. DOI: 10.1021/es801330u.

SGL GROUP - THE CARBON COMPANY. **Specialty Graphites for Energy Storage**. , [s.d.].

SHARAN, Prashant; JUN, Tae; JAFFE, Stephen M.; JU, Taeho; CURRIER, Robert P.; FINDIKOGLU, Alp T. Can capacitive deionization outperform reverse osmosis for brackish water desalination ? **Cleaner Engineering and Technology**, *[S. l.]*, v. 3, p. 100102, 2021. DOI: 10.1016/j.clet.2021.100102.

SHERLALA, A. I. A.; RAMAN, A. A. A.; BELLO, M. M.; ASGHAR, A. A review of the applications of organo-functionalized magnetic graphene oxide nanocomposites for heavy metal adsorption. **Chemosphere**, *[S. l.]*, v. 193, p. 1004–1017, 2018. DOI: 10.1016/j.chemosphere.2017.11.093.

SHI, Wenhui; LI, Haibo; CAO, Xiehong; LEONG, Zhi Yi; ZHANG, Jun; CHEN, Tupei; ZHANG, Hua; YANG, Hui Ying. Ultrahigh Performance of Novel Capacitive Deionization Electrodes based on A Three-Dimensional Graphene Architecture with Nanopores. **Scientific Reports**, *[S. l.]*, v. 6, n. November 2015, p. 1–9, 2016. DOI: 10.1038/srep18966.

SHI, Wenhui; LIU, Xiaoyue; YE, Chenzeng; CAO, Xiehong; GAO, Congjie; SHEN, Jiangnan. Efficient lithium extraction by membrane capacitive deionization incorporated with monovalent selective cation exchange membrane. **Separation and Purification Technology**, *[S. l.]*, v. 210, n. July 2018, p. 885–890, 2019. DOI: 10.1016/j.seppur.2018.09.006.

SIONG, Wai; YING, Jie; KUMAR, P. Senthil; MUBASHIR, Muhammad; MAJEED, Zahid; BANAT, Fawzi; HO, Shih-hsin; LOKE, Pau. A review on conventional and novel materials towards heavy metal adsorption in wastewater treatment application. **Journal of Cleaner Production**, *[S. l.]*, v. 296, n. 126589, p. 1–12, 2021. DOI: 10.1016/j.jclepro.2021.126589.

SITKO, Rafal; JANIK, Paulina; FEIST, Barbara; TALIK, Ewa; GAGOR, Anna. Suspended aminosilanized graphene oxide nanosheets for selective preconcentration of lead ions and ultrasensitive determination by electrothermal atomic absorption spectrometry. **ACS Applied Materials and Interfaces**, *[S. l.]*, v. 6, n. 22, p. 20144–20153, 2014. DOI: 10.1021/am505740d.

SITKO, Rafal; MUSIELAK, Marcin; ZAWISZA, Beata; TALIK, Ewa; GAGOR, Anna. Graphene oxide/cellulose membranes in adsorption of divalent metal ions. **RSC Advances**, *[S. l.]*, v. 6, n. 99, p. 96595–96605, 2016. DOI: 10.1039/c6ra21432k.

SITKO, Rafal; TUREK, Edyta; ZAWISZA, Beata; MALICKA, Ewa; TALIK, Ewa; HEIMANN, Jan; GAGOR, Anna; FEIST, Barbara; WRZALIK, Roman. Adsorption of divalent metal ions from aqueous solutions using graphene oxide. **Dalton Transactions**, *[S. l.]*, v. 42, n. 16, p. 5682–5689, 2013. DOI: 10.1039/c3dt33097d.

SOARES, Ana. Wastewater treatment in 2050: Challenges ahead and future vision in a European context. **Environmental Science and Ecotechnology**, *[S. l.]*, v. 2, p. 10–13, 2020.

SOLIMAN, N. K.; MOUSTAFA, A. F. Industrial solid waste for heavy metals adsorption features and challenges; a review. **Integrative Medicine Research**, *[S. l.]*, v. 9, n. 5, p. 10235–10253, 2020. DOI: 10.1016/j.jmrt.2020.07.045. Disponível em: https://doi.org/10.1016/j.jmrt.2020.07.045.

SOYEKWO, Faizal; LIU, Changkun; ZHAO, Lihua; WEN, Hao; HUANG, Wei; CAI, Chaojie; KANAGARAJ, Palsamy; HU, Yunxia. Nanofiltration Membranes with Metal Cation-Immobilized Aminophosphonate Networks for E ffi cient Heavy Metal Ion Removal and Organic Dye Degradation. **ACS Applied Materials & Interfaces**, *[S. l.]*, v. 11, p. 30317–30331, 2019. DOI: 10.1021/acsami.9b10208.

STAUDENMAIER, L. Verfahren zur Darstellung der Graphitsäure. **Berichte der Deutschen Chemischen Gesellschaft**, *[S. l.]*, v. 31, p. 1481–1487, 1898.

STOIA, Marcela; ISTRATIE, Roxana; PA, Cornelia. Investigation of magnetite nanoparticles stability in air by thermal analysis and FTIR spectroscopy. **Journal of Thermal Analysis and Calorimetry**, *[S. l.]*, v. 125, n. 2, p. 1185–1198, 2016. DOI: 10.1007/s10973-016-5393-y.

SUBRAMANI, Arun; JACANGELO, Joseph G. Emerging desalination technologies for water treatment: A critical review. **Water Research**, *[S. l.]*, v. 75, p. 164–187, 2015. DOI: 10.1016/j.watres.2015.02.032.

SUMAN, Prateekshya; RAVI, Sahu; VERMA, Prakash; TEWARI, Chetna; GOPAL, Nanda; BISWAJIT, Sahoo. Environmental application of amine functionalised magnetite nanoparticles grafted graphene oxide chelants. **Environmental Science and Pollution Research**, *[S. l.]*, 2022. DOI: 10.1007/s11356-022-21407-3.

SUN, Hao; WANG, Han; WANG, He; YAN, Qun. Enhanced removal of heavy metals from electroplating wastewater through electrocoagulation using carboxymethyl chitosan as corrosion inhibitor for steel anode. **Environmental Science: Water Research & Technology**, *[S. l.]*, v. 4, p. 1105–1113, 2018. DOI: 10.1039/c8ew00322j.

SUN, Jieping; LIANG, Qionglin; HAN, Qiang; ZHANG, Xiaoqiong; DING, Mingyu. One-step synthesis of magnetic graphene oxide nanocomposite and its application in magnetic solid phase extraction of heavy metal ions from biological samples. **Talanta**, *[S. l.]*, v. 132, p. 557–563, 2015. DOI: 10.1016/j.talanta.2014.09.043. Disponível em: http://dx.doi.org/10.1016/j.talanta.2014.09.043.

SUN, Zhong-xi; SU, Fen-wei; FORSLING, Willis; SAMSKOG, Per-olof. Surface Characteristics of Magnetite in Aqueous Suspension. **Journal of Colloid and Interface Science**, *[S. l.]*, v. 159, n. 197, p. 151–159, 1998.

SUSS, M. E.; PORADA, S.; SUN, X.; BIESHEUVEL, P. M.; YOON, J.; PRESSER, V. Water desalination via capacitive deionization: What is it and what can we expect from it? **Energy and Environmental Science**, *[S. l.]*, v. 8, n. 8, p. 2296–2319, 2015. DOI: 10.1039/c5ee00519a.

SUSS, Matthew E. Size-Based Ion Selectivity of Micropore Electric Double Layers in Capacitive Deionization Electrodes. **Journal of The Electrochemical Society**, *[S. l.]*, v. 164, n. 9, p. E270–E275, 2017. DOI: 10.1149/2.1201709jes.

TAN, Ping; SUN, Jian; HU, Yongyou; FANG, Zheng; BI, Qi; CHEN, Yuancai; CHENG, Jianhua. Adsorption of Cu2+, Cd2+ and Ni2+ from aqueous single metal solutions on graphene oxide membranes. **Journal of Hazardous Materials**, *[S. l.]*, v. 297, p. 251–260, 2015. DOI: 10.1016/j.jhazmat.2015.04.068.

TANG, Wangwang; HE, Di; ZHANG, Changyong; KOVALSKY, Peter; WAITE, T. David. Comparison of Faradaic reactions in capacitive deionization (CDI) and membrane capacitive deionization (MCDI) water treatment processes. **Water Research**, *[S. l.]*, v. 120, p. 229–237, 2017. DOI: 10.1016/j.watres.2017.05.009.

TAYYEBI, Ahmad; OUTOKESH, Mohammad; MORADI, Shahab; DORAM, Amir. Synthesis and characterization of ultrasound assisted “graphene oxide-magnetite” hybrid, and investigation of its adsorption properties for Sr(II) and Co(II) ions. **Applied Surface Science**, *[S. l.]*, v. 353, p. 350–362, 2015. DOI: 10.1016/j.apsusc.2015.06.087.

ULLAH, Abaid; HUSSAIN, Salman; WASIM, Ahmad; JAHANZAIB, Mirza. Development of a decision support system for the selection of wastewater treatment technologies. **Science of the Total Environment**, *[S. l.]*, v. 731, p. 139158, 2020. DOI: 10.1016/j.scitotenv.2020.139158.

UNITED NATIONS WORLD WATER ASSESSMENT PROGRAMME. **The United Nations World Water Development Report 2017. Wastewater: The Untapped Resource.** Paris.

VANÝSEK, Petr. Electrochemical series. *Em*: **CRC Handbook of Chemistry and Physics**. 95th. ed. [s.l: s.n.]. p. (5)80-89.

VAQUERO, Susana; DÍAZ, Raul; ANDERSON, Marc; PALMA, Jesus; MARCILLA, Rebeca. Insights into the influence of pore size distribution and surface functionalities in the behaviour of carbon supercapacitors. **Electrochimica Acta**, *[S. l.]*, v. 86, p. 241–247, 2012. DOI: 10.1016/j.electacta.2012.08.006.

VERMA, Monu et al. Graphene oxide-manganese ferrite (GO-MnFe2O4) nanocomposite: One-pot hydrothermal synthesis and its use for adsorptive removal of Pb2+ ions from aqueous medium. **Journal of Molecular Liquids**, *[S. l.]*, v. 315, p. 113769, 2020. DOI: 10.1016/j.molliq.2020.113769. Disponível em: https://doi.org/10.1016/j.molliq.2020.113769.

VINODHA, G.; SHIMA, P. D.; CINDRELLA, L. Mesoporous magnetite nanoparticle-decorated graphene oxide nanosheets for efficient electrochemical detection of hydrazine. **Journal of Materials Science**, *[S. l.]*, v. 54, p. 4073–4088, 2019.

WANG, Huan Wen; HU, Zhong Ai; CHANG, Yan Qin; CHEN, Yan Li; ZHANG, Zi Yu; YANG, Yu Ying; WU, Hong Ying. Preparation of reduced graphene oxide/cobalt oxide composites and their enhanced capacitive behaviors by homogeneous incorporation of reduced graphene oxide sheets in cobalt oxide matrix. **Materials Chemistry and Physics**, *[S. l.]*, v. 130, n. 1–2, p. 672–679, 2011. DOI: 10.1016/j.matchemphys.2011.07.043.

WANG, Hui; YAN, Tingting; LIU, Peiying; CHEN, Guorong; SHI, Liyi; ZHANG, Jianping; ZHONG, Qingdong; ZHANG, Dengsong. In situ creating interconnected pores across 3D graphene architectures and their application as high performance electrodes for flow-through deionization capacitors. **Journal of Materials Chemistry A**, *[S. l.]*, v. 4, n. 13, p. 4908–4919, 2016. a. DOI: 10.1039/c5ta10703b.

WANG, Li; LIN, Shihong. Intrinsic tradeoff between kinetic and energetic efficiencies in membrane capacitive deionization. **Water Research**, *[S. l.]*, v. 129, p. 394–401, 2018. DOI: 10.1016/j.watres.2017.11.027.

WANG, Miao; XU, Xingtao; LIU, Yong; LI, Yanjiang; LU, Ting; PAN, Likun. From metal-organic frameworks to porous carbons: A promising strategy to prepare high-performance electrode materials for capacitive deionization. **Carbon**, *[S. l.]*, v. 108, p. 433–439, 2016. b. DOI: 10.1016/j.carbon.2016.07.047.

WANG, Nannan; ZHENG, Tong; ZHANG, Guangshan; WANG, Peng. A review on Fenton-like processes for organic wastewater treatment. **Journal of Environmental Chemical Engineering**, *[S. l.]*, v. 4, n. 1, p. 762–787, 2016. c. DOI: 10.1016/j.jece.2015.12.016.

WANG, Yang; VÁZQUEZ-RODRÍGUEZ, Inés; SANTOS, Cleis; GARCÍA-QUISMONDO, Enrique; PALMA, Jesús; ANDERSON, Marc A.; LADO, Julio J. Graphite felt 3D framework composites as an easy to scale capacitive deionization electrode for brackish water desalination. **Chemical Engineering Journal**, *[S. l.]*, v. 392, n. September, p. 123698, 2019. DOI: 10.1016/j.cej.2019.123698.

WANG, Zhongzhen; MA, Chen; XU, Chunyan; SINQUEFIELD, Scott A.; SHOFNER, Meisha L.; NAIR, Sankar. Graphene oxide nanofiltration membranes for desalination under realistic conditions. **Nature Sustainability**, *[S. l.]*, v. 4, p. 402–408, 2021. DOI: 10.1038/s41893-020-00674-3.

WEI, Cao; YIRAN, Ma; WEI, Zhou; LIN, Guo. One-pot Hydrothermal Synthesis of rGO-Fe3O4 Hybrid Nanocomposite for Removal of Pb (II) via Magnetic Separation. **Chemical Research in Chinese Universities**, *[S. l.]*, v. 31, n. 4, p. 508–513, 2015. DOI: 10.1007/s40242-015-4487-6.

WEI, L.; ZHAO, T. S.; ZHAO, G.; AN, L.; ZENG, L. A high-performance carbon nanoparticle-decorated graphite felt electrode for vanadium redox flow batteries. **Applied Energy**, *[S. l.]*, v. 176, p. 74–79, 2016. DOI: 10.1016/j.apenergy.2016.05.048.

WELGEMOED, T. J.; SCHUTTE, C. Frik. Capacitive Deionization Technology™: An alternative desalination solution. **Desalination**, *[S. l.]*, v. 183, n. 1–3, p. 327–340, 2005. DOI: 10.1016/j.desal.2005.02.054.

WOUTERS, Jesse J.; ISABEL TEJEDOR-TEJEDOR, M.; LADO, Julio J.; PEREZ-ROA, Rodolfo; ANDERSON, Marc A. Influence of metal oxide coatings, carbon materials and potentials on ion removal in capacitive deionization. **Journal of the Electrochemical Society**, *[S. l.]*, v. 165, n. 5, p. E148–E161, 2018. DOI: 10.1149/2.0271805jes.

WOUTERS, Jesse J.; TEJEDOR-TEJEDOR, M. Isabel; LADO, Julio J.; PEREZ-ROA, Rodolfo; ANDERSON, Marc A. Influence of Metal Oxide Coatings on the Microstructural and Electrochemical Properties of Different Carbon Materials. **Journal of The Electrochemical Society**, *[S. l.]*, v. 163, n. 13, p. A2733–A2744, 2016. DOI: 10.1149/2.0911613jes.

XU, Xingtao; PAN, Likun; LIU, Yong; LU, Ting; SUN, Zhuo; CHUA, Daniel H. C. Facile synthesis of novel graphene sponge for high performance capacitive deionization. **Scientific Reports**, *[S. l.]*, v. 5, p. 1–9, 2015. DOI: 10.1038/srep08458.

YANG, Kun Lin; YING, Tung-Yu; YIACOUMI, Sotira; TSOURIS, Costas; VITTORATOS, E. Steven. Electrosorption of ions from aqueous solutions by nanostructured carbon aerogel. **Langmuir**, *[S. l.]*, v. 17, n. 6, p. 1961–1969, 2001. DOI: 10.1021/la001527s.

YOO, Jeseung; KIM, Hyo Sun; PARK, Sang Yul; KWON, Suyong; LEE, Joohyun; KOO, Jaseung; SEO, Young Soo. Instantaneous integration of magnetite nanoparticles on graphene oxide assisted by ultrasound for efficient heavy metal ion retrieval. **Ultrasonics Sonochemistry**, *[S. l.]*, v. 64, n. 104962, 2020. DOI: 10.1016/j.ultsonch.2020.104962.

YOO, Myung Jin; PARK, Ho Bum. Effect of hydrogen peroxide on properties of graphene oxide in Hummers method. **Carbon**, *[S. l.]*, v. 141, p. 515–522, 2019. DOI: 10.1016/j.carbon.2018.10.009.

YU, Huitao; ZHA, Bangwen; CHAOKE, B.; LI, Ruihong; XING, Ruiguang. High-efficient Synthesis of Graphene Oxide Based on Improved Hummers Method. **Nature Publishing Group**, *[S. l.]*, v. 6, n. November, p. 1–7, 2016. DOI: 10.1038/srep36143.

ZÉLIS, P. Mendoza et al. Structural and magnetic study of zinc-doped magnetite nanoparticles and ferrofluids for hyperthermia applications. **Journal of Physics D: Applied Physics**, *[S. l.]*, v. 125006, n. 46, 2013. DOI: 10.1088/0022-3727/46/12/125006.

ZHANG, Bei; HU, Runtao; SUN, Dejun; WU, Tao; LI, Yujiang. Fabrication of chitosan/magnetite- graphene oxide composites as a novel bioadsorbent for adsorption and

detoxification of Cr(VI) from aqueous solution. **Scientific Reports**, *[S. l.]*, v. 8, n. 15397, p. 1–12, 2018. DOI: 10.1038/s41598-018-33925-7.

ZHANG, Yingying; ZHUANG, Yao; GENG, Jinju; REN, Hongqiang; XU, Ke; DING, Lili. Reduction of antibiotic resistance genes in municipal wastewater ef fl uent by advanced oxidation processes. **Science of the Total Environment**, *[S. l.]*, v. 550, p. 184–191, 2016. DOI: 10.1016/j.scitotenv.2016.01.078.

ZHAO, R.; BIESHEUVEL, P. M.; VAN DER WAL, A. Energy consumption and constant current operation in membrane capacitive deionization. **Energy and Environmental Science**, *[S. l.]*, v. 5, n. 11, p. 9520–9527, 2012.

ZHAO, Shanshan; YAN, Tingting; WANG, Hui; ZHANG, Jianping; SHI, Liyi; ZHANG, Dengsong. Creating 3D Hierarchical Carbon Architectures with Micro-, Meso-, and Macropores via a Simple Self-Blowing Strategy for a Flow-through Deionization Capacitor. **ACS Applied Materials and Interfaces**, *[S. l.]*, v. 8, n. 28, p. 18027–18035, 2016. DOI: 10.1021/acsami.6b03704.

ZHU, Xiaobo; LI, Wang; TANG, Sen; ZENG, Majian; BAI, Pengyuan. Selective recovery of vanadium and scandium by ion exchange with D201 and solvent extraction using P507 from hydrochloric acid leaching solution of red mud. **Chemosphere**, *[S. l.]*, v. 175, p. 365–372, 2017. DOI: 10.1016/j.chemosphere.2017.02.083. Disponível em: http://dx.doi.org/10.1016/j.chemosphere.2017.02.083.

ZIAEI, Ehsan; MEHDINIA, Ali; JABBARI, Ali. A novel hierarchical nanobiocomposite of graphene oxide-magnetic chitosan grafted with mercapto as a solid phase extraction sorbent for the determination of mercury ions in environmental water samples. **Analytica Chimica Acta**, *[S. l.]*, v. 850, p. 49–56, 2014. DOI: 10.1016/j.aca.2014.08.048.

ZORNITTA, Rafael L.; GARCÍA-MATEOS, Francisco J.; LADO, Julio J.; RODRÍGUEZ-MIRASOL, José; CORDERO, Tomás; HAMMER, Peter; RUOTOLO, Luis A. M. High-performance activated carbon from polyaniline for capacitive deionization. **Carbon**, *[S. l.]*, v. 123, p. 318–333, 2017. DOI: 10.1016/j.carbon.2017.07.071.

ZORNITTA, Rafael L.; LADO, Julio J.; ANDERSON, Marc A.; RUOTOLO, Luís A. M. Effect of electrode properties and operational parameters on capacitive deionization using low-cost commercial carbons. **Separation and Purification Technology**, *[S. l.]*, v. 158, p. 39–52, 2016. DOI: 10.1016/j.seppur.2015.11.043.

ZORNITTA, Rafael L.; RUOTOLO, Luís A. M. Simultaneous analysis of electrosorption capacity and kinetics for CDI desalination using different electrode configurations. **Chemical Engineering Journal**, *[S. l.]*, v. 332, n. September 2017, p. 33–41, 2018. DOI: 10.1016/j.cej.2017.09.067.

ANNEX A – FUNCTIONALIZED MAGNETIC GRAPHENE OXIDE COMPOSITES FOR SELECTIVE TOXIC METAL ADSORPTION

Figure A1 – Scanning electron microscopy images for (a) GO, (b) Fe_3O_4, (c) MAG-GO_1, (d) MAG-GO_2 and (e) MAG-GO_3 composites with magnification of 100 000x.

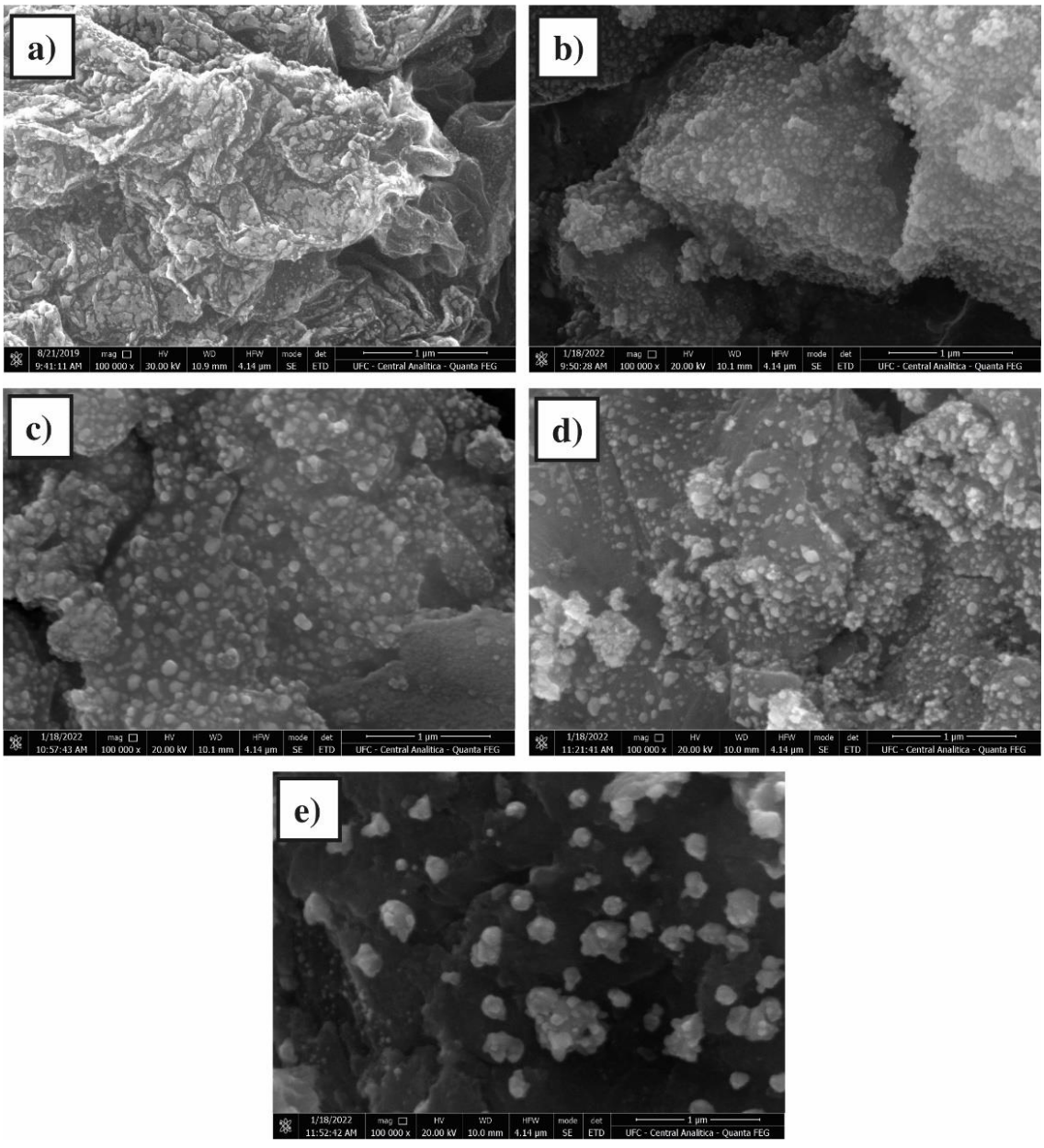

Source: the author.

Figure A2 – EDS mapping for (a) Fe_3O_4, (b) MAG-GO_1, (c) MAG-GO_2 and (d) MAG-GO_3 composites.

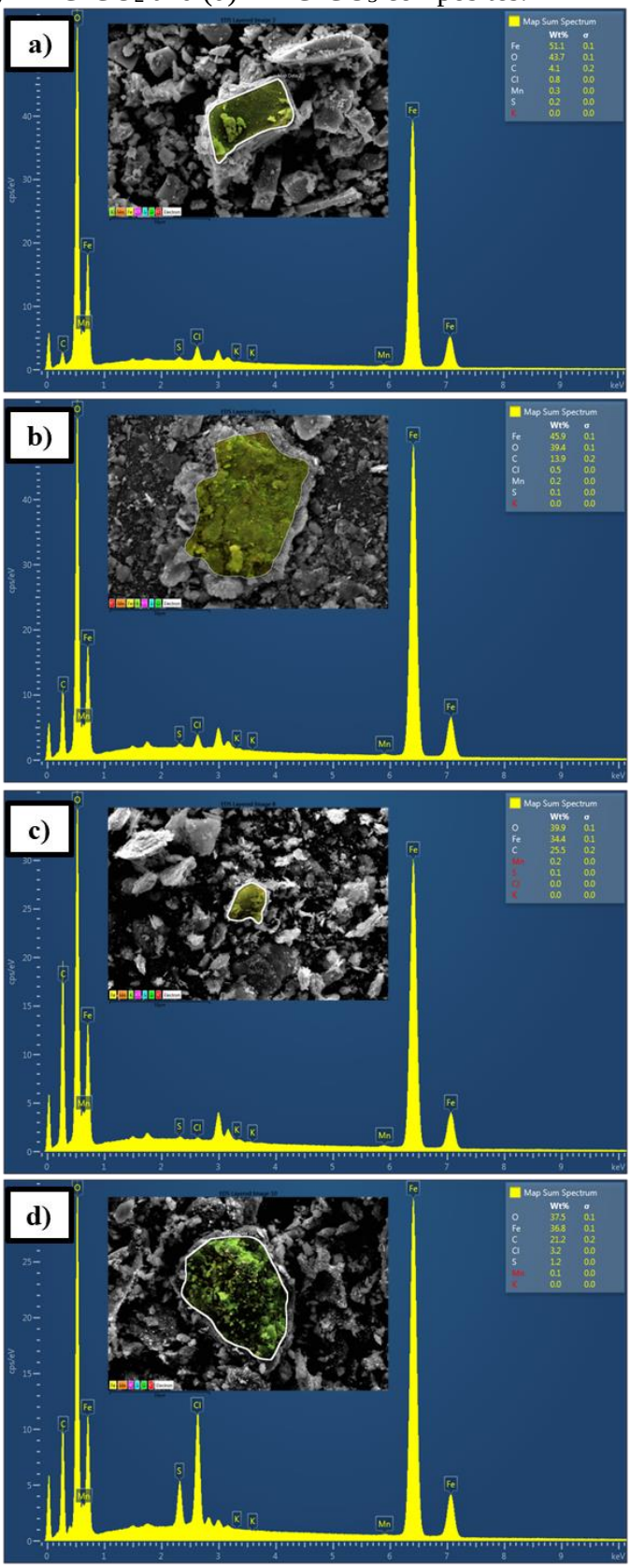

Source: the author.

Figure A3 – Survey spectra of MAG-GO_1 and MAG-GO_1-NH_2.

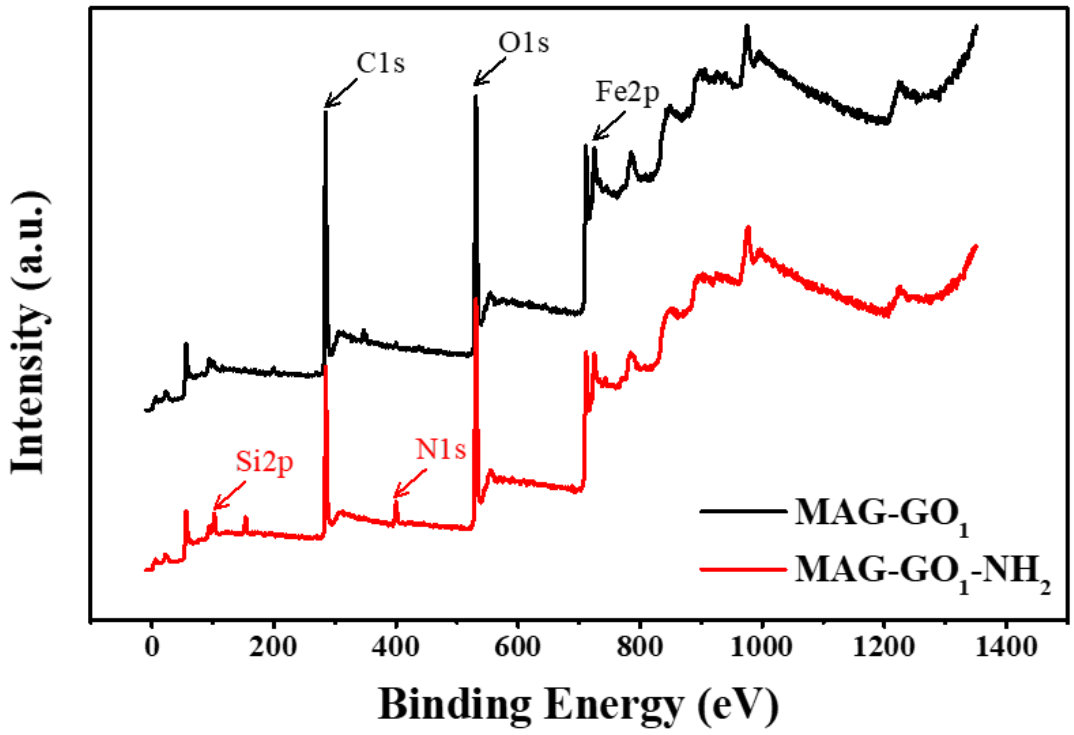

Source: the author.

Table A1 – Summary of XPS data for MAG-GO_1 and MAG-GO_1-NH_2.

	MAG-GO_1			**MAG-GO_1-NH_2**		
Element	**Binding Energy (eV)**	**Atomic Fraction (%)**	**Group**	**Binding Energy (eV)**	**Atomic conc. (%)**	**Group**
C1s	284.18	60.69	C-C/C=C	284.13	47.05	C-C/C=C
	285.00		C-O	284.75		C-O
	285.74		C-O-C	285.46		C-O-C
	286.82		C=O	286.45		C=O
	288.80		O-C=O	288.15		O-C=O
O1s	529.57	27.98	O-C=O	529.13	32.32	O-C=O
	530.28		Fe-O	530.10		Fe-O
	531.49		C-OH	530.88		C-OH
	532.86		C-O/Fe-OH	532.13		C-O/Fe-OH
$Fe2p_{3/2}$	710.31	9.55	Fe2+ oct	710.4	9.00	Fe^{2+} oct
	711.63		Fe3+ thd	711.67		Fe^{3+} thd
	713.93		Fe3+ oct	713.68		Fe^{3+} oct
	717.88			717.79		
	720.69			720.52		
$Fe2p_{1/2}$	723.11		Fe2+ oct	723.2		Fe^{2+} oct
	724.47		Fe3+ oct	724.59		Fe^{3+} oct
	726.73		Fe3+ thd	726.62		Fe^{3+} thd
	730.68			730.59		
	733.49			733.83		
N1s				399.91	5.42	$–NH_2$
				401.81		$–NH_3^+$

Source: the author.

Figure A4 – Species distribution diagram for Cu(II), Cd(II) and Cr(VI). The free softwares Medusa and Hydra were used to generate the species distribution diagrams.

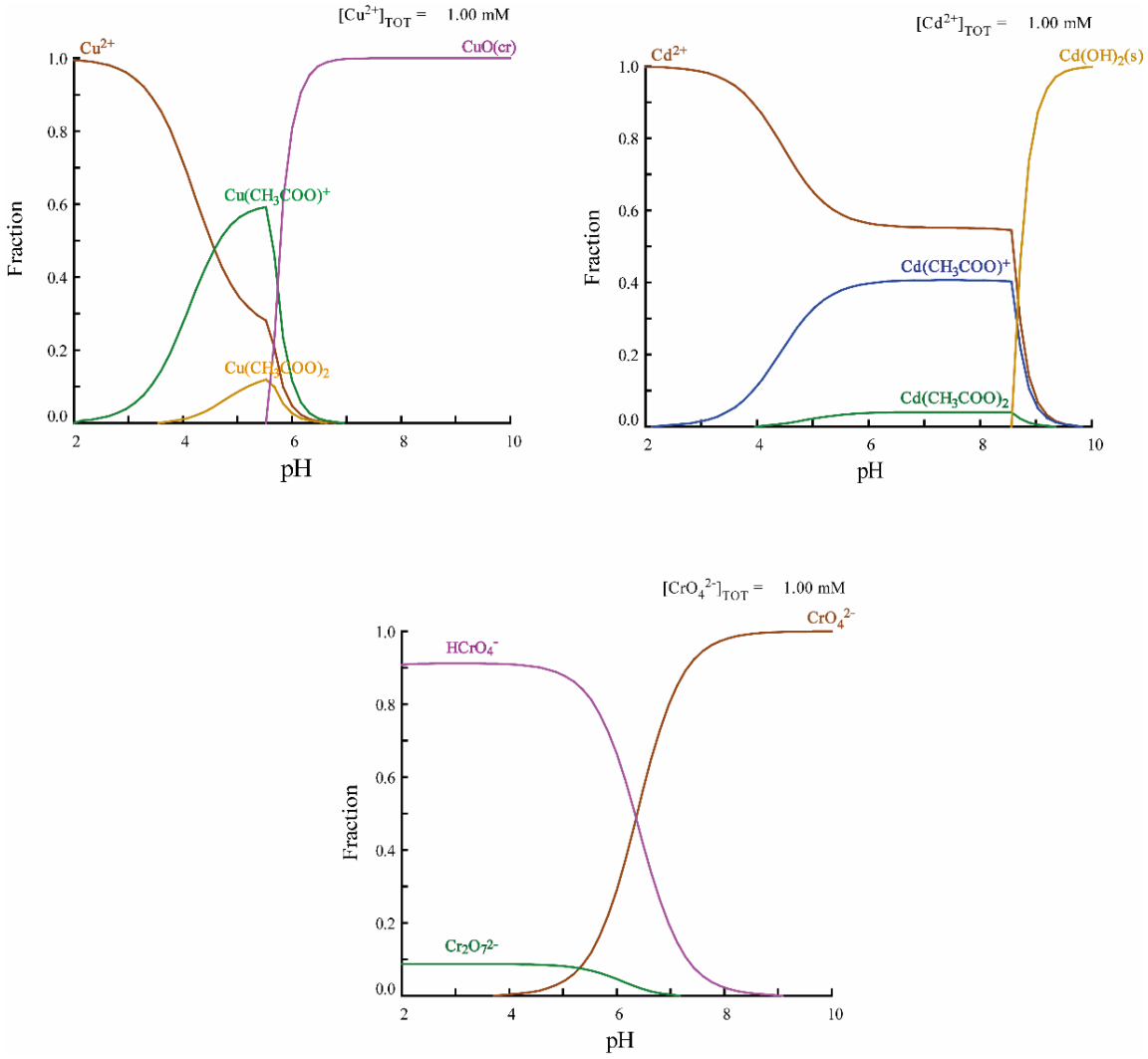

Source: the author.

Figure A5 – Van't Hoff plot for Cd(II), Cu(II), and Cr(VI) adsorption by MAG-GO_1-NH_2 at 298, 308 and 318 K.

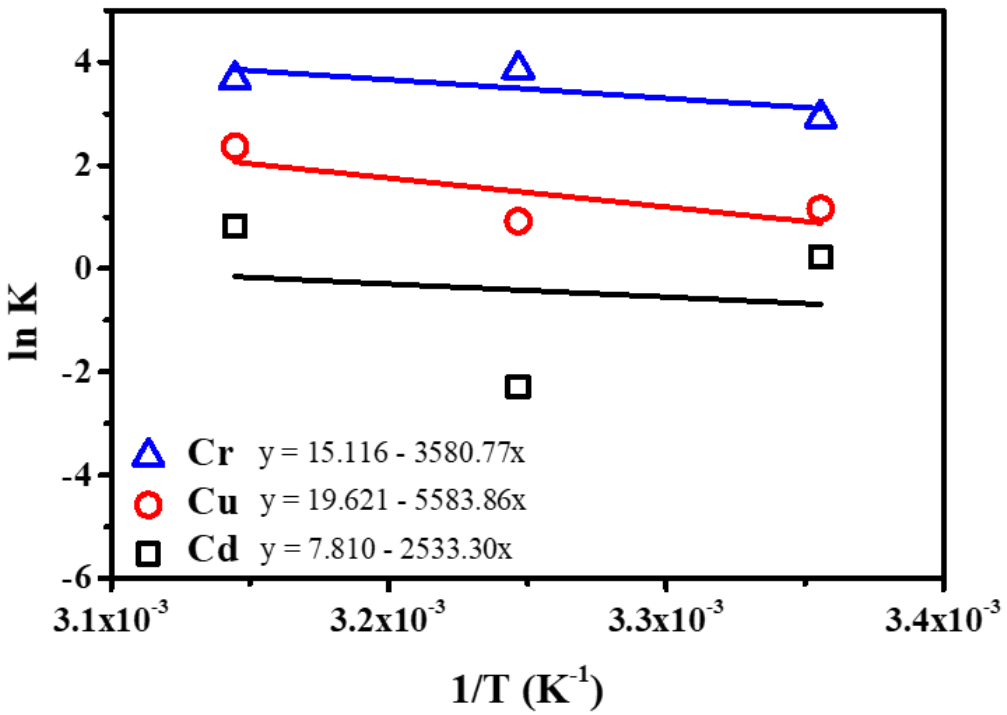

Source: the author.

In this study, five non-linear error functions were used to evaluate the adsorption model that better fits the obtained data:

1. The Sum of Squares of the Errors (ERRSQ):

$$\sum_{i=1}^{p}\left(q_{e,meas}-q_{e,calc}\right)_i^2$$

2. The Sum of Hybrid Fractional Error Functions (HYBRID):

$$\sum_{i=1}^{p}\left[\frac{\left(q_{e,meas}-q_{e,calc}\right)^2}{q_{e,meas}}\right]_i$$

3. The Sum of Marquardt's Percent Standard Deviations (MPSD):

$$\sum_{i=1}^{p}\left(\frac{q_{e,meas}-q_{e,calc}}{q_{e,meas}}\right)_i^2$$

4. The Sum of Average Relative Errors (ARE):

$$\sum_{i=1}^{p}\left|\frac{q_{e,meas}-q_{e,calc}}{q_{e,meas}}\right|_i$$

Table A2 – Isotherms parameters for MAG-GO_1 and MAG-GO_1-NH_2 materials at 298 K.

Material	**Isotherm**		**Cd(II)**	**Cu(II)**	**Cr(VI)**
			Parameters values		
MAG-GO_1	Langmuir	q_{max} (mmol g^{-1})	0.117 ± 0.100	0.119 ± 0.009	0.614 ± 0.091
		K_L	0.283 ± 0.310	11.714 ± 3.246	1.827 ± 0.595
		R^2	0.8755	0.9251	0.9602
		ERRSQ	8.11 x 10^{-5}	8.96 x 10^{-4}	7.18 x 10^{-3}
		HYBRID	0.0096	0.0219	0.0832
		MPSD	1.94	1.31	2.58
		ARE	3.15	2.42	3.24
	Freundlich	K_F	0.0246 ± 0.133	0.119 ± 0.012	0.407 ± 0.015
		1/n	1.035 ± 0.158	0.301 ± 0.065	0.587 ± 0.048
		R^2	0.9450	0.8198	0.9784
		ERRSQ	5.66 x 10^{-5}	0.037	0.061

		HYBRID	0.0079	0.47	0.49
		MPSD	1.78	8.18	6.35
		ARE	2.85	8.65	7.05
$MAG\text{-}GO_1\text{-}NH_2$	Langmuir	q_{max} (mmol g^{-1})	0.015 ± 0.014	0.088 ± 0.007	0.574 ± 0.055
		K_L	1.244 ± 1.764	3.198 ± 0.668	18.528 ± 7.425
		R^2	0.7879	0.9640	0.8937
		ERRSQ	4.38×10^{-6}	1.48×10^{-4}	0.0369
		HYBRID	0.0012	0.0065	0.29
		MPSD	0.52	0.60	4.47
		ARE	1.56	1.59	5.10
	Freundlich	K_F	0.0092 ± 0.002	0.0692 ± 0.003	0.568 ± 0.008
		1/n	0.710 ± 0.237	0.465 ± 0.030	0.249 ± 0.009
		R^2	0.8044	0.9787	0.9950
		ERRSQ	2.45×10^{-5}	6.86×10^{-3}	0.446
		HYBRID	0.0061	0.184	1.48
		MPSD	2.47	6.87	8.40
		ARE	3.58	7.86	8.88

Source: the author.

ERRSQ: Sum of Squares of the Errors / HYBRID: Sum of Hybrid Fractional Error Function / MPSD: Sum of Marquardt's Percent Standard Deviation / ARE: Sum of Average Relative Errors

Table A3 - Isotherms parameters for MAG-GO_1-NH_2 under different temperatures.

Temperature	Isotherm		Cd(II)	Cu(II)	Cr(VI)
			Parameters values		
298 K	Langmuir	q_{max} (mmol g^{-1})	0.015 ± 0.014	0.088 ± 0.007	0.574 ± 0.055
		K_L	1.244 ± 1.764	3.198 ± 0.668	18.528 ± 7.425
		R_L	1.03 – 4.50	0.94 – 0.14	0.71 – 0.02
		R^2	0.7879	0.9640	0.8937
		ERRSQ	4.38×10^{-6}	1.48×10^{-4}	0.037
		HYBRID	0.0012	0.0065	0.29
		MPSD	0.52	0.60	4.47
		ARE	1.56	1.59	5.10
	Freundlich	K_F	0.0092 ± 0.002	0.0692 ± 0.003	0.568 ± 0.008
		1/n	0.710 ± 0.237	0.465 ± 0.030	0.249 ± 0.009
		R^2	0.8044	0.9787	0.9950
		ERRSQ	2.45×10^{-5}	6.86×10^{-3}	0.45
		HYBRID	0.0061	0.18	1.48
		MPSD	2.47	6.87	8.40
		ARE	3.58	7.86	8.88
308 K	Langmuir	q_{max} (mmol g^{-1})	0.627 ± 0.582	0.202 ± 0.015	0.309 ± 0.033
		K_L	0.1007 ± 0.107	2.498 ± 0.436	47.659 ± 26.54
		R_L	1.01 – 1.20	0.87 – 0.19	0.26 – 0.01
		R^2	0.9843	0.9760	0.7479
		ERRSQ	1.10×10^{-4}	4.30×10^{-4}	0.0202
		HYBRID	0.0099	0.0052	0.20
		MPSD	2.64	0.15	2.88
		ARE	3.09	0.83	3.28
	Freundlich	K_F	0.056 ± 0.003	0.143 ± 0.008	0.323 ± 0.036
		1/n	0.960 ± 0.094	0.484 ± 0.059	0.158 ± 0.050

		R^2	0.9810	0.9296	0.6560
		ERRSQ	1.64×10^{-4}	4.28×10^{-2}	0.376
		HYBRID	0.0048	0.44	1.54
		MPSD	0.96	6.39	8.11
		ARE	1.97	7.37	8.41
318 K	Langmuir	q_{max} (mmol g^{-1})	0.178 ± 0.063	0.237 ± 0.022	0.317 ± 0.015
		K_L	2.257 ± 1.400	10.588 ± 3.635	38.973 ± 10.596
		R_L	1.14 – 5.56	0.61 – 0.05	0.30 – 0.01
		R^2	0.8562	0.9057	0.9386
		ERRSQ	5.77×10^{-4}	3.66×10^{-3}	5.64 x 10-3
		HYBRID	0.016	0.026	0.088
		MPSD	0.88	0.22	2.02
		ARE	1.46	1.04	2.33
	Freundlich	K_F	0.146 ± 0.030	0.225 ± 0.027	0.315 ± 0.021
		1/n	0.629 ± 0.169	0.311 ± 0.0824	0.147 ± 0.0402
		R^2	0.7817	0.7570	0.6912
		ERRSQ	0.011	0.18	1.47
		HYBRID	0.17	1.04	5.47
		MPSD	3.20	8.08	22.31
		ARE	4.26	7.96	12.40

Source: the author.

ERRSQ: Sum of Squares of the Errors / HYBRID: Sum of Hybrid Fractional Error Function / MPSD: Sum of Marquardt's Percent Standard Deviation / ARE: Sum of Average Relative Errors

Table A4 - Kinetic parameters of MAG-GO_1-NH_2 using 0.1, 0.5 and 1.0 mmol L^{-1} multielement solutions of Cd(II), Cu(II) and Cr(VI).

Ion concentration	**Kinetic model**		**Cd(II)**	**Cu(II)**	**Cr(VI)**
			Parameters values		
0.1 mmol L^{-1}	Pseudo-first-order	q_e (mmol g^{-1})	0.0035	0.0167	N.A.
		k_1	0.008	0.010	N.A.
		R^2	0.8441	0.9253	N.A.
	Pseudo-second-order	q_e (mmol g^{-1})	0.0031	0.0127	0.0517
		k_2	11.45	8.70	-119.12
		R^2	0.9709	0.9666	0.9999
0.5 mmol L^{-1}	Pseudo-first-order	q_e (mmol g^{-1})	0.0073	0.0599	0.0402
		k_1	0.027	0.114	0.020
		R^2	0.7564	0.9518	0.9192
	Pseudo-second-order	q_e (mmol g^{-1})	0.0028	0.0303	0.153
		k_2	-103.80	4.43	4.35
		R^2	0.9445	0.9960	0.9992
1.0 mmol L^{-1}	Pseudo-first-order	q_e (mmol g^{-1})	0.0104	0.0615	0.0410
		k_1	0.011	0.038	0.039
		R^2	0.7757	0.8715	0.9761
	Pseudo-second-order	q_e (mmol g^{-1})	0.0106	0.0756	0.327
		k_2	-42.01	0.97	3.24
		R^2	0.9657	0.9802	0.9999

Source: the author.

N.A.: not applied

ANNEX B – STRATEGIES TO BOOST CAPACITIVE DEIONIZATION PERFORMANCE OF 3D ELECTRODES

Figure B1 – Calibration curve of conductivity *versus* concentration of NaCl.

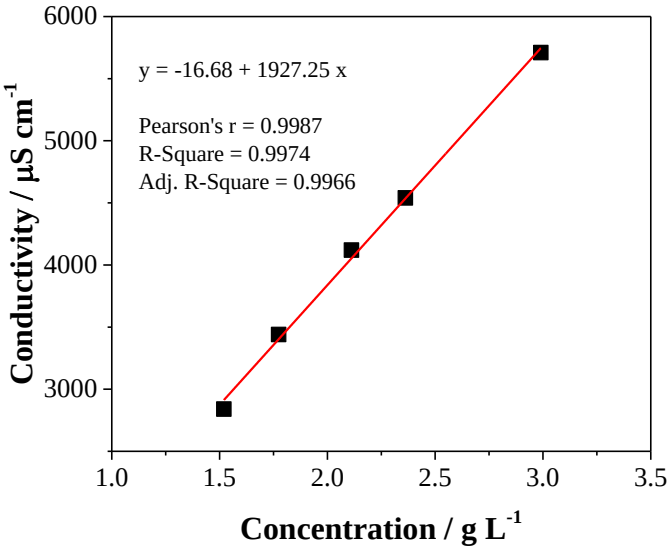

Source: the author.

Table B1 – Comparison of GF-ACx electrodes performance in terms of Δ*c*, *SAC* and *ASAR*.

		GF-AC$_{2.0}$			**GF-AC$_{3.0}$**			**GF-AC$_{5.0}$**		
E$_{cell}$	***Ic/Id***	***Δc***	***SAC***	***ASAR***	***Δc***	***SAC***	***ASAR***	***Δc***	***SAC***	***ASAR***
V	**mA**	**mg L^{-1}**	**mg g^{-1}**	**mg g^{-1} min^{-1}**	**mg L^{-1}**	**mg g^{-1}**	**mg g^{-1} min^{-1}**	**mg L^{-1}**	**mg g^{-1}**	**mg g^{-1} min^{-1}**
1.0	20/10	50.3	5.9	0.24	32.7	3.6	0.14	21.0	1.5	0.08
1.0	30/15	34.5	4.1	0.34	14.0	1.5	0.13	5.3	0.4	0.06
1.0	40/20	19.3	2.2	0.41	5.3	0.6	0.09	7.0	0.5	0.13
1.1	20/10	62.5	7.3	0.25	43.2	4.7	0.15	29.2	2.1	0.09
1.1	30/15	50.3	5.9	0.38	19.3	2.1	0.14	10.5	0.7	0.09
1.1	40/20	24.0	2.8	0.44	8.8	0.9	0.11	7.0	0.5	0.16
1.2	20/10	67.2	7.9	0.22	60.8	6.6	0.16	38.0	2.7	0.10
1.2	30/15	59.0	6.9	0.38	45.0	4.9	0.22	10.5	0.7	0.09
1.2	40/20	48.5	5.7	0.50	25.7	2.8	0.24	7.0	0.5	0.14

Source: the author.

Table B2 – Comparison of GF-AC electrodes performance in terms of η_{coul} and Λ_{cycle}.

E_{cell}	Ic	Id	Λ_{cycle} $GF\text{-}AC_{2.0}$	Λ_{cycle} $GF\text{-}AC_{3.0}$	Λ_{cycle} $GF\text{-}AC_{5.0}$
V	**mA**	**mA**	**%**	**%**	**%**
1.0	20	10	54.8	38.3	31.7
1.0	30	15	58.6	38.9	17.4
1.0	40	20	75.6	12.7	28.7
1.1	20	10	52.4	36.4	35.3
1.1	30	15	62.2	27.6	26.6
1.1	40	20	59.8	16.5	35.5
1.2	20	10	41.7	35.9	37.2
1.2	30	15	58.9	37.9	26.6
1.2	40	20	62.0	33.8	31.2

Source: the author.

FARADAIC LOSSES CALCULATION

Faradaic losses calculation: Faradaic losses (e.g. reduction of dissolved oxygen at 0.69 V (vs. SHE) and oxidation of carbon electrode at 0.7 – 0.9 V) were estimated considering the area under the experimental charging curves and the area under completely capacitive charging curves (Fig. B2) (HEMMATIFAR et al., 2016).

Figure B2 – Representation of the areas under the charging curves of a capacitive process and an experimental result.

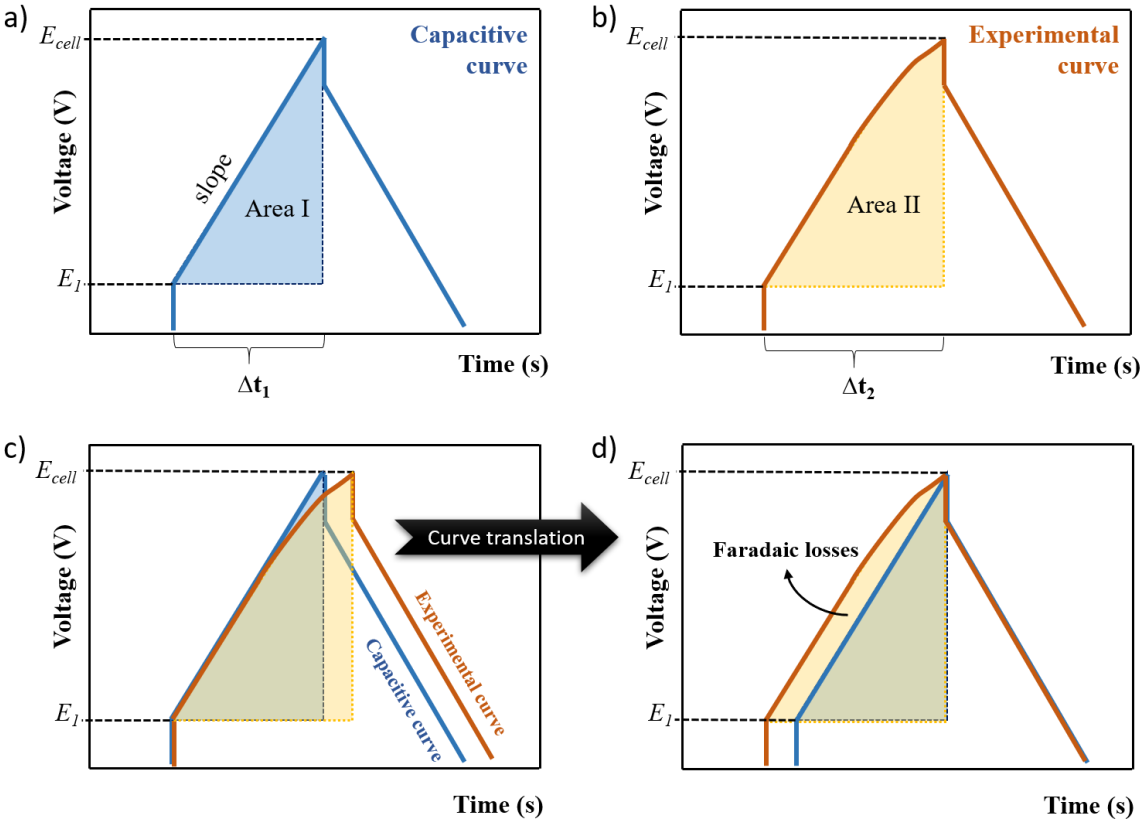

Considering a capacitive process, the theoretical time to perform the charging process was extracted from the Equation B1 and applied on Equation B2 to calculate the area under the charging curve (integral). The slope was calculated from the straight region of the experimental charging curve (0.2 – 0.8 V for GF-$AC_{2.0}$ and GF-$AC_{3.0}$, and 0.4 – 0.8 V for GF-$AC_{5.0}$).

$$slope\ (V\ s^{-1}) = \frac{E_{cell} - E_1}{\Delta t_1} \qquad \text{(B1)}$$

$$Area\ I\ (V \cdot\ s) = \frac{(E_{cell} - E_1) \times \Delta t_1}{2} \qquad \text{(B2)}$$

Wherein E_{cell} is the cell potential (V), E_1 is the overpotential (V) and Δt_1 is the time (s). The area from the experimental charging curve was calculated from Equation B3.

$$Area\ II\ (V \cdot\ s) = \int Vdt\ - E_1 \times \Delta t_2 \qquad \text{(B3)}$$

Then, the estimated Faradaic loss was calculated considering the areas I and II by using Equation B4.

$$Faradaic\ losses\ (\%) = \frac{Area\ II - Area\ I}{Area\ II} \times 100 \qquad \text{(B4)}$$

Table B3 – Effect of AC mass loading on GF-$AC_{2.0}$ electrodes performance in terms of *Δc*, *SAC*, and *ASAR*.

		31.6 mg AC cm^{-2}			**37.6 mg AC cm^{-2}**			**55.5 mg AC cm^{-2}**		
E_{cell}	***Ic/Id***	***Δc***	***SAC***	***ASAR***	***Δc***	***SAC***	***ASAR***	***Δc***	***SAC***	***ASAR***
V	**mA**	**mg L^{-1}**	**mg g^{-1}**	**mg g^{-1} min^{-1}**	**mg L^{-1}**	**mg g^{-1}**	**mg g^{-1} min^{-1}**	**mg L^{-1}**	**mg g^{-1}**	**mg g^{-1} min^{-1}**
1.0	20/10	63.7	7.5	0.22	50.3	5.9	0.24	-	-	-
1.0	30/15	55.5	6.5	0.37	34.5	4.1	0.34	48.5	4.1	0.18
1.0	40/20	60.8	7.1	0.61	18.7	2.2	0.42	57.3	4.8	0.29
1.1	20/10	57.3	6.7	0.20	61.9	7.3	0.25	-	-	-
1.1	30/15	60.8	7.1	0.32	50.3	5.9	0.38	67.8	5.6	0.15
1.1	40/20	60.8	7.1	0.51	24.0	2.8	0.44	88.2	7.5	0.32
1.2	20/10	48.5	5.7	0.13	67.2	7.9	0.22	-	-	-
1.2	30/15	53.8	6.3	0.24	59.0	6.9	0.38	74.8	6.1	0.12
1.2	40/20	60.8	7.1	0.42	48.5	5.7	0.50	95.3	8.1	0.29

Source: the author.

Figure B3 – Effect of voltage and current on performance in terms of productivity (a) and energy consumption per m^3 of solution (b) when using GF-$AC_{2.0}$ electrodes.

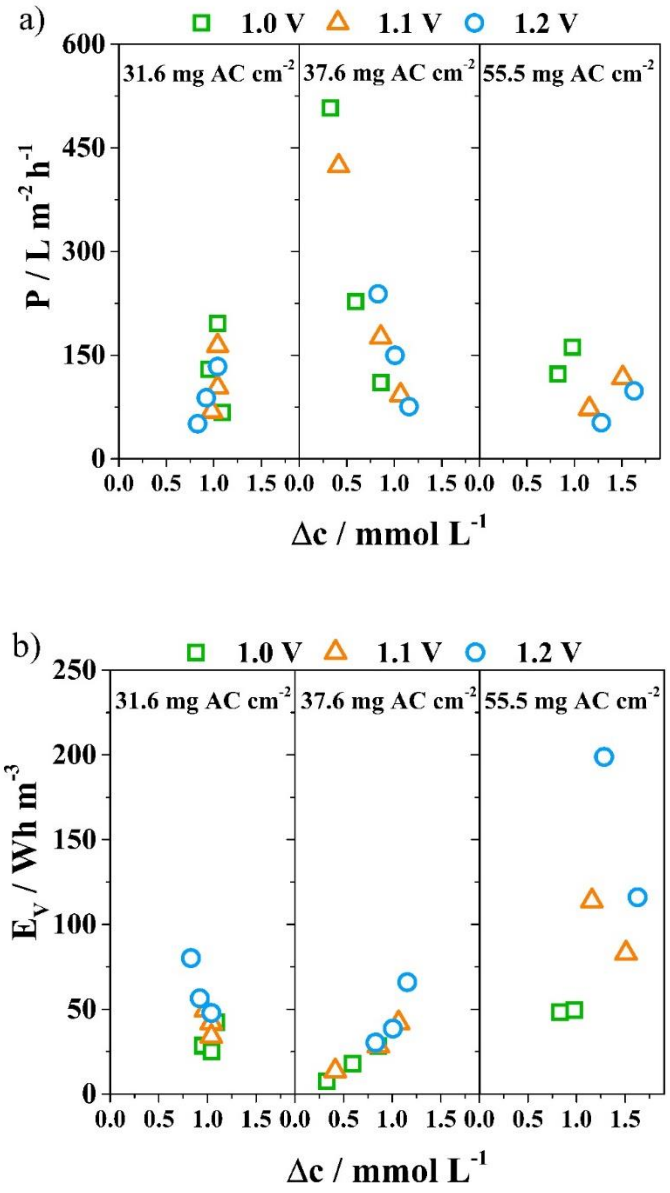

Source: the author.